1-5-2018

Strain Engineering of Two-Dimensional (2D) Materials at the Atomic Scales

Jin Wang
University of Connecticut - Storrs, jin.wang@uconn.edu

Strain Engineering of Two-Dimensional (2D) Materials at the Atomic Scales

Jin Wang, Ph.D.

University of Connecticut, 2018

Since the discovery of graphene, there has been a fast-growing interest in fabricating ultrathin 2-dimensional (2D) films and nano flakes out of materials with layered structures. Among all these materials, transition metal dichalcogenides (TMDs) such as MoS_2, WSe_2, HfS_2 and ReS_2, are semiconductors that show significant promise for use in electronics, optoelectronics, and catalytic applications. These materials comprise of covalent interactions between the atoms within the layer and van der Waals (vdW) interactions between the layers. Recent experiments have demonstrated that strain engineering is an effective method to tune the electronic, magnetic and optical properties of these 2D materials for their optimal performance. Strain engineering of 2D materials entails a thorough understanding of the deformation behavior, which is hard to capture experimentally. However, the recent advancements in computational methods at the atomic scales are well-suited to probe the effects of strains on the electronic properties as well as the mechanical response of 2D materials. The chemical vapor deposition (CVD) grown 2D materials comprise of flakes of several layers wherein the top layers are relatively narrower than the bottom layers. The strain response of such multi-layered structures is likely to be different as compared to their thin film counterpart. As a result, the investigation of the

strain response of monolayer and CVD-grown few layered 2D materials at the atomic scales is performed in this thesis.

First part of this work is based on density functional theory (DFT) simulations to explore the variations in the local electronic structure and local strain relaxation under varying loading strains for CVD-grown MoS_2. The difference in the electronic structure at/below the edges in multilayered structures is discussed. In addition, the effects of the presence of defect structures on the modifications in the local electronic structure and the strain relaxation (sliding) of the MoS_2 bilayer structures are identified.

These DFT simulations, however, are limited to system sizes of a few nanometers. As a result, classical molecular dynamics (MD) simulations are used to model system sizes close to the experimental length scales. The capability of MD simulations to model material behavior is determined by the capability of the interatomic potential being used to reproduce the mechanical and thermodynamic response. Therefore, current work focuses on the investigation of the reactive bond order (REBO) potential to reproduce the elastic properties as well as the strain response of MoS_2 monolayer and few-layer MoS_2 sheets. The results suggest that the REBO potential can model the elastic deformation behavior of MoS_2 bilayer sheets as predicted by DFT calculations. However, the REBO potential slightly over predicts the in-plane elastic constants as well as the strain transfer between the MoS_2 layers. A re-parameterization of the REBO potential for the MoS_2 system to correct for the accurate strain transfer across the MoS_2 layers is therefore performed. The evolution of the microstructure and the atomic scale mechanisms for strain relaxation are discussed using MD simulation for various types of edge configurations. The origins of

ripples as found in experiments are identified. In addition, the underlying correlations between strain relaxation and Moiré patterns are discussed at the atomic scale.

This study extends to investigate the effects of strain on the local electronic structure of 2D WSe_2 and HfS_2, and the modifications in the chemistry for various systems under the applied strain are discussed and compared. The understanding of the links between structure, stacking sequence and electronic properties in 2D materials allow for the possibility of unprecedented performance improvements for the miniaturized electronic devices.

Strain Engineering of Two-Dimensional (2D) Materials at the Atomic Scales

Jin Wang

A Dissertation

Submitted in Partial Fulfilment of the

Requirements for the Degree of

Doctor of Philosophy

at the

University of Connecticut

2018

APPROVAL PAGE

Doctor of Philosophy Dissertation

Strain Engineering of Two-Dimensional (2D) Materials at the Atomic Scales

Presented by

Jin Wang

Major Advisor _____

Dr. Avinash M. Dongare

Associate Advisor _____

Dr. Puxian Gao

Associate Advisor _____

Dr. Seok-Woo Lee

University of Connecticut

2018

to my dear parents

to my beloved fiancée

Acknowledgement

First and foremost, I would like to express my sincere gratitude to my supervisor Prof. Avinash Dongare for his consistent support, guidance and encouragement throughout my entire graduate life. Prof. Dongare infuses my research with curiosity and enthusiasm, and always instructs me to dig into the problem to unravel the mystery of the underlying science. Apart from research, Prof. Dongare provides enormous advice and valuable resource for my carrier development.

I am deeply appreciative of the discussions and comments from my advisory committee members: Prof. Rampi Ramprasad, Prof. Puxian Gao, Prof. Serge Nakhmanson, and Prof. Seok-Woo Lee. Their knowledge and insights are inspiring to my research.

Also, I would like to thank Dr. Madan Dubey and Dr. Sina Najmaei for their hospitality and mentorship during my 7-month visit to the Army Research Laboratory.

My heartfelt appreciation goes to all the group members of CMMG family. Dr. Liang Dong patiently tutored me in calculating electronic properties and setting up VASP simulations. I will always remember the good occasions with Jie Chen, Garvit Agarwal, Sumit A. Suresh, and Sergey Galitskiy. I am grateful to their strong supports and what I have learned from them: presentation skills, time-management, scripting, etc. I could see vast research potential of CMMG group from them, and I wish you all the success in the future.

I must thank Avinash and Fayekah Assanah for their summer and winter treats each year. I can never forget all the delicious Indian foods and good times, and sadly these experiences won't come back.

Finally, I would like to thank my fiancée Hao for her consistent support. I love you.

TABLE OF CONTENTS

TABLE OF FIGURES

CHAPTER ONE

1. INTRODUCTION

1.1 Transition Metal Dichalcogenide Materials

Transition metal dichalcogenides (TMDs) are a class of materials with a chemical formula of MX_2, where M represents transition metal element from group 3 to group 12, and X is a chalcogen (S, Se or Te). Currently, there are around 60 TMDs known since 1960s, with two-thirds of them forming layered structure [1]. In these layered structures, metals form strong covalent bonds with chalcogens in the *x-y* plane, while in the vertical direction the layers are weakly bonded by van de Waals (vdW) interactions. Due to the weak interactions between layers, the TMDs offer a low coefficient of friction. As a result, they have been used as dry lubricants to reduce the friction since 1970s [2]. Figure 1.1 identifies the transition metals in the periodic table (highlighted as light blue) that form layered structures when bonded with chalcogens. It can be seen that such transition metals are mainly from group 4-7 and group 10.

The rediscovery of TMDs is attributed to the renaissance in layered materials since the discovery of graphene in 2004 [3]. In addition to TMDs and graphene, two dimensional structures have also been synthesized for other layered materials, such as hexagonal boron nitride (hBN), germanane, silicene, phosphorene, etc. [3]. These materials are termed as

two dimensional (2D) materials, because they can be easily exfoliated from bulk to monolayer due to weak interlayer interaction [3]. Among all the 2D materials beyond graphene, TMDs attracted most attentions because the large family of TMDs covers diverse

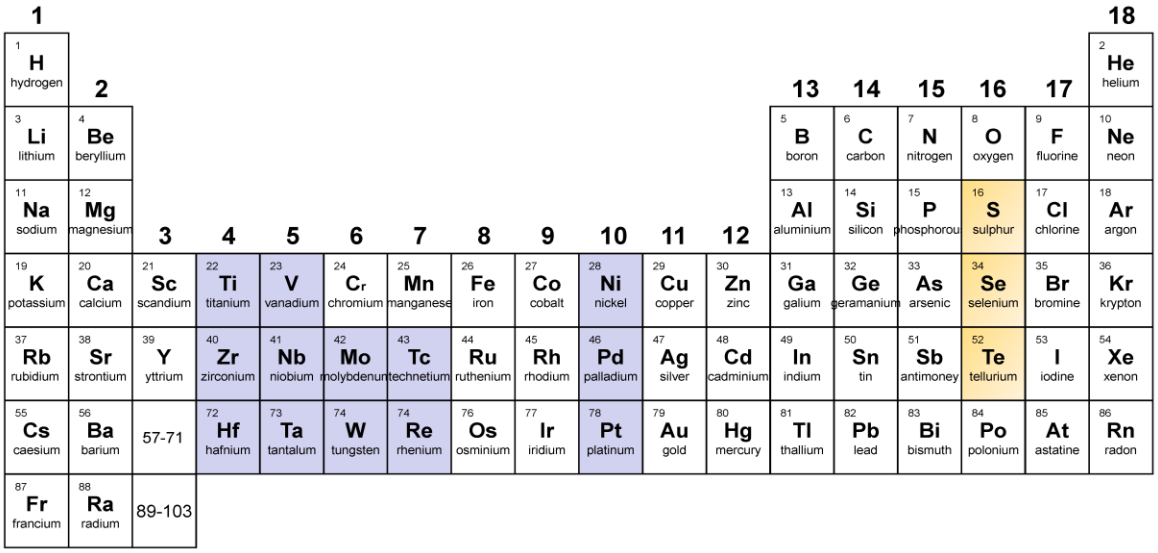

Figure 1.1 Periodic table shows layered TMDs. Three chalcogens are in light yellow. The transition metals that form layered structures with chalcogens are highlighted in light blue.

properties ranging from semiconductors to superconductors, depending on their composition and structure. As a result, the TMDs-based novel devices have been successfully demonstrated or proposed in applications of nanoelectronics, optoelectronics, spintronics, valleytronics, piezoelectric devices, and superconductivity [4-7].

1.2 Crystal Structures and Electronic Properties of TMDs

The bulk structure of TMDs comprises of stacked layers of MX_2, where each MX_2 layer consists of one hexagonal plane of M atoms sandwiched between two planes of hexagonally packed chalcogen atoms. The thickness of one MX_2 layer is typically 6~7 Å, and the in-plane lattice parameters *a* are in the range 3.1 Å to 3.7 Å. Depending on the

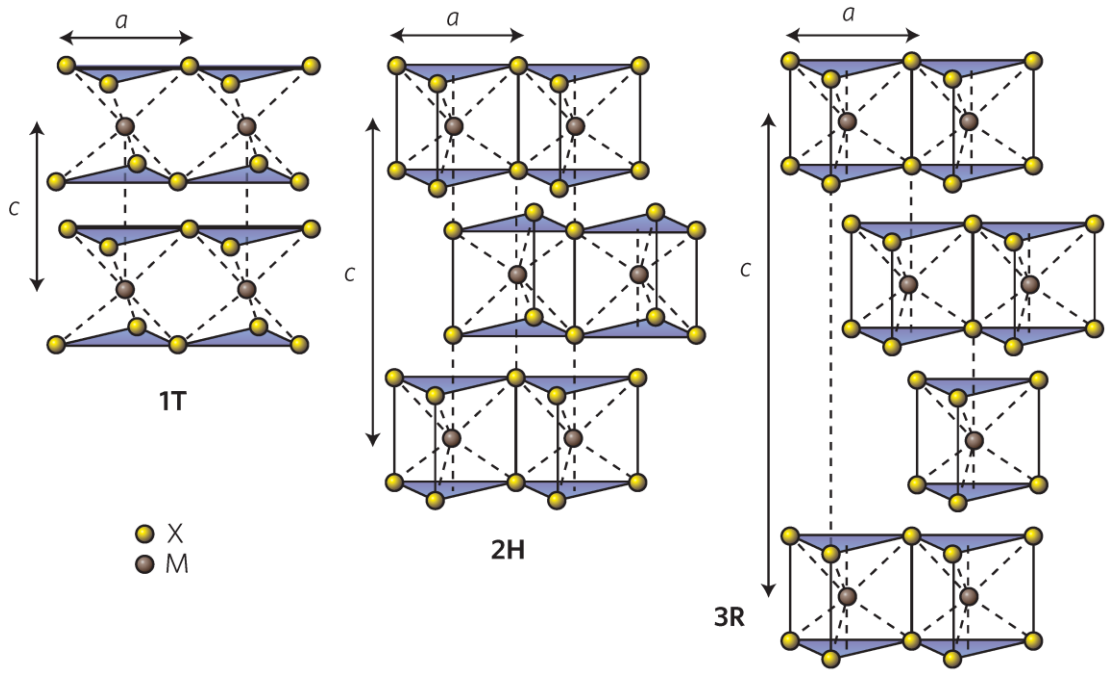

Figure 1.2 Schematics of the crystalline structures of 1*T*, 2*H*, 3*R* phases of TMDs. Reproduced from Ref. [5].

stacking sequences and the metal atom coordination, three phases are commonly found in TMDs: 1*T,* 2*H,* 3*R,* as shown in Figure 1.2. The number 1, 2, 3 denote the number of MX_2 layers per unit cell, and the letter *T, H, R* are labeled as trigonal, hexagonal and rhombohedral, respectively. The 1*T* phase presents a tetragonal symmetry, and each M atom is octahedrally coordinated with six X atoms. Such a stacking requires only one MX_2 layer per unit cell for 1*T* phase. The 2*H* phase has hexagonal symmetry, and each M atom is coordinated with six X atoms in a trigonal prismatic polyhedron. There are two layers per unit cell with a *AB* stacking sequence. The 3*R* phase shows a rhombohedral symmetry with a trigonal prismatic coordination for M atom and three MX_2 layers per unit cell in a *ABC* stacking order.

In general, the electronic properties of the TMDs are determined by the progressive filling of *d* bands of the transition metals. If the highest bands are completely filled, such

as group 4, group 5 and group 10, the materials exhibit semiconducting characteristic. On the other hand, if the top bands are partially filled, the resulting TMDs are metallic (group 5 and group 7). The unbonding band contributed from *d* orbitals of transition metals lies between the σ* anti-bonding bands and σ bonding bands, as shown in Figure 1.3. These unbonding *d* bands are degenerated into two groups in D_{3d} symmetry (1T), and three groups in D_{3h} symmetry (2*H* or 3R) [8]. However, the electronic properties of TMDs are also affected by their crystalline structure. For example, ReS_2 from group 7 is supposed to be metallic according to Figure 1.3. However, the stable ReS_2 presents a distorted phase (1T') rather than 1*T,* and thus exhibits a semiconducting electronic structure with a band gap of 1.9 eV [9].

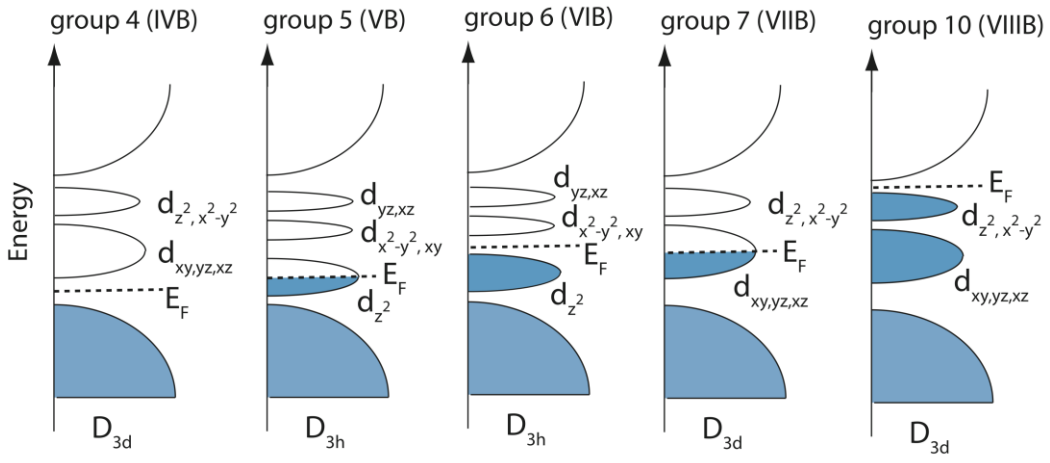

Figure 1.3 Schematics of the DOS of TMDs formed form different groups of transition metals. Reproduced from Ref. [8].

As a result, the electronic properties of TMDs are dependent on the coordination of the metal atoms and the interplay between M-*d* electrons and X-*p* electrons, which result in electronic properties in a wide variety of ranges from superconducting to semiconducting, as listed in Table 1.1 [10]. The diverse characteristics of TMDs allow

them playing different roles and offering various functionalities in electronic devices. For example, the semiconducting MoS_2, $MoSe_2$, WSe_2, HfS_2, etc., are promising in building transistors, switches, sensors, and optoelectronic devices, while the semi-metallic TMDs (such as $TiSe_2$, WTe_2) can be implemented as interconnects [1]. The metallic TMDs are possible to be fabricated in Josephson junctions and superconducting qubits [1].

Table 1.1 Electronic properties of different layered TMDs [10]. ρ is in-plane electrical resistivity.

Group	M	X	Electronic Properties
4	Ti, Hf, Zr	S, Se, Te	Semiconducting (*E*g = 0.2~2 eV).
5	V, Nb, Ta	S, Se, Te	Narrow band metals (ρ ~ 10^{-4} Ω.cm) or semimetals.
6	Mo, W	S, Se, Te	Semiconducting (*E*g = 1~1.9 eV).
7	Tc, Re	S, Se, Te	Semiconducting (*E*g ~ 1 eV).
10	Pd, Pt	S, Se, Te	Sulfides and selenides are semiconducting (*E*g = 0.4 eV). Tellurides are metallic. $PdTe_2$ is superconducting.

As compared to other nanostructures, such as nanowires and nanotubes, 2D materials allow greater flexibilities, in that the electronic, optical and magnetic properties can be readily altered by many approaches including external electric or magnetic field

[11-14], phase engineering [15], heterostructure fabrication [16, 17], and strain engineering [18-20]. Therefore, 2D TMDs have been recognized as promising building blocks for a wide range of applications in various nanophotonic and nanoelectronic devices.

For example, TMDs present superb mechanical strength, sizable band gap and high mobility in their monolayer structure [21]. The band gap of 2D TMDs are comparable to that of silicon ~1.1 eV, which is suitable for transistors. In addition, the direct band transition in monolayer structure is preferred in the implementation of transistor due to its low energy consumption, which makes them attractive as a conductive channel material for the next generation field effect transistors (FETs).

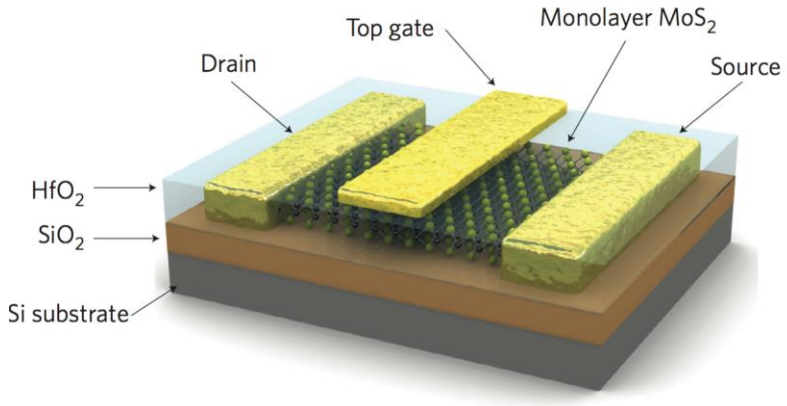

Figure 1.4 Three-dimensional schematics of the first top-gated transistor based on monolayer MoS_2. Reproduced from Ref. [23].

The FETs is a three-terminal system consisting of source, drain and gate electrodes, which is integrated in many electronic devices to achieve high-speed switching [22]. The operation of FETs is largely dependent on the performance of the channel semiconducting materials to span the source and drain electrodes. The traditional channel materials are composed of silicon, the III-V semiconductors, GaSs and GaN [22]. However, these 3D

materials are limited to the quantum effects when scaled down to nanoscale dimensions. As a result, the outstanding features of 2D TMDs make them promising candidates as channel materials for the next generation FETs. The first top-gated FETs based on single layer MoS_2 is shown in Figure 1.4, where 30 nm of HfO_2 layers with a high-κ dielectric are engineered as a gate insulator to improve the mobility and control charge density in a local manner [23]. This transistor demonstrated an exceptional mobility of at least 200 cm^2 V^{-1} S^{-1} and extraordinary current on/off ratios of 1×10^8 at room temperature, as well as ultralow standby power dissipation due to the large direct band gap of monolayer MoS_2 [23]. In addition, as compared to the back-gated transistors [24], the top-gated geometry reduced the voltage required to switch the device, and allowed the integration of multiple circuits in the same substrate [5]. Similarly, TMDs have also been used in sensors [25], and optoelectronic devices [26].

2D materials allow greater flexibilities, in that the electronic, optical and magnetic properties can be readily altered by many approaches including external electric or magnetic field [11-14], phase engineering [15], heterostructure fabrication [16, 17], and strain engineering [18-20]. Therefore, 2D TMDs have been recognized as promising building blocks for a wide range of applications in various nanophotonic and nanoelectronic devices. Thus, superior characteristics of 2D TMDs have attracted extensive research interests, and the application and optimization require the fundamental understanding of the electronic, optical and the mechanical properties of 2D TMDs.

1.3 Synthesis of TMDs

The synthesis of 2D TMDs is typically carried out using two routes. The first is top-down route, in which the bulk TMD crystals are exfoliated into monolayer or few layers by various methods, including mechanical exfoliation (Scotch-tape method), liquid and chemical exfoliation, intercalation by ionic species, and so on [8]. In these approaches, the vdW interaction between adjacent layers are weakened by various treatments. For

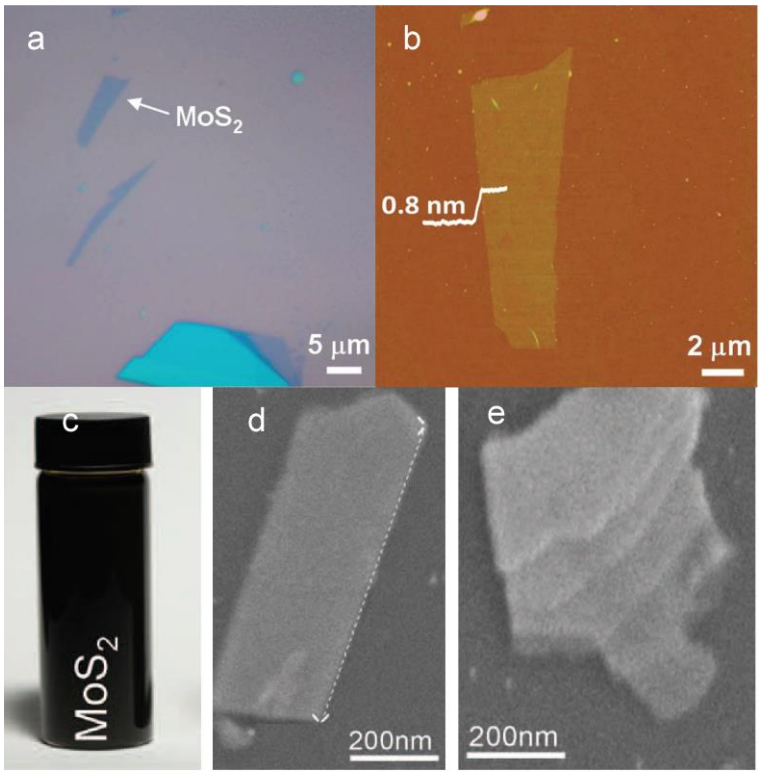

Figure 1.5 (a) Optical image and (b) AFM image of single layer MoS_2 prepared by mechanical exfoliation. Reproduced from Ref. [26]. (c)-(e) liquid exfoliation method: (c) dispersion of MoS_2 into NMP solvent. SEM image of (d) thin flake and (e) multilayer MoS_2. Reproduced from Ref. [28].

example, in mechanical exfoliation method (Figure 1.5 (a)-(b)), the 2D TMDs are obtained by repeatedly peeling the bulk TMD crystals on substrates with adhesive tapes [27]. Also,

in liquid exfoliation method (Figure 1.5 (c)-(e)), the monolayer or few-layer TMDs can be exfoliated from bulk TMD crystals in N-methyl-pyrrolidone solvent. The largest limitation of exfoliated methods is the small size. The 2D TMDs prepared from exfoliated methods are limited in tens of microns, which is unrealistic in device applications. In addition, the

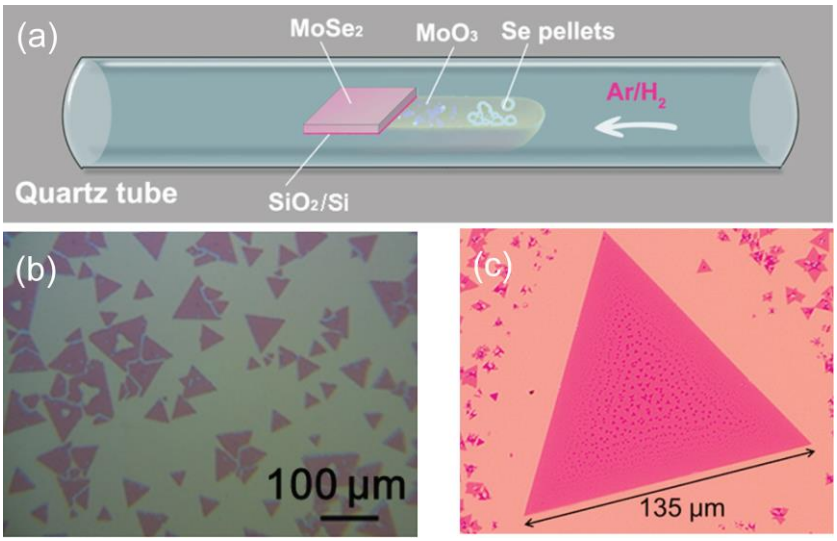

Figure 1.6 (a) Schematic setup of the controlled synthesis of the monolayer $MoSe_2$. (b) and (c) Typical optical images of monolayer $MoSe_2$ triangles. Reproduced from Ref. [28].

poor-quality control of this methods also poses limitations to their applicability in devices. The second is a bottom-up route, such as chemical vapor deposition (CVD), wherein the M and X atoms are vaporized by hot carrier gas and deposited on substrate. An example synthesis of 2D TMDs by metal chalcogenisation in CVD is shown in Figure 1.6 (a). Here, the MoO_3 powder and Se pellets, which are Mo and Se precursors, respectively, are positioned in the same alumina boat. The Ar/H_2 are used as carrier gas to vaporize Mo and Se precursors, and SiO_2/Si are chosen as substrate. This system results in large area monolayer $MoSe_2$ triangles synthesized with a length scale ~ 135 μm as shown in Figure 1.6 (c) [28]. CVD growth method is thus able to prepare 2D TMDs with large area and

high quality, and therefore is a breakthrough approach in fabrication of micro-scale 2D TMDs for the application devices.

1.4 Experimental Characterizations of Electronic properties of 2D TMDs

Experimentally, the electronic structure of 2D TMDs is investigated using photoluminescence (PL) technique. The PL spectrum enables the investigation of transitions/variations in band gap energy as TMDs are exfoliated from bulk to monolayer. For most semiconducting TMDs in 2*H* phase, such as MoS_2, WS_2, $MoSe_2$, WSe_2, etc., a striking indirect-to-direct transition in band gap is observed when they are exfoliated from

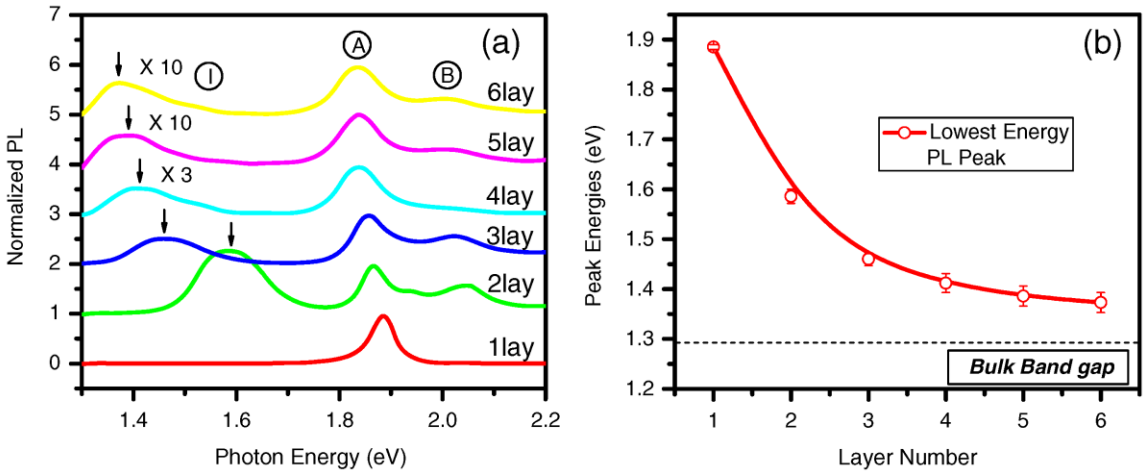

Figure 1.7 (a) The normalized PL spectra for monolayer to 6-layer MoS_2. The spectra are normalized by the intensity of peak A. (b) Bandgap energy of 2D MoS_2 structures. The bandgap of bulk MoS_2 is indicated by the dashed line. Reproduced from Ref. [29].

bulk to monolayer. It was first experimentally demonstrated using PL technique for MoS_2 [29]. As shown in Figure 1.7 (a), the indirect peak is denoted by I. The direct peaks are indicated by A and B, corresponding to the A- and B-exciton-related emissions, respectively. The PL spectrum of monolayer MoS_2 is quite distinct with that of few-layer.

Only one single narrow peak centered at 1.9 eV (corresponding to the direct transition) is observed in monolayer, while in few-layer samples, multiple peaks are observed. Moreover, the PL intensity of monolayer is substantially higher, which also suggests the direct-band-transition nature in monolayer. The bandgap energy of 2D MoS_2 decreases with the increment of layer thickness, as indicated by Figure 1.7 (b). The values of band

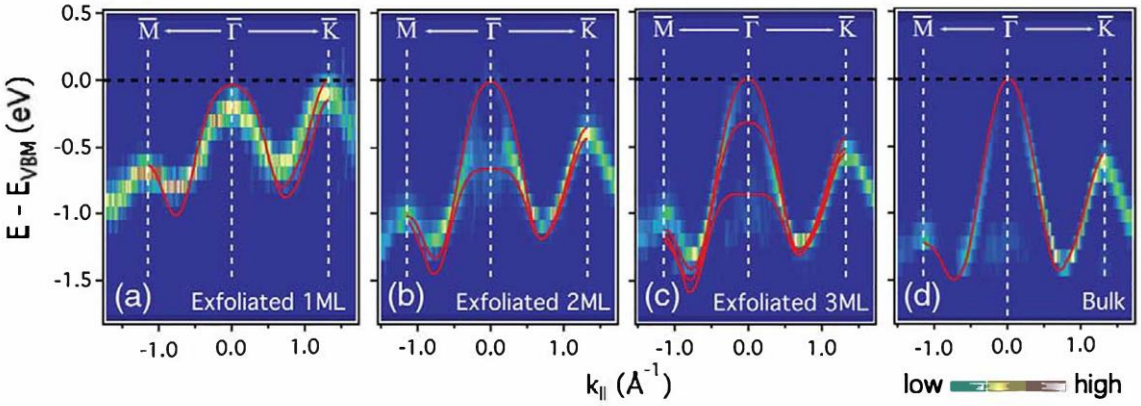

Figure 1.8 ARPES measurement of the band structure at the low energy valence bands of exfoliated MoS_2: (a) monolayer, (b) bilayer, (c) trilayer, and (d) bulk. Reproduced from Ref. [30].

gap for MoS_2 are observed to be 1.88 eV, 1.59 eV, 1.46 eV, 1.41 eV, 1.39 eV, 1.38 eV, and 1.30 eV for monolayer, bilayer, trilayer, 4 layer, 5 layer, 6 layer, and bulk, respectively.

The indirect-to-direct band transition can be also investigated using angle-resolved photoemission spectroscopy (ARPES) measurement [30]. Figure 1.8 shows the variations of the bandstructure of MoS_2 with regards to the layer thickness measured using ARPES [30]. The valence band edges are measured along the high symmetry points in the full Brillouin zone. It is clearly shown that the valence band maximum (VBM) locates at K point in monolayer, and shifts to Γ point at bilayer, trilayer and bulk MoS_2.

In addition to MoS_2, The PL spectra of other TMDs have also been studied. For example, Figure 1.9 (a) shows the PL spectra of WSe_2 as a function of layer thickness [31]. Similar to MoS_2, a direct band gap is observed for monolayer WSe_2 with a value of 1.62 eV, while the indirect band gaps are found in fewlayer and bulk structures [31]. One interesting difference in monolayer WSe_2 is that the energy of indirect peak I is almost the

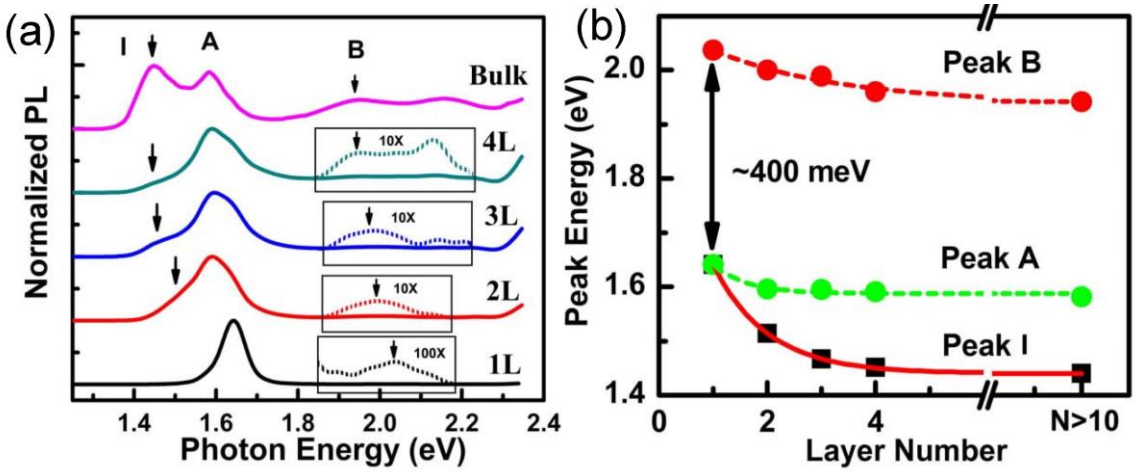

Figure 1.9 (a) The normalized PL spectra of monolayer, fewlayer, and bulk WSe_2. (b) The variations in peak positions of indirect I peak, and two direct A and B peaks as a function of layer thickness. Reproduced from Ref. [31].

same as the direct peak A, as indicated in Figure 1.9 (b). Besides, the energy gaps between two direct peaks, A and B, are observed to be 0.4 eV, which is huge as compared to MoS_2 [31].

Although experimental techniques such as PL spectrum or ARPES can provide useful insights and evidences of the variations in the electronic structures of 2D TMDs under the external strain, it is difficult and expensive to uncover the underlying physics and the origins of these variations using experiments alone. With the rapid advancements of the computational resources, it is possible to explore the complex electronic structures

using theoretical methods, such as first principle calculations based on density functional theory (DFT) [32].

1.5 Theoretical Studies of the Electronic Structure of 2D TMDs

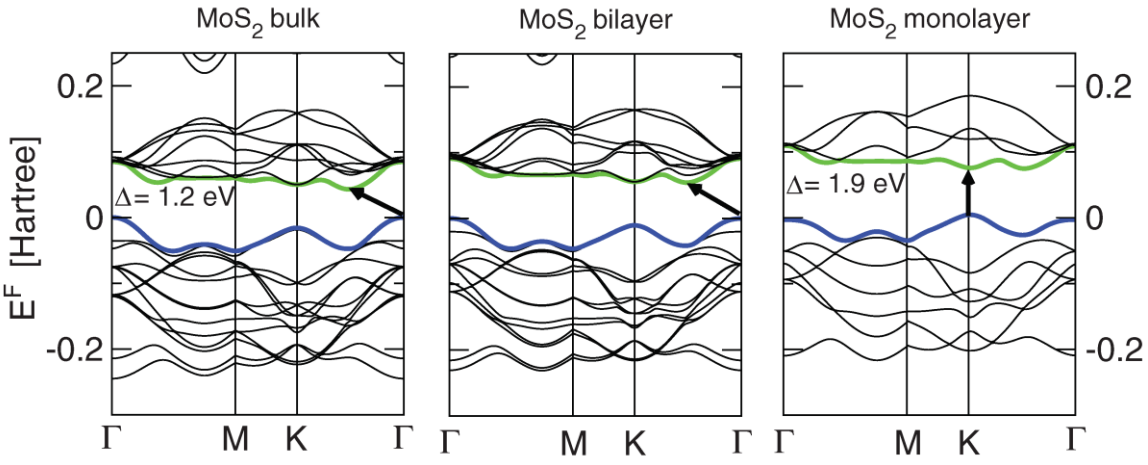

Figure 1.10 Band structures from first principle calculations based for bulk, bilayer and monolayer MoS_2. The valence and conduction band edge are colored in blue and green, respectively. Reproduced from Ref [34].

Several theoretical studies have been carried out to complement the experimental investigation of the rich physics associated with the extraordinary properties of 2D TMDs, such as the direct band gap in the monolayer TMDs, the significant spin-orbit coupling, etc. [33]. Figure 1.10 shows the band structures of MoS_2 bulk, bilayer, and monolayer calculated using DFT simulations. The valence band maximum (VBM) of bulk MoS_2 appears at Γ point, and the conduction band minimum (CBM) locates Λ point, which is between K point and Γ point [34]. This point is also denoted as Q, T, or Σ point in other references [33, 35, 36]. As a result, an indirect b1and gap is observed for bulk MoS2 attributed to the Γ−Λ transition. This value is computed to be 1.2 eV, and compares well

with the experimental value of 1.3 eV [29]. In bilayer MoS_2, the energy of K point in conduction band edge decreases as compared to the that of bulk MoS2, and the energy of K point in valence band edge shifts up as indicated in Figure 1.10. However, the band extrema of bilayer MoS_2 are not changed, still locating at Γ and Λ for VBM and CBM, respectively. As for monolayer MoS_2, the energy of K point locates below Λ point at the conduction band edge, and the energy of K point locates above Γ point at the valence band

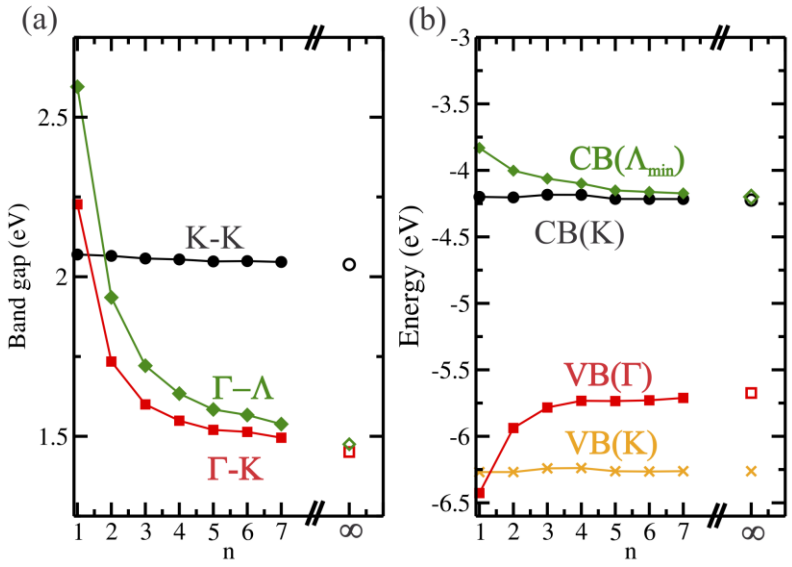

Figure 1.11 (a) The band gap transitions between critical points in BZ with respect to the layer thickness, n. (b) Band edges evolution as a function of layer thickness n. Reproduced from Ref. [41].

edge. As a result, the VBM and CBM of monolayer MoS_2 both change to the corner of the hexagonal Brillouin zone, i.e. K point. An indirect band transition of Γ–Λ observed in the bulk structure shifts to a direct K–K transition in monolayer MoS_2. The band gap of monolayer MoS2 is determined by the direct K-K transition with a value of 1.9 eV, which is consistent with the result from PL spectrum, 1.88 eV [29]. The change in the band structure from bulk to monolayer is contributed to the quantum confinement effects [37].

The quantum confinement effects are observed when the size of the nanostructures is sufficiently small to be comparable with its exciton Bohr radius [38]. For monolayer MoS_2, the Bohr radius is predicted to be 0.93 nm, which is larger than the thickness of monolayer MoS_2 (~0.6 nm) [39]. As a result, the electrons and holes in 2D MoS_2 are squeezed within the Bohr radius, which renders a faster electron-hole recombination process in monolayer and bilayer MoS_2 sheets as compared to bulk MoS_2 crystals [40]. The quantum

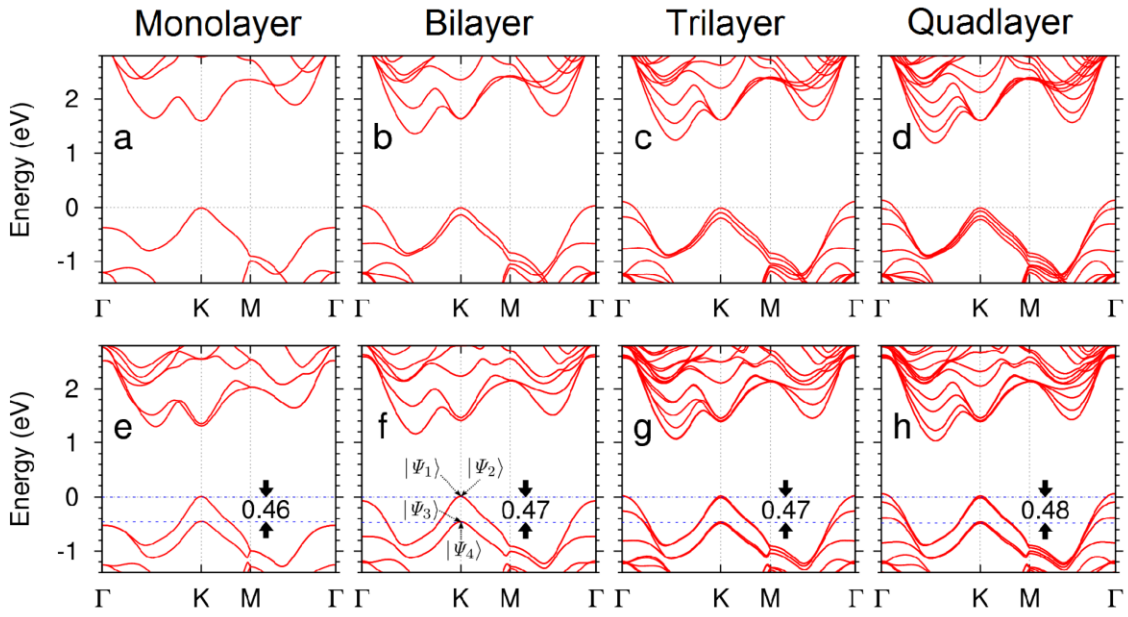

Figure 1.12 (a)-(d) The band structure of mono-, bi-, tri-, and quad- layer WSe_2 without spin orbit coupling. (e)-(h) The band structure of mono-, bi-, tri-, and quad- layer WSe_2 with spin orbit coupling. Reproduced from Ref [31].

confinement effects also result in the change in the hybridization between the p_z orbitals of S atoms and the *d* orbitals on Mo atoms [5]. The variations of band transitions and band edges for monolayer to 7-layer MoS_2 as computed using DFT [41] are shown in Figure 1.11.

As discussed before, the PL spectra of monolayer and fewlayer WSe_2 show a giant splitting in the energy difference between two direct peaks, A and B. The underlying physics can be explained by the DFT calculations. It has been shown that the energy difference of A and B peaks is purely attributed to the strong spin orbit coupling (SOC) in the d orbitals of W atom for monolayer. For the multilayer structures, in addition to the spin splitting, the interlayer coupling also plays an important role in the band splitting of the valence band edge [31]. Figure 1.13 demonstrates the significance of SOC in WSe_2 structures, which results in a band splitting around 0.47 eV at the K point of the valence band edge.

1.6 Strain Response of 2D TMDs

Recently, an emerging area of research has been the modifications of the electronic properties of 2D TMDs by environmental changes, and thus provide new opportunities in

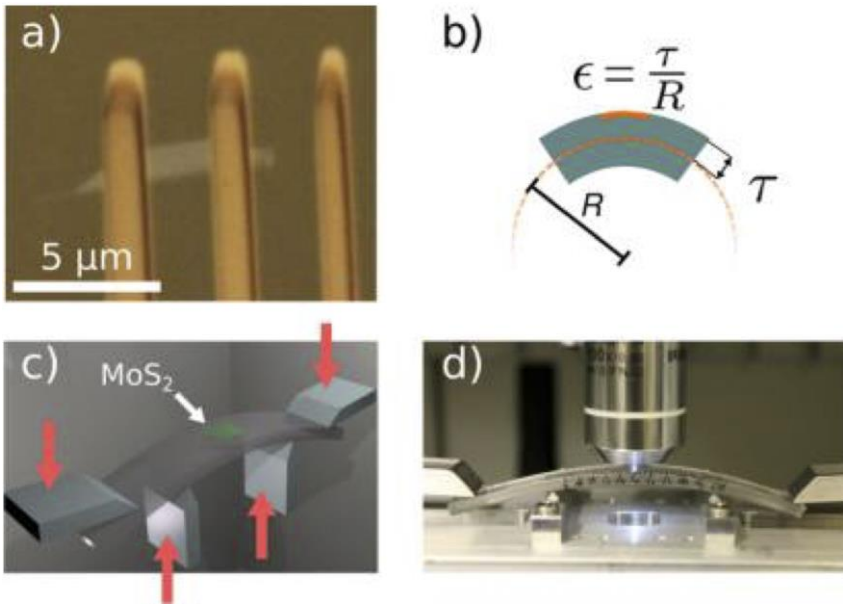

Figure 1.13 (a) Optical image of the MoS_2 bilayer attached on the substrate with the titanium clamps. (b)-(c) Schematic of the bending apparatus to apply and determine the strain. (d) Photograph of the straining apparatus. Reproduced from [46].

engineering novel devices [4]. Such a capability to alter or tune the electronic properties has been demonstrated using phase engineering [15, 42], defect engineering [43, 44] and strain engineering [45-49]. The optimization of the applicability of these 2D TMDs, therefore, hinges on a fundamental understanding of the stability and variations in the electronic structure in various environments. It is well understood that 2D materials are usually more flexible under mechanical deformations as compared to conventional 3-dimensional bulk and thin film materials. For example, nanoindentation experiments using an atomic force microscope show that ultrathin free-standing MoS_2 membranes may bear

a large in-plane strain up to 11 % before fracture [50], implying a broad operation range for strain engineering in 2D TMDs.

As a result, several efforts have focused on the investigation of the strain-induced variations in the electronic properties of 2D TMDs. Figure 1.13 provides an example to subject strain to the 2D TMDs [46]. The strain is directly subjected to the polycarbonate substrate, and the strain on the 2D TMDs samples are determined from the curvature of the

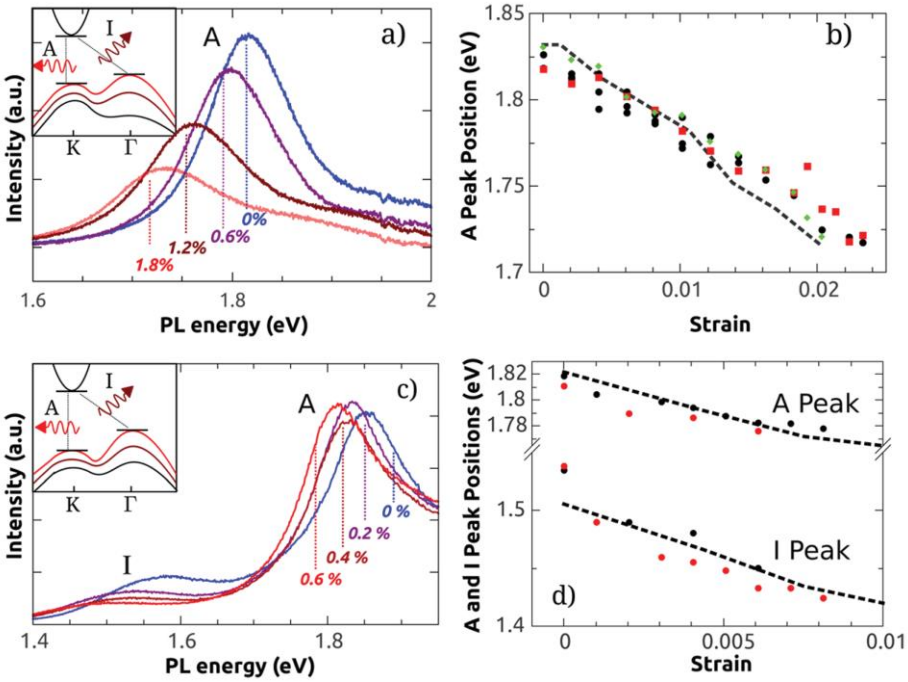

Figure 1.14 (a) PL spectra of strained MoS_2: (a) monolayer, (b) bilayer. PL peaks of (c) monolayer and (d) bilayer MoS_2 as a function of strain. Reproduced from Ref. [46].

substrate. The PL spectra of monolayer and bilayer MoS_2 are displayed in Figure 1.14 [46]. The peak A and peak I in the bilayer correspond to direct and indirect band gap, respectively. It is evident that both PL peaks of monolayer and bilayer show a linear redshift with respect to strain, i.e. the PL peaks linearly decrease with the increment strain. The redshift rates are observed to be ~ 45 meV/% for monolayer MoS_2 and ~120 meV/%

for bilayer MoS_2. Moreover, a significant reduction in PL intensity of monolayer MoS_2 is observed at an applied strain of ~1%, suggesting a strain-induced direct-to-indirect transition of the bandgap in monolayer MoS_2 [46, 51]. These results demonstrate need to identify the variations/transitions in 2D TMDs under applied strain.

The effects of strain have also been studied for bilayer WSe_2 structure using PL spectrum, as shown in Figure 1.15 [52]. Unlike the consistent blueshifts of the band gap of bilayer MoS_2 under tensile strain, the band gaps of bilayer WSe_2 is found to increase at applied tensile strains up to 1.32%, then the show a small blue shift with further strain [52].

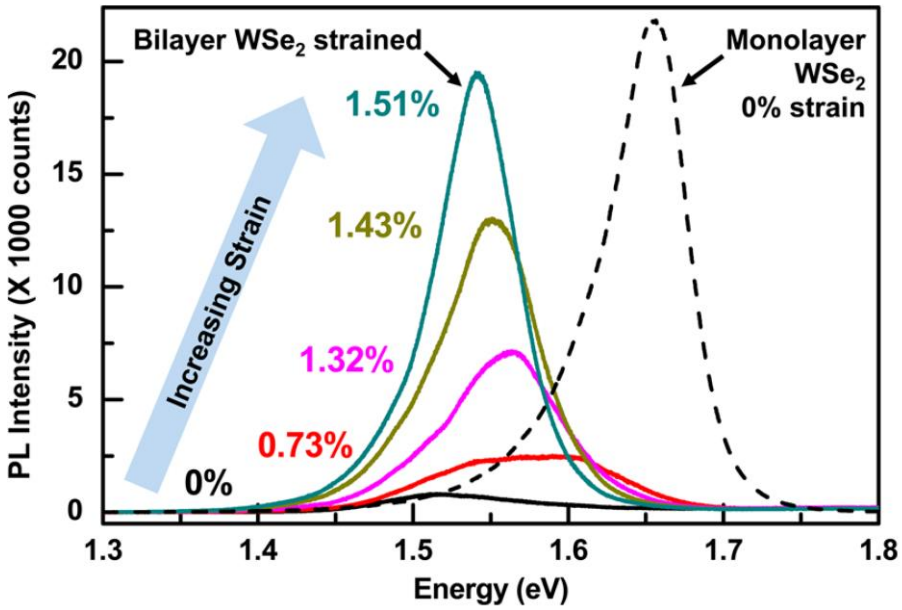

Figure 1.15 (a) PL spectra of strained WSe_2 bilayer. PL peak of unstrained monolayer WSe_2 is indicated by dashed line for comparison. Reproduced from Ref [52].

At ~ 1.5% strain, the PL intensity is observed to dramatically amplify by 25 times. Such a

strong signal is comparable to that observed in monolayer WSe2, indicating a direct band nature in strained bilayer WSe_2.

As discussed before, it becomes extremely difficult to probe the fundamental

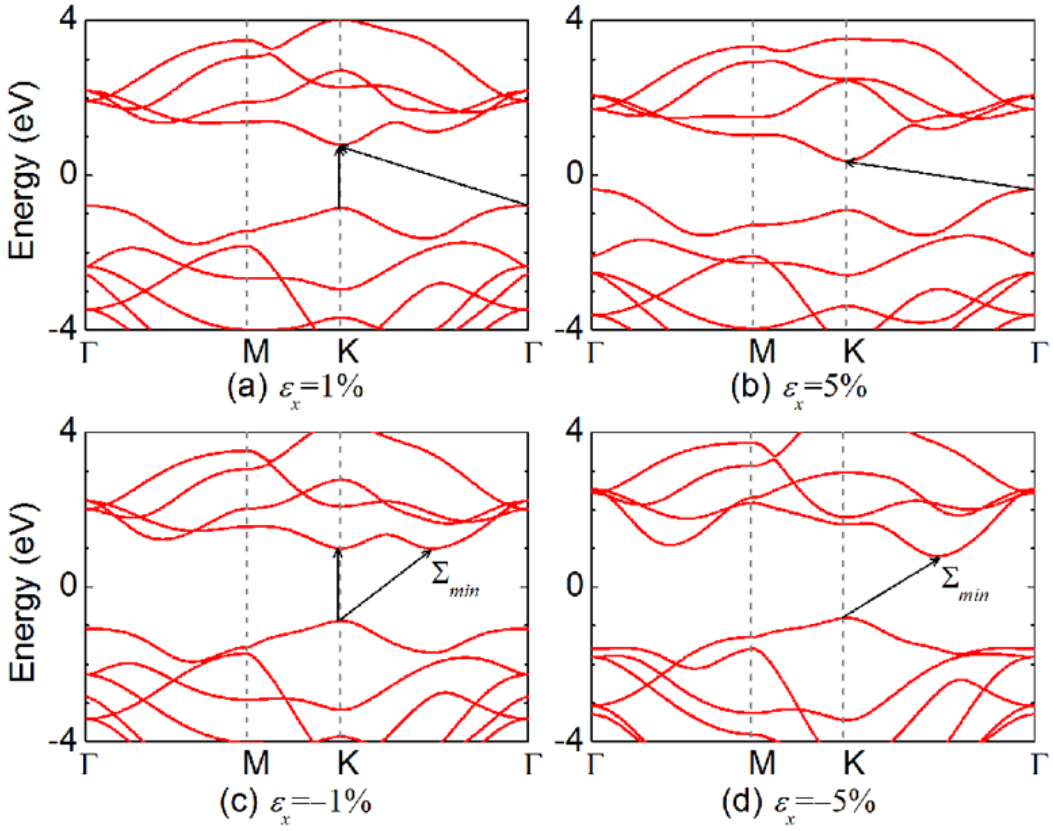

Figure 1.16 The band structure of monolayer MoS_2 at different applied strains: (a) 1%, (b) 5%, (c) -1%, and (d) -5%. Reproduced from Ref. [36].

characteristics that render the variations in the band gap energies under various strain conditions using experiments alone. As a result, several computational studies using density functional theory (DFT) have aimed to investigate the variations in the band gap energies, the various bandgap transitions, as well as carrier mobility for monolayer and bilayer MoS_2 under varying strain conditions [20, 36, 53-57]. For monolayer MoS_2, ab initio calculations predict a similar trend of 40-100 meV/% blue shift rate [20, 36, 54-57], and suggest a direct−indirect transition under both tensile and compressive strains [36].

Figure 1.16 shows the variations in band structure of monolayer MoS_2 at tensile and compressive strain. It can be seen from Figure 1.16 that the direct K–K band gap shifts to indirect Γ–K band transition at an applied tensile strain of ~ 1% [36]. While at the compressive strain domain, the CBM changes to Σ_{min}. As a result, an indirect K– Σ_{min} band gap is observed at applied compressive strain greater than 1%.

The band gap energy (E_g) is observed to decrease under tensile strain/stress

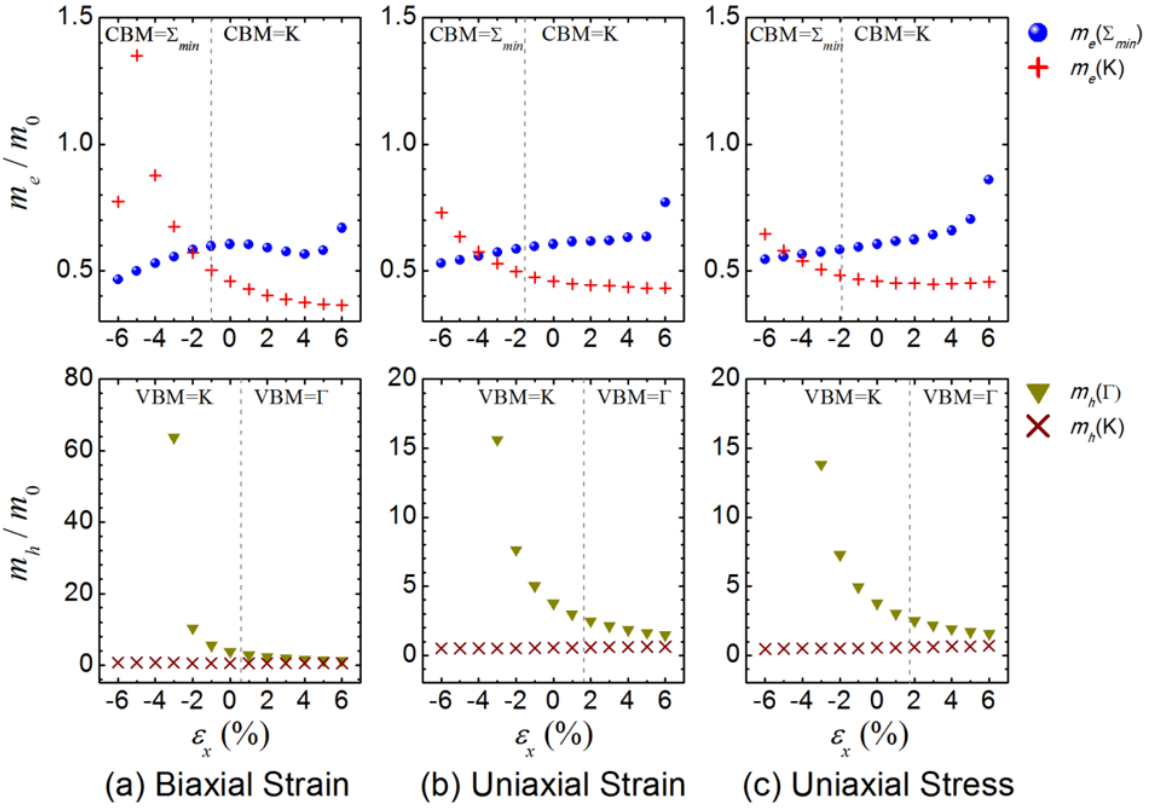

Figure 1.17 The variations of effective mass as a function of strain at different loading conditions: (a) biaxial strain, (b) uniaxial strain, and (c) uniaxial stress. Reproduced from Ref. [36].

conditions, while for an in-plane compression E_g is initially raised by a small amount and then decreased as the strain varies from 0 % to −6 % [36]. The strain effects on effective

carrier masses of monolayer MoS_2 have also been studied, as shown in Figure 1.17 [36]. A tensile strain/stress tends to reduce m_e at CBM (K), but introduce an abrupt increase in m_h (VBM from K to Γ). On the other hand, a compressive strain/stress tends to reduce m_h at VBM (K), but introduces an abrupt increase in m_e (CBM from K to Σ_{min}) [36]. DFT simulations also show a significant enhancement in the electron mobility (over 10 times) under biaxial tensile strain [58], which can be employed to improve the transport characteristics [59].

Similarly, DFT simulations suggest an indirect band gap for bilayer MoS_2 for all variations of strain along the basal plane [54]. In addition, several transitions for the indirect band gap are observed for various strains for the bilayer structure [34]. These studies are consistent with the experiments that E_g of bilayer MoS_2 is blue shifted under a uniaxial strain.

1.7 Strain Response of CVD-grown TMDs

As discussed before, the recent advancements in the capability to successfully grow high-quality 2D TMDs using CVD further enhance the applicability of these 2D structures for applications in the next-generation field-effect transistors, phototransistors, as well as spintronic devices [31, 60, 61]. The experimental as-grown structures during chemical vapor deposition comprise of multiple layers with unequal dimensions. An example as-grown bilayer flake of MoS_2 using CVD is shown in Figure 1.18 (a) [62]. It can be seen

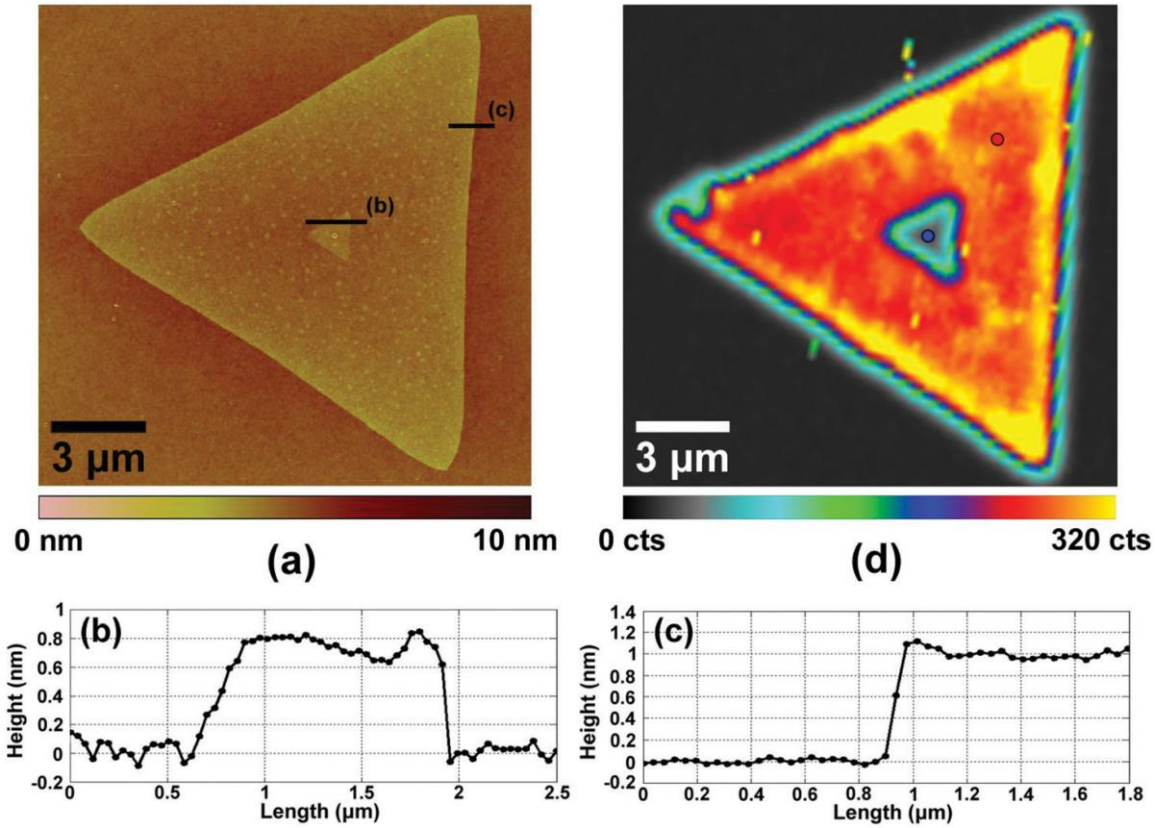

Figure 1.18 (a) AFM image of CVD-grown bilayer MoS_2. Step height measurement (b) from monolayer to bilayer, and (b) from SiO_2/Si substrate to monolayer. (d) PL intensity map of MoS_2 bilayer. Reproduced from Ref. [62].

from this image that the bilayer flake comprises of a bottom layer as a triangle and the top layer that is also a triangle with smaller dimensions as compared to the bottom layer [62].

Such structures result in regions that resemble a bilayer structure at the center surrounded by regions that are simply a monolayer MoS_2 structure. The monolayer to bilayer step is measured to be 0.7 nm, which is typical thickness of a MoS_2 layer. Interestingly, the substrate to monolayer step is measured to be 0.9 nm, which is remarkably larger than the thickness of single layer MoS_2. Such a difference suggests that the interlayer bonding between SiO_2/Si substrate and monolayer is weak as compared to that between two MoS_2 layers. Similarly, a CVD-grown few-layered MoS_2 flake shows several layers of unequal

dimensions with the largest layer at the bottom, and the smallest layer at the top. The PL intensity map of the CVD-grown bilayer is displayed in Figure 1.18 (d) [62]. Noticeable differences in PL intensity are observed in edges of monolayer and bilayer triangles. The PL signal at the edges is substantially smaller, which indicate the electronic properties of bilayer MoS2 is modified at the presence of edge.

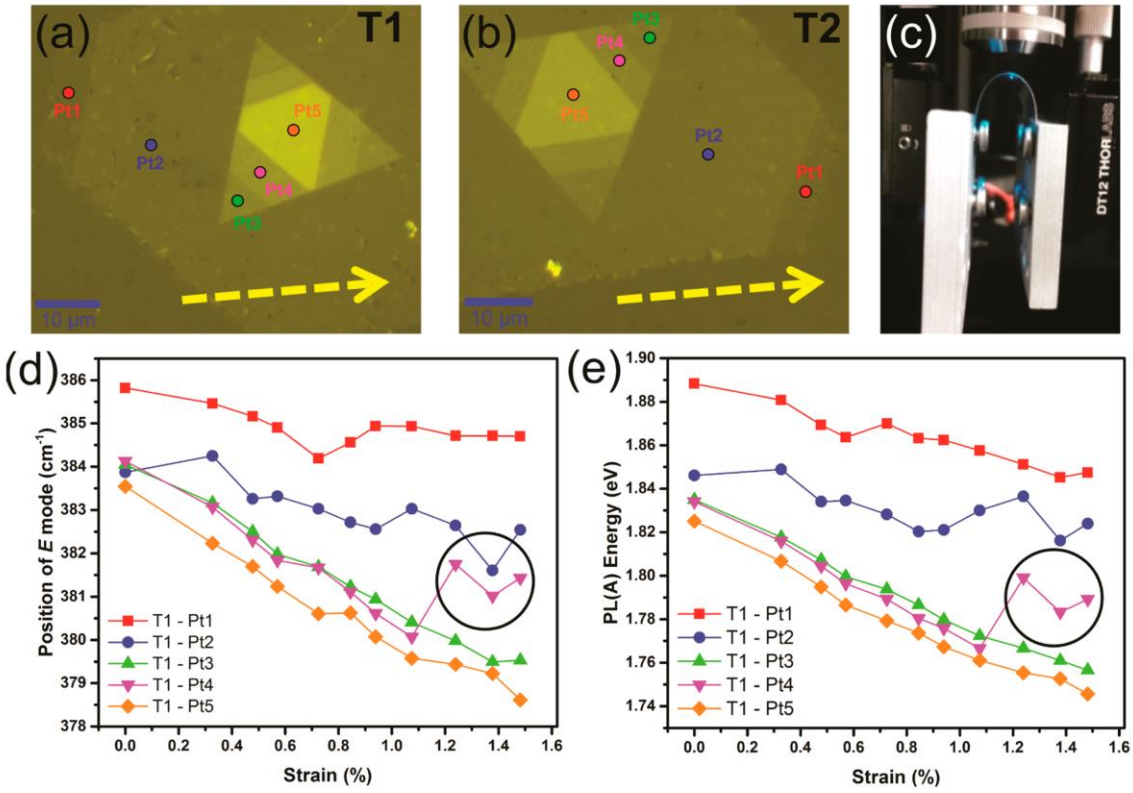

Figure 1.19 Optical images of two MoS_2 multilayer (a) and (b). (c) Photograph of the strain system. (d) The position of E mode of Raman spectrum and (e) the PL energy as a function of uniaxial strain. Reproduced from Ref. [63].

An example as-grown five-layer MoS_2 flake using CVD is shown in Figure 1.19 (a) and (b) [63]. Five triangles are stacked to form a multilayer structure, and the dimensions of the triangular layers are decreasing with each increasing layer. The effects of strain on the electronic properties of these multilayered structures may therefore lead to variations

in the band gap energies across the monolayer and bilayer regions. As the top layers are weakly bound to the bottom layers through vdW interaction, the presence of the edges is likely to affect the relaxation behaviors of the multilayered structures, and the behavior of the top layers is likely to be different from that of bottom. Therefore, the response of such 2D structures (with unequal dimensions) is likely to create an inequality in the amounts of strain across the layers and hence is likely to exhibit inhomogeneous electronic properties.

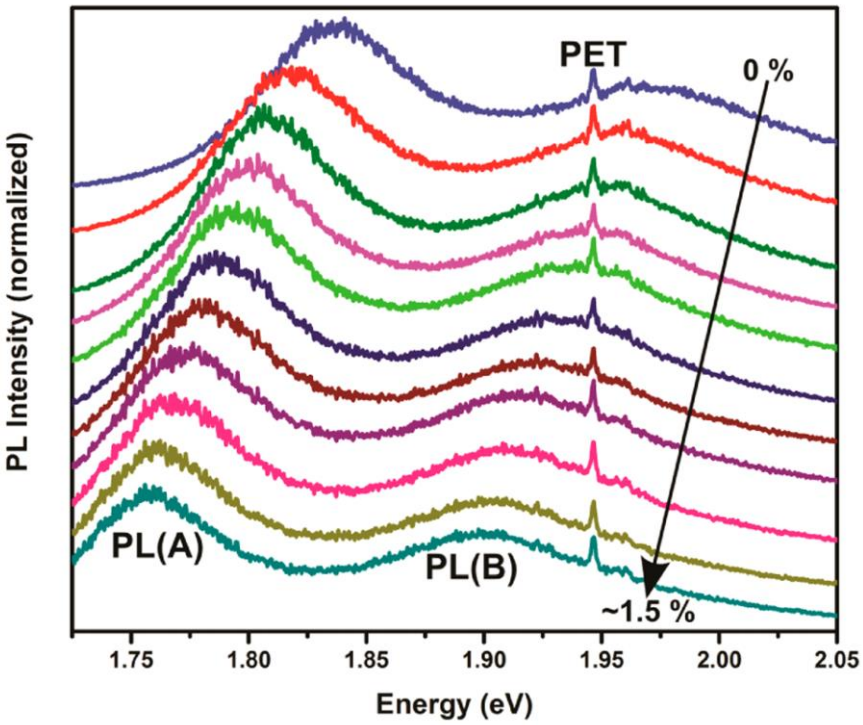

Figure 1.20 PL spectra of Pt 3 on T1 (trilayer) as a function of applied uniaxial strain. Reproduced from Ref. [63].

The CVD-grown five layered MoS_2 flakes on PET substrate as shown in Figure 1.19 (a) and (b) have been subjected to strains under loading conditions of both uniaxial and biaxial strains [63]. Two multilayered structures as referred to triangle 1 (T1) and triangle 2 (T2) are studied. Each point (Pt) corresponds to one layer with Pt1 being monolayer and Pt5 being fivelayer structure. The terrace triangles (T1 and T2) are placed

on PET substrate, and the strain is directly subjected by bending the PET substrate. The applied strain on T1 and T2 are estimated by the strain on PET, the distance between two plates, and the angle at the minimum strain point [63]. The PL spectra as the function of applied uniaxial strain is shown in Figure 1.20. It can be seen that two peaks, corresponds to two K–K transitions splitting at K point at valence band edge, have been observed for the trilayer point at the multilayer system. Both peaks show blue shift behavior with respect to the strain. Figure 1.19 (e) illustrates the variation of the positions of PL(A) peak as a function of applied strain. It is interesting to note that the strain response of CVD-grown few-layered MoS_2 structures shows a hysteretic shift of the in-plane Raman peak position and PL energy at a large applied strain (Figure 1.19) [63]. This shift occurs at random

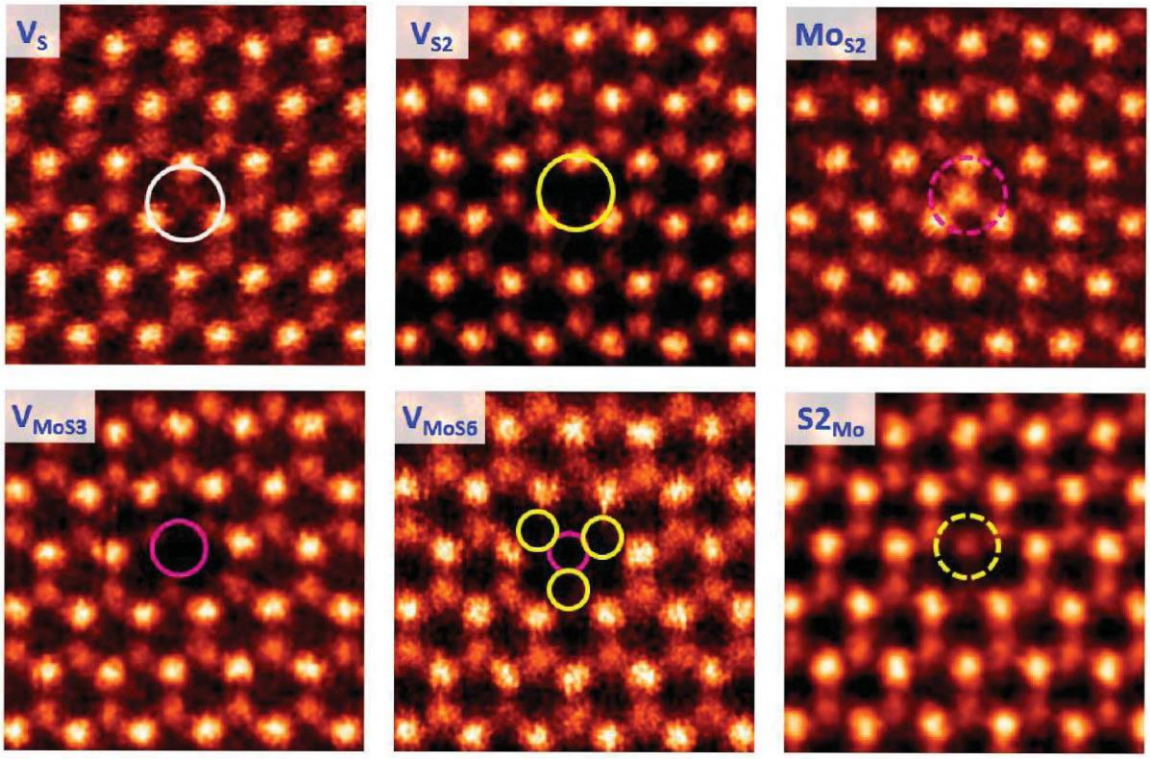

Figure 1.21 Atomic resolution ADF image of intrinsic defects found in CVD-grown monolayer MoS_2. Reproduced from Ref. [64].

layers (layer 4 in Figure 1.19). It is speculated that this local shift may be originated from the sliding of local regions with defects. As a result, the role of defects on the sliding energy barrier of bilayer MoS_2 is investigated.

It is now known that the CVD-grown TMDs result in the presence of the intrinsic defects, such as vacancies, interstitials and grain boundaries that are inevitable to form during the growth process [64]. Figure 1.21 shows the atomic resolution STEM-ADF images for six types of point defects seen in the CVD-grown monolayer MoS_2 [64]. These intrinsic defects include monosulfur vacancy (V_S), disulfur vacancy (V_{SS}), vacancy complex of Mo and surrounding three sulfur atoms in one plane (V_{MoS3}), vacancy complex of Mo and its six first-nearest neighboring sulfur atoms (V_{MoS6}), and antisite defects where a Mo atom substituting a S_2 column (Mo_{S2}) or a S2 column substituting a Mo atom ($S2_{Mo}$). It has been demonstrated that the presence of defects significantly modifies the electronic,

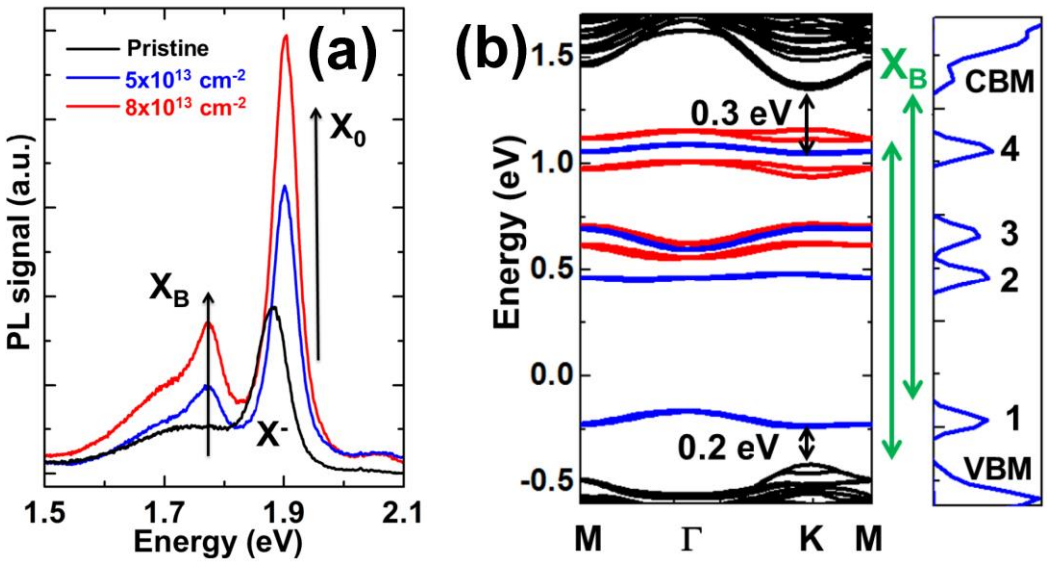

Figure 1.22 (a) PL spectrum of pristine and irradiated monolayer MoS_2. (b) Calculated band structure and density of states for monolayer MoS_2 at the presence of disulfur vacancy. Reproduced from Ref. [65].

optical and transport properties of 2D TMDs [43]. For example, an additional peak positioned at 1.78 eV, X_B, is observed in PL spectrum of irradiated monolayer MoS_2 by α-particles (Figure 1.22 (a)) [65]. The signal of this peak is enhanced at a larger irradiation dose of α-particles. In addition, the intensity of main PL peak at 1.9 eV (X_0) increases by three times due to the irradiation/defects. The theoretical simulations based on DFT methods confirm that additional charge states appear within the mid gap region for monolayer MoS_2 at the presence of disulfur vacancy [65]. As shown in the density of states (DOS) of monolayer MoS_2 with V_{SS} vacancy in Figure 1.22 (b), four defect states are observed between CBM and VBM. The optical transitions from CBM to peak 1 and from peak 4 to CBM (indicated by green arrows) are 0.2 eV and 0.3 eV lower than the X_0 peak. As a result, these transitions are speculated to be related to the X_B peak observed in the PL spectrum, which is 0.12 eV lower than X_0 [65]. Therefore, the electronic and optical properties of 2D TMDs are remarkably modified at the presence of defects. However, the previous studies of effects of defects have been limited on monolayer TMDs, while the role of defects on bilayer TMDs remain unknow. It is not clear whether the modification in electronic structures in the defective layer may transfer to its adjacent pristine layer. As a result, the role of defects is also studied in this thesis.

Recently, a few studies have reported the observation of ripples near edge terminals in CVD-grown multilayer MoS_2 structures as shown in Figure 1.23 [66]. The STM images indicate that typical height of these ripples is ~11 Å (Figure 1.23 (d)), while the spectroscopy (STS) measurements suggest that these ripples result in the reduction of band gap of the MoS_2 sheets near edge terminals from 1.96 eV to 1.46 eV [66]. Since the locations of the ripples are observed at the edges, it is likely that the formation of ripples is related to the displacement of atoms at the edges. A recent study has also observed ripples

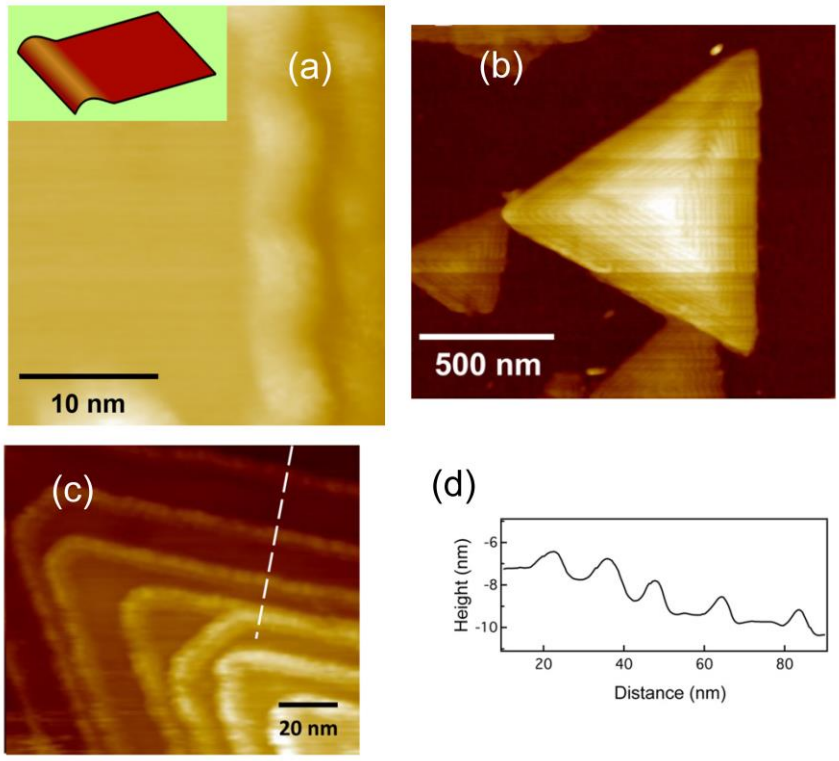

Figure 1.23 (a) STM images of the curved MoS_2 few-layer structure on GaN substrate. (b) AFM images of multilayer MoS_2. (c) Constant current STM image of the MoS_2 multilayer; (d) The thickness profile along the dashed white line in (c). Reproduced from Ref. [66].

in a CVD-grown bilayer structure in Figure 1.24 (a) [67]. The arrays of ripples with a typical height of 1 nm can be clearly seen from the AFM image as shown in Figure 1.24 (b) and (c). The ripples are found to be attributed to the residual biaxial strain across layers

due to the interlayer coupling during the grown process. The PL intensity map show a star-shaped signals in bilayer structure, indicating an interesting strain response. The PL spectrum shown in Figure 1.24 (e) demonstrates a 42 meV blue shift in PL peak position of nanoripples as compared to those in pristine monolayer MoS_2. Such a blue shift is equivalent to the effects of ~ 0.7% strain. As a result, the ripples formed in bilayer structure are likely to relate to the strain. However, the underlying mechanisms of the formation of ripples at a large atomic scale (~ 100 nm) are still not clear.

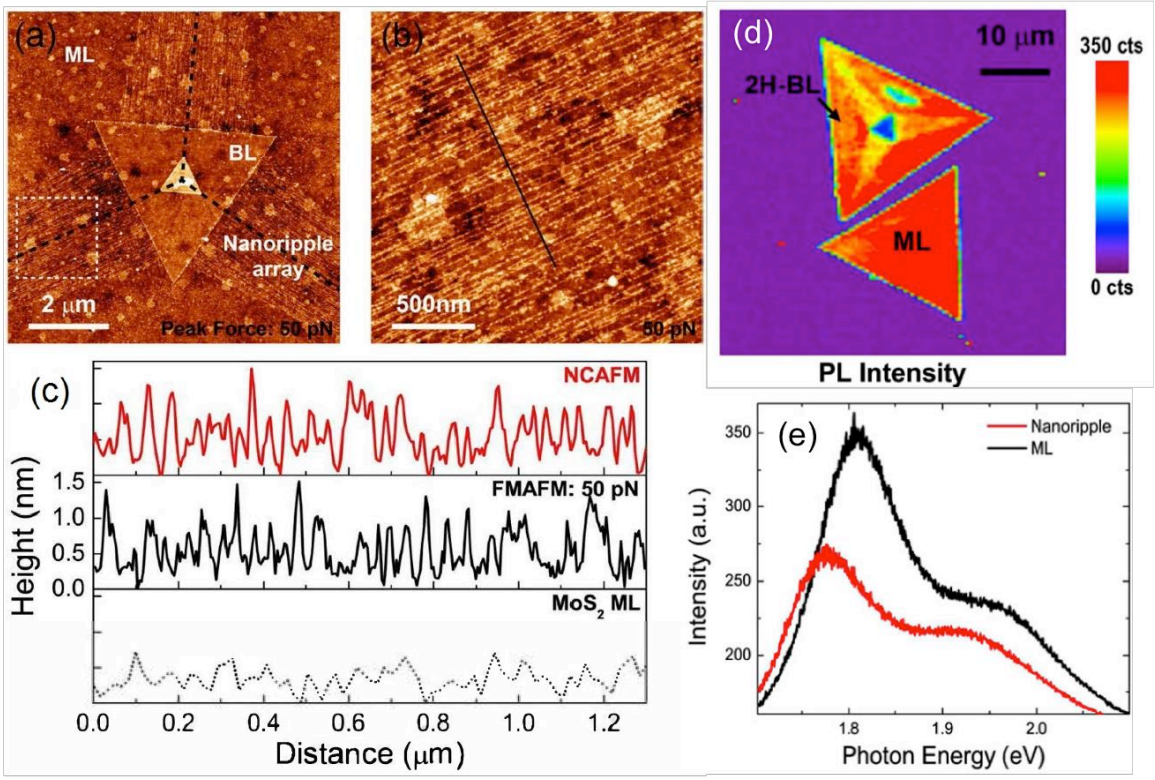

Figure 1.24 (a) AFM of nanoripple arrays (NRAs). (b) Zoom in over the dashed square in (a). (c) AFM heights show corrugations of NRAs. PL map (d) and spectra (e) of NRAs as compared to pristine monolayer MoS_2. Reproduced from Ref. [32].

In addition, when the CVD-grown multilayers are subjected by external strain, the incomplete strain transfer across layers may also lead to the different strain configuration in each layer. Such a vertically heterogeneous strain response can induce a lattice mismatch between different layers. As a result of this mismatch, a Moiré-like superstructure is observed in individual layers, i.e., Moiré pattern. The lattice-mismatched Moiré-pattern structures are considered as the evidence of successful alignment/growth of heterostructures, and have been extensively observed in many vdW heterostructures [68-72], graphene-metal interface [73] as well as MoS_2-metal interfaces [74-77]. For example, rotationally aligned MoS_2-WSe_2 bilayer shows a Moiré pattern with a well-defined periodicity of ~8.7 nm, as shown in Figure 1.25 [72].

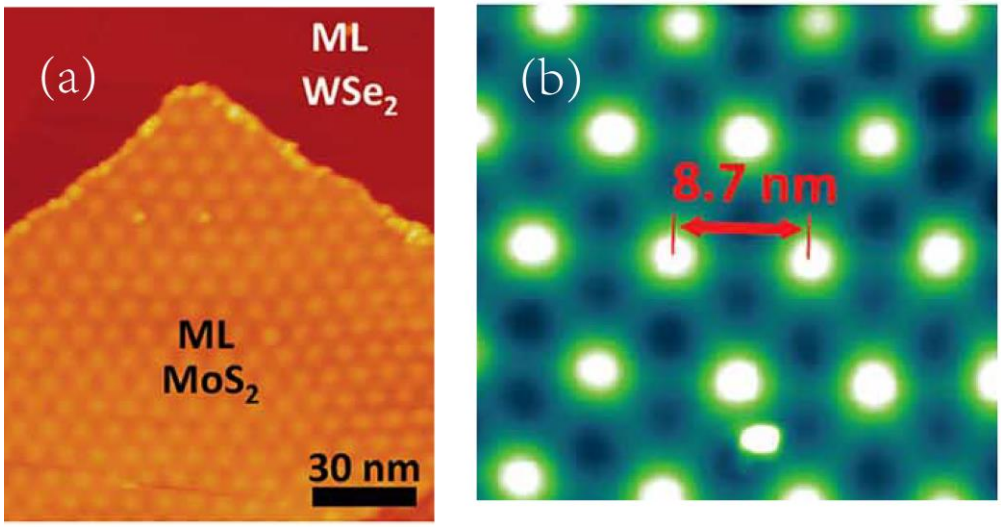

Figure 1.25 (a) STM images of MoS_2/WSe_2 heterostructure. (b) Close-up STM image show the Moiré pattern with a periodicity of ~8.7 nm. Reproduced from Ref. [68].

While most of the current discussions have focused on MoS_2 systems, strain response of other 2D TMDs such as HfS_2 and WSe_2 has also been recently investigated. For example, a strain-induced indirect-to-direct transition has been observed for bilayer WSe_2 using PL techniques [52]. It was reported that a crossover from indirect band gap to

direct one occurred at an applied strain of 2% that resulted in a dramatic enhancement in PL intensity in strained structures [52]. However, our experimental collaborators, Wei Wu and Prof. Michael Pettes, observe a distinct phenomenon for bilayer WSe_2. As shown in Figure 1.26 [52], no crossover of direct and indirect band transition is found up to 3.5% uniaxial tensile strain. The reason of the discrepancies between Wu et. al. and Desai et. al. [52] remains unknown.

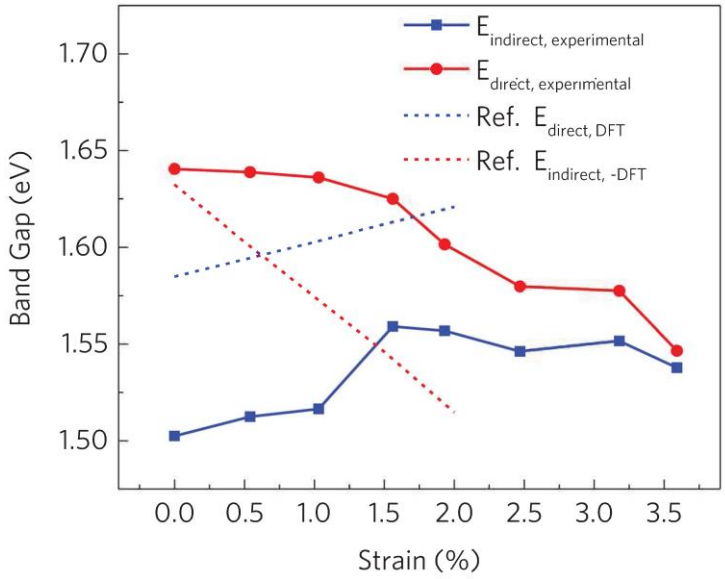

Figure 1.26 The direct and indirect band energies of bilayer WSe_2 at different uniaxial tensile strains. The reference DFT results are from [52].

1.8 Goal of Thesis

Thus, based on the experimental and theoretical results in the literatures, it can be seen that the understanding of the strain response of 2D TMDs is still in an infancy. This dissertation aims to use atomic scale modeling methods to investigate the correlations between structure and electronic properties of 2D TMDs, and the modifications due to applied strain. The details of the computational methods are given below.

1.8.1 Density Functional Theory

Density functional theory (DFT) is a quantum mechanical methods based on the famous Hohenberg and Kohn theorem [32]. It is known for successful description of the ground state properties of atoms, molecules, and solids with reasonable computational efforts and surprising accuracy. DFT is inherently parameter-free and requires no experimental input and thus has often be considered as a benchmark for other non-ab-initio methods. Therefore, DFT has rapidly become a most popular computational approach in materials science and has been shown to be able to accurately predict structural and geometrical details, elastic constants, vibrational frequencies and phase transformation behavior, especially for periodical solid systems [78].

Using Hohenberg-Kohn theorems [32], the Hamiltonian of a many-electron system, with Born-Oppenheimer approximation, is expressed as a functional of electron density rather than wave function based on two theorems:

Theorem 1: The external potential (and hence the total energy), is a unique functional of the electron density.

Theorem 2: The functional that delivers the ground state energy of the system, gives the lowest energy if and only if the input density is the true ground state density.

Based on these two theorems, there exists a universal functional of the density, denoted as H-K functional $F[n(r)]$, such that the global minimum value of the energy functional

$$E[n(r)] = \int n(r) V_{ext}(r) dr + F[n(r)] \tag{1.1}$$

is the exact ground-state energy of the system and the exact ground-state density minimizes this functional. As a result, the grand-state energy and density are fully dependent on the functional $E[n(r)]$.

Although the Hohenberg-Kohn theorems can simplify the many-body interactions in terms of the density as the basic variable, the unavailability of the universal H-K functional make it impractical. The huge progress came from Kohn-Sham approach in 1965 [79], in which the ground-state density of the interacting system is assumed to equal that of a fictitious non-interacting system with all the difficult many-body terms incorporated into the exchange-correlation functional of the density.. As a result, the DFT is practically implemented within the Kohn-Sham framework. The interacting many-body electron problem can be solved self-consistently in terms of a set of Kohn-Sham equations of auxiliary non-interacting system,

$$\left[\frac{-\hbar^2}{2m}\nabla^2 + V_{ext}(r) + V_H(r) + V_{XC}(r)\right]\phi_i(r) = \epsilon_i\phi_i(r) \tag{1.2}$$

where $V_{ext}(r)$, $V_H(r)$, and $V_{XC}(r)$ are the interaction potential of an electron with nuclei (Hartree potential), the interaction potential of an electron with other electrons, and the exchange-correlation potential, respectively. $\phi_i(r)$ is the one-electron wavefunction. Then the charge density can be determined by

$$n(r) = \sum_i^N |\phi_i(r)|^2 \tag{1.3}$$

The original many-body electron problem is ingeniously converted to a non-interacting one electron problem, with the interacting part incorporated in the exchange-correlation potential. In practical, the exact form of exchange-correlation functional is unknown, but various approximation can be made to estimate the exact exchange-

correlation functional, such as the local density approximation (LDA) [79] and the generalized gradient approximation (GGA) [80]. LDA depends only on the density at the local coordinates, whereas GGA also takes into account the local gradient of the density. In general, the LDA should be used when the electron density slowly varies. The LDA usually underestimate bond lengths and band gaps, and overestimate biding energies [81]. GGA generally works better than LDA in bond lengths and binding energies, but still underestimate the band gaps [81]. The most common version of GGA is PBE, a parameter-free GGA proposed by John P. Perdew, Kieron Burke and Matthias Ernzerhof [80].

It is known that in general GGA underestimates the absolute band gap energy of semiconductors [82]. The calculated E_g of the infinitely large bilayer MoS_2 sheet is about 0.4 eV lower than the experimental value (1.6 eV) [83]. Such an underestimation may be corrected or reduced by using modern time-intensive hybrid functionals (e.g., HSE06 [84]) or the quasiparticle GW approximation [85] for many other semiconductor materials [86]. For monolayer and bilayer MoS_2 crystals, however, both HSE06 and GW approaches were found to overestimate the band gap energy by 0.3~1.0 eV [87-91]. Based on these facts, the relatively simpler GGA is employed in our analysis because I focus primarily on the *relative variations* in the electronic properties of bilayer MoS_2 under different strain/stress conditions. For this purpose, results of different levels of theory are in mutual agreement with each other. It is well known that none of the existing popular DFT functionals (e.g., PBE and HSE06) are capable of describing the long-range vdW interactions [92]. As a consequence, they fail to yield correct results of the lattice parameters or the elastic properties of bulk MoS_2 [93]. In This study, the conventional DFT energy is supplemented with a pairwise interatomic vdW potential which is determined by Tkatchenko and

Scheffler (TS-vdW) from non-empirical mean-field electronic structure calculations [92] to reproduce the structures and energetics of 2D materials. More details are provided in chapter 2.

The evolutions of microstructures of these 2D CVD-grown structures with respects to strain require sufficiently large model/supercell to accommodate the complex strain transfer across different layers. While DFT simulations can provide insights in the effect of the presence of edges on the variation in the electronic structure and strain configuration, these simulations are limited to system size on the order of a few nanometers. It is likely that the effect of the presence of edges on the strain relaxation and the resulting electronic structure is more significant at the nanoscale dimensions of the layers and less significant at the micron scale dimensions as observed experimentally. As a result, classical molecular dynamics (MD) simulations are performed in this thesis to study the strain response of CVD-grown MoS_2 structures at the experimental length scales.

1.8.2 Classical Molecular Dynamics

Molecular dynamics (MD) is a classical mechanics based methods which treats atoms as hard sphere particles and solves Newton's equation of motions to obtain their trajectories [94]. The force on atom *i* is determined from the gradient of the potential:

$$F_i = -\nabla_i U \tag{1.5}$$

Then the acceleration of atom *i* is calculated by the Newton's law:

$$a_i = F_i / m_i \tag{1.6}$$

where m_i is the mass of atom i. Take the third order of Taylor series of the position of at time t:

$$r(t+\Delta t) = r(t) + v(t)\Delta t + \frac{1}{2}a(t)\Delta t^2 + \frac{1}{3!}\dddot{r}(t)\Delta t^3 + O(\Delta t^4) \tag{1.7}$$

$$r(t-\Delta t) = r(t) - v(t)\Delta t + \frac{1}{2}a(t)\Delta t^2 - \frac{1}{3!}\dddot{r}(t)\Delta t^3 + O(\Delta t^4) \tag{1.8}$$

add (1.7) and (1.8), the position of the next timestep $t + \Delta t$ is

$$r(t+\Delta t) = 2r(t) - r(t-\Delta t) + a(t)\Delta t^2 \tag{1.9}$$

Equation (1.9) indicates that $\mathrm{r(t+\Delta t)}$ is expressed with the previous $\mathrm{r(t-\Delta t)}$ and current $\mathrm{r(t)}$ positions and the current acceleration $a(t)$. And the velocity of the current timestep can be estimated by:

$$v(t) = \frac{r(t+\Delta t) - r(t-\Delta t)}{2\Delta \mathrm{t}} \tag{1.10}$$

Once the initial positions (initial structure) and velocities (e.g. from Boltzmann distribution) are given, the forces, accelerations, position, and velocities of the next timestep can be determined through equation (1.5) to (1.10). As a result, the complete trajectories of the system are available.

As a result, the only input of MD calculation is the interatomic potential energy, U, which is usually fitted from ab-initio calculations such as DFT. The applicability and reliability of MD calculation rely on the availability of the interatomic potential. For MoS_2, the reactive empirical bond-order (REBO) potential is chosen to describe in-plane covalent interaction of Mo-S system, because it is able to provide an accurate description of the structural energetics for bulk MoS_2 (the in-plane lattice parameter *a*, the vertical S-S distance *d*, and the intra-layer lattice parameter *c*) as well as the bond breaking and

formation processes at extreme tensile and compressive stresses [95, 96]. The out-of-plane van der Waals (vdW) interaction between adjacent layers is described by pairwise Lennard Jones (LJ) potential.

1.8.3 Key Questions being Addressed in this Thesis

The understanding of the links between strains, structure, and electronic and mechanical properties in 2D TMDs will allow for the possibility of unprecedented performance improvements for the miniaturized electronic devices. The central focus of this dissertation is on the strain engineering of CVD-grown 2D TMDs, which undertakes several important tasks to gain a fundamental understanding of the relationship between the atomic scale structure, chemistry, strain and the electronic and mechanical properties of various configurations of CVD-grown 2D TMDs using DFT and MD simulations. These questions are listed below:

A. What are the effects of applied strain on the electronic structure of CVD-grown MoS_2 structures? The variations of band gaps at different regions of the as grown bilayer (monolayer, bilayer or edge region) will be investigated as a function of strain using DFT simulations. The local variations in band gap will be investigated and the strain configuration will be discussed.

B. What roles do defects play in modifications of electronic and mechanical properties of CVD-grown MoS_2 structures? The questions will be addressed using DFT simulations of MoS_2 bilayer with defects. The modifications in electronic properties will be investigated by defect charge states whereas the mechanical

properties will be studied by computing the energy barrier required for sliding in various types of defect MoS_2 bilayers.

C. What are strain response for CVD-grown MoS_2 multilayer at the length scale that is close to experiment? What is the possible mechanism for strain relaxation in these 2D structures? What are the atomic scale mechanisms related to the formation of ripples in CVD-grown MoS_2 structures? The evolution of microstructures of CVD-grown multilayer structures will be studied using MD simulations. The origin of ripples will be uncovered from the microstructures at different applied strains.

D. What are the strain response of CVD-grown bilayer MoS_2 stacked triangles with a realistic edge configuration? What is the role of substrate in transferring strains? What are the atomic scale mechanisms related to the emergence of Moiré patterns? The questions will be addressed using MD simulations. The emergence of Moiré patterns and their correlations to strain relaxation will be discussed.

E. What are the effects of applied strain on the electronic structure of bilayer WSe_2 and 2D HfS_2? The question will be addressed using DFT simulations to study the band structure and band transitions of these 2D TMDs with respects to strain.

As a result, the strain response of CVD-grown MoS_2 structures will be investigated using two methods: (1) DFT method to study the modifications in electronic structures under various conditions related to strain engineering of CVD-grown structure; (2) MD method to prove the underlying mechanisms of the strain response of CVD-grown structure at the experimental length scale. The remainder of the thesis is organized as follows.

1.9 Summary of Chapters in this Dissertation

In chapter 2, the strain dependence of the electronic properties of bilayer sheets of CVD-grown 2*H*-MoS_2 is studied using DFT simulations. The variations in the local electronic structure (local density of states) due to the presence of edges are studied under varying strain conditions. The variations in band gap energies are observed across the layers under a tensile uniaxial strain, although they remain mutually interacting by vdW interactions. The deviation in their band gap energies grows from 0 to 0.42 eV as the uniaxial strain increases from 0% to 6% under both uniaxial strain and stress conditions. The deviation, however, disappears if a compressive uniaxial strain is applied.

Chapter 3 discusses the role of presence of various types of vacancy defects on the modifications in the local electronic structure of bilayer MoS_2 using DFT calculations. DFT calculations suggest that additional charge states are activated in the gap between the valence band and conduction band for the atoms neighboring the defects in the layer and in the layer above the defects. In addition, the DFT results indicate that the presence of a local defect lowers the energy barrier for strain relaxation of bilayer MoS_2 attributed to sliding between the layers.

Chapter 4 investigates the atomic scale mechanisms related to the formation of ripples in CVD-grown MoS_2 structures using MD simulations. The model comprises of free standing few-layer MoS_2 with complex edge configurations to mimic CVD-grown structures. MD simulations suggest that the CVD-grown structures are able to relax the applied in-plane strain through the nucleation of ripples at the various edges that propagate inwards under both tensile and compressive loading conditions. The origins of ripples are

found to be attributed to the presence of edges as MD simulations for the case of MoS_2 thin films showed no ripple formation under the same loading conditions.

Chapter 5 investigates the atomic scale mechanisms related to the emergence of Moiré patterns in CVD-grown MoS2 structures using MD simulations. Bilayer MoS_2 triangles are places over a substrate layer to mimic CVD-grown structure with realistic edge configurations. The MD simulations suggest that the strain subjected to the substrate is not able to completely transfer to the bilayered MoS_2 sample, and the difference in the layer strain causes lattice match, which results in the formation of Moiré patterns. The emergence of Moiré islands is correlated to the reduction in the layer strain.

Chapter 6 focuses on the effects of strain on electronic structure of other 2D materials: bilayer WSe_2 and HfS_2. The effect of vdW interaction and spin orbit coupling on the band structure of bilayer WSe_2 are studied. DFT results indicate that the vdW interaction, SOC and Poisson effects may significantly influence the band edge locations and the gap energies of band transitions. As for 2D HfS_2, distinct read shift under tensile strain and blue shift under compressive strain are observed, and the metallization of 2D HfS_2 occurs around 10% at the compressive domain.

CHAPTER TWO

2. EDGE EFFECTS ON ELECTRONIC STRUCTURE OF MoS_2 BILAYER

2.1 Introduction

As shown in chapter 1, there is a rapidly growing interest in investigating the band gap of 2D MoS_2 materials through strains and stresses to further exploit their potential for use in various electronic and optoelectronic applications [20, 90, 97-102]. An example setup of the strain device is shown in Figure 1.13. In these experiments [46, 90, 97, 101], the magnitude of the strain in the sample is estimated by the deflection of the substrate because the sample and the substrate are assumed to bear the same degree of mechanical deformation. While this assumption is generally true if an ultrathin film is clamped on the substrate by strong covalent bonds, it does not necessarily hold for a 2D sample that is weakly adhered to a substrate by long-range vdW interactions. The local strain in 2D materials can be mapped through aberration-corrected high-resolution transmission electron microscopy. This approach has recently been realized in single-crystal and bi-crystal graphene membranes [103], but, unfortunately, has not yet been applied to MoS_2 films under mechanical deformations.

Alternatively, theoretical simulations based on DFT are able to provide some insights into this problem. There has been a considerable effort to understand the variations in the electronic band structures of bilayer MoS_2 [90, 99, 102, 104, 105]. These studies are consistent with the experiments that E_g of bilayer MoS_2 is red shifted under a uniaxial strain. They are performed under the mechanical boundary condition (MBC) wherein the top and the bottom layers are of the equal size and are always subject to an identical amount of strain or stress.

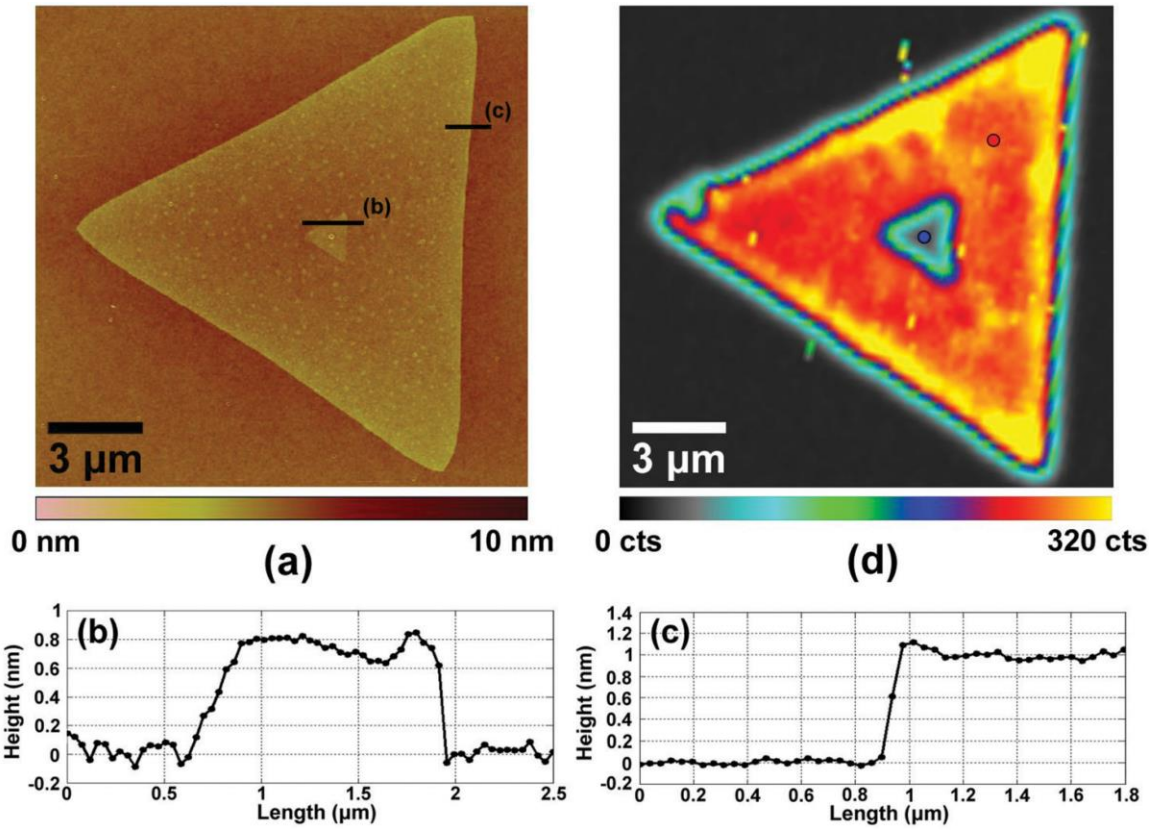

Figure 2.1 (a) AFM image of CVD-grown bilayer MoS_2. Step height measurement (b) from monolayer to bilayer, and (b) from SiO_2/Si substrate to monolayer. (d) PL intensity map of MoS_2 bilayer. Reproduced from Ref. [62].

However, the CVD-grown MoS_2 flakes comprise of a small top layer on top of a large base layer, as shown in Figure 2.1 (a) [62]. The response of such 2D bilayer structures

with unequal dimensions is likely to create an inequality in the amounts of strain in the two layers and hence inhomogeneous electronic properties, such as ununiform distribution of PL intensity as shown in Figure 2.1 (d) [62]. A recent Raman spectroscopy experiment demonstrates that relative sliding occurs between a 2D graphene film and the supporting SiO_2/Si substrate when the film is mechanically pulled from one side [106]. This finding implies that the degree of the strain in a 2D sample may be different from that in the substrate. Similarly, in a bilayer sample the top and the bottom layers can be subject to different magnitudes of strain as well. It is feasible that the top layer is more apt to relax the strain by atomic displacements as it is weakly bound to the substrate compared to bottom layer. Due to this complexity, the strain configuration of the bilayer MoS_2 samples in those experiments has to be identified to obtain a better understanding in the effect of strain on their electronic band structure. This chapter discusses DFT simulations aimed to investigate the effect of strain in bilayer MoS_2 films under a less constrained MBC that allows the top layer with an edge to relax under the presence of a uniaxial strain in the bottom layer.

2.1 Computational Details

The structure of an infinitely large bilayer MoS_2 sheet in the 2*H* stacking sequence is shown in Figure 2.2(a). This structure is characterized by the in-plane lattice parameters a_0 and b_0 ($b_0 = \sqrt{3}a_0$), the Mo-Mo interlayer distance l and the Mo-S bond length d_0 along the vertical [0001] direction [Figure 2.2(a)]. Such a unit cell is used to calculate the electronic properties of relaxed (i.e., unstrained) bilayer MoS_2, but any uniaxial mechanical deformation on this structure will generate identical strain states in the top and the bottom

layers. Therefore, a supercell is constructed based on the unit cell structure to enable different atomic and lattice relaxations between the two layers.

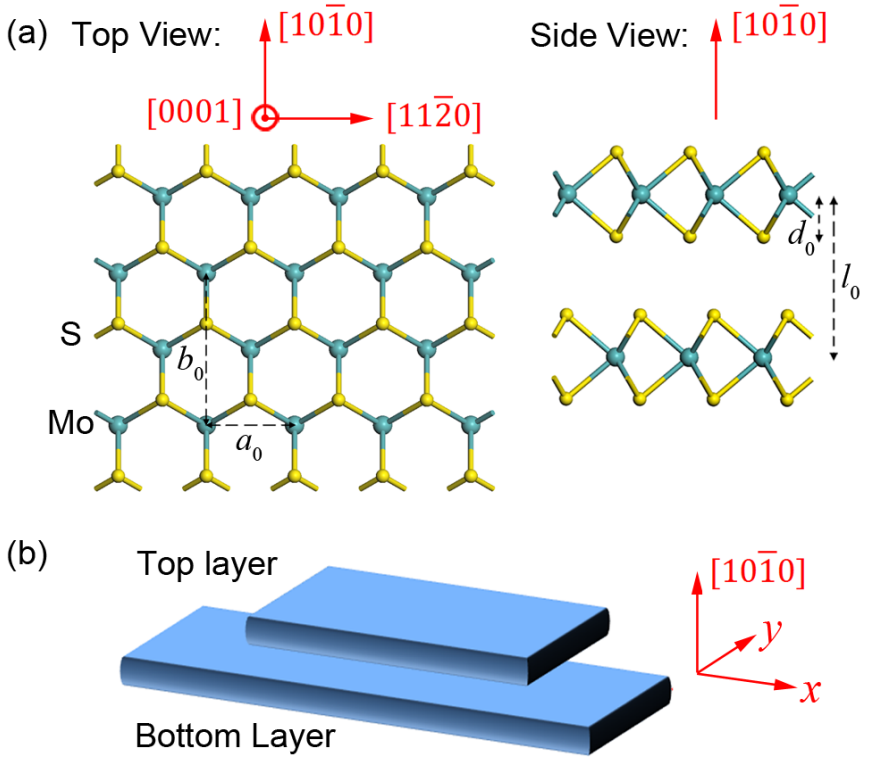

Figure 2.2 (a) Top view and side view of an infinitely large bilayer MoS_2 sheet, and (b) schematic show of the bilayer supercell used in this study.

As schematically shown in Figure 2.2(b), the supercell is rectangular in the basal (*xy*) plane. The top layer is of the same lattice size as the bottom layer along the *y* direction, but relatively smaller along the *x* direction. Three dimensional periodic boundary conditions are applied in the calculations so that the bottom MoS_2 layer is actually infinitely large while the top layer is composed of infinitely long nanoribbon arrays along the *y* direction. A vacuum space of 20 Å thick is used along the vertical [0001] direction of the supercell shown in Figure 2.2(b) to prevent unphysical interactions between adjacent images along this direction.

Two types of supercells with distinct nanoribbon growth orientations (and hence edge terminations) are considered in this study:

(1) $x//[11\bar{2}0]$ and $y//[\bar{1}100]$ with armchair edges along the y direction, and the bottom and the top layers are $14\times a_0$ and $8\times a_0$ wide along the x direction, respectively [Figure 2.3(a)];

(2) $x//[\bar{1}100]$ and $y//[11\bar{2}0]$ with zigzag edges along the y direction, and the bottom and the top layers are $13\times b_0$ and $9\times b_0$ wide along the x direction, respectively [Figure 2.3(b)].

Each supercell is investigated under two MBCs in the basal xy plane to simulate a bilayer MoS_2 film that is exfoliated onto a deflected substrate:

(1) uniaxial strain condition along the x direction with $\varepsilon_x\neq0$, $\varepsilon_y=0$, $\sigma_x\neq0$, and $\sigma_y\neq0$, where ε_x and ε_y (σ_x and σ_y) are the *average* strains (stresses) of the *entire supercell* along the x and y directions of Figure 2.2(b), respectively;

(2) uniaxial stress condition along the x direction with $\varepsilon_x\neq0$, $\varepsilon_y\neq0$, $\sigma_x\neq0$, and $\sigma_y=0$.

Under both MBCs, ε_x is taken as the parameter in the calculations and is varied from -6% to 6%.

The width of the top layer nanoribbon is ~2.5 nm and 4.9 nm in Figure 2.3 (a) and (b), respectively, much narrower than the experimentally fabricated bilayer MoS_2 nanoflakes or ultrathin films (~100 nm or wider). Such simulations, however, are beyond the capability of DFT calculations, even using modern high performance computational clusters. Therefore, the size of the crystal structure is compromised here. But the

nanoribbon of the top layer is wide enough to ensure that the dangling bonds of the edge atoms (R4 in Figure 2.3) will not affect the electronic band energy at the center of the supercells (R2 and R3 in Figure 2.3). In other words, the central part of such stripes can at least partially represent the inner part of an experimentally obtained bilayer MoS_2 nanoflake or ultrathin film. Also, the spacing between adjacent periodic images of the nanoribbons in the basal plane is large enough to prevent unphysical interactions between the images. To verify if the relatively narrow stripes used in this study can provide reliable and useful results that guide further experiments, I first increase the width of the top layer stripe in Figure 2.3(a) by 50%. The results of DFT calculations on the wider construct show no noticeable differences compared to the narrower ones and hence it is expected that the results scale up with the size of the bilayer structures. In principle, one can use molecular dynamics (MD) simulations to investigate strain effects in bilayer configurations that are

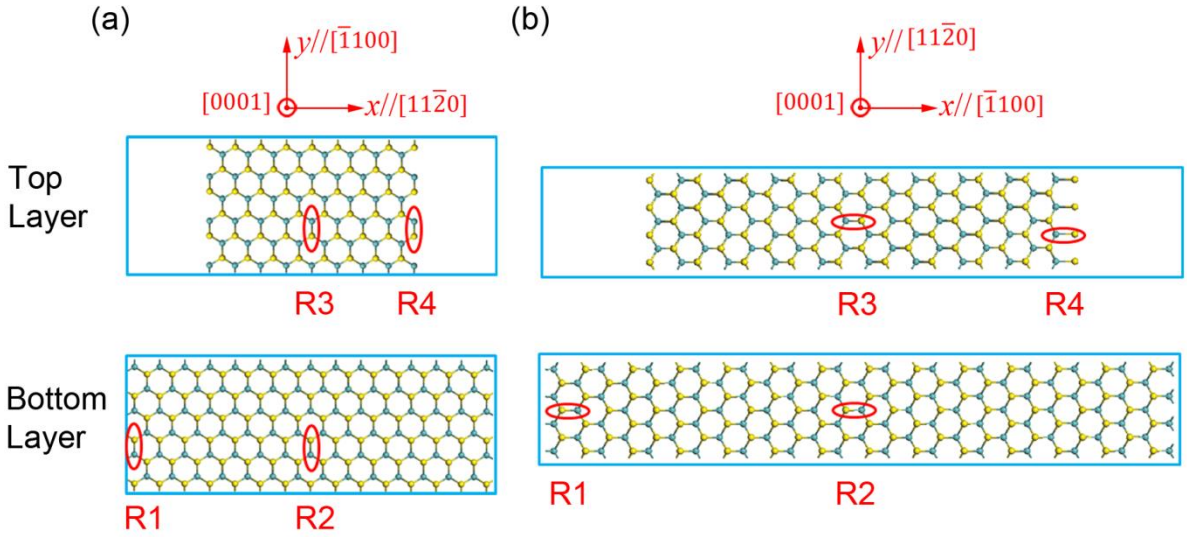

Figure 2.3 Top views of the pre-relaxed bilayer supercells with (a) armchair edges [Type (1)] and (b) zigzag edges [Type (2)] in the top layer. R1 is the region in the bottom layer with a monolayer situation, while R2 and R3 are regions analogous to bilayer MoS_2.

close to experimentally fabricated structures.

DFT calculations are carried out using projector augmented wave pseudo-potentials[107] as implemented in the VASP code [108]. A cutoff energy of 500 eV for the plane-wave expansions and a Monkhorst–Pack *k*-point mesh of 15×15×1 in the first Brillouin zone is found to yield well-converged results of the unit cell of the infinitely large bilayer MoS_2 sheet [Fig.1(a)]. The number of *k*-points are reduced to 1×9×1 and 1×15×1 for the supercell structures in Figs. 2(a) and (b), respectively. The atomic positions are optimized until all components of the forces on each atom are reduced to values below 0.01 eV/Å. The exchange-correlation functional is treated within the Perdew–Burke–Ernzerhof (PBE) generalized gradient approximations (GGA) [109].

To test the validity of this method, I first compute the lattice parameters (a_0, l_0, and d_0, see Figure 2.1 for details), the elastic stiffness tensor (C_{ij}), and bulk modulus (B_0) of bulk 2*H*-MoS_2 with space group $P6_3/mmc$. C_{ij} of this crystal structure has five independent components in the contracted notation, namely, C_{11}, C_{12}, C_{13}, C_{33}, and C_{44}, and B_0 are given by [110]

$$B_0 = \frac{(C_{11} + C_{12})C_{33} - C_{13}^2}{C_{11} + C_{12} + 2C_{33} - 4C_{13}} \tag{1.4}$$

The results of a_0, l_0, d_0, C_{ij}, and B_0 from pure PBE calculations and PBE with TS-vdW calculations are listed in Table 1.2, from which it is obvious that the usage of TS-vdW leads to a much better agreement with the experimental values [111, 112]. The values of a_0, l_0, and d_0 in an infinitely large bilayer MoS_2 sheet are reported in Table 2.1 as well.

Table 2.1: Lattice constants (a_0, l_0, and d_0, unit: Å), elastic stiffness coefficients (C_{11}, C_{12}, C_{13}, C_{33}, and C_{44}, unit: GPa), and bulk modulus (B_0, unit: GPa) of bulk 2*H*-MoS_2. Values in parentheses are results of bilayer 2*H*-MoS_2.

	a_0	l_0	d_0	C_{11}	C_{12}	C_{13}	C_{33}	C_{44}	B_0
This Work (PBE)	3.190	7.081	1.565	182.1	50.3	3.9	13.0	-1.6	12.3
This Work (PBE with TS-vdW)	3.158 (3.158)	6.056 (6.053)	1.560 (1.566)	218.8	51.3	5.4	47.3	14.1	37.7
Other DFT (PBE with TS-vdW)	3.160[a]	6.015[a]	1.564[a]						41[a]
Experiment	3.160[b]	6.147[b]	1.586[b]						53[c]

[a] Ref. [93], [b] Ref. [111], and [c] Ref. [112]

As a result, to correctly describe the structure and energy of the fewlayer TMDs, a supplemental TS-vdW interaction is needed to add to the conventional ground state energy to account for the interlayer coupling [113].

2.3 Edge Effects on Strained MoS_2 Bilayer Structure

The mechanical deformations and electronic properties of the two types of supercells are investigated in this section under the uniaxial loading conditions. I characterize the local microscopic deformations in the supercells with two parameters. The first parameter is the local uniaxial strain ε_x^L in the basal plane. It is defined as

$$\varepsilon_x^L = (a - a_0)/a_0 \,, \tag{2.2}$$

$$\varepsilon_x^L = (b - b_0)/b_0 \,, \tag{2.3}$$

in Types (1) and (2) supercells, respectively. Here a_0 and b_0 are the in-plane lattice parameters of infinitely large MoS_2 sheets (Figure 2.2), and a and b are the local in-plane atomic spacing in R1, R2, or R3. The second parameter is the relative change in the average Mo−S bond distance (ΔL) in the supercell defined as

$$\Delta L = (L - L_0)/L_0 \,, \tag{2.4}$$

where L_0 and L are the average local bond distances in the equilibrium unstrained and strained supercells, respectively.

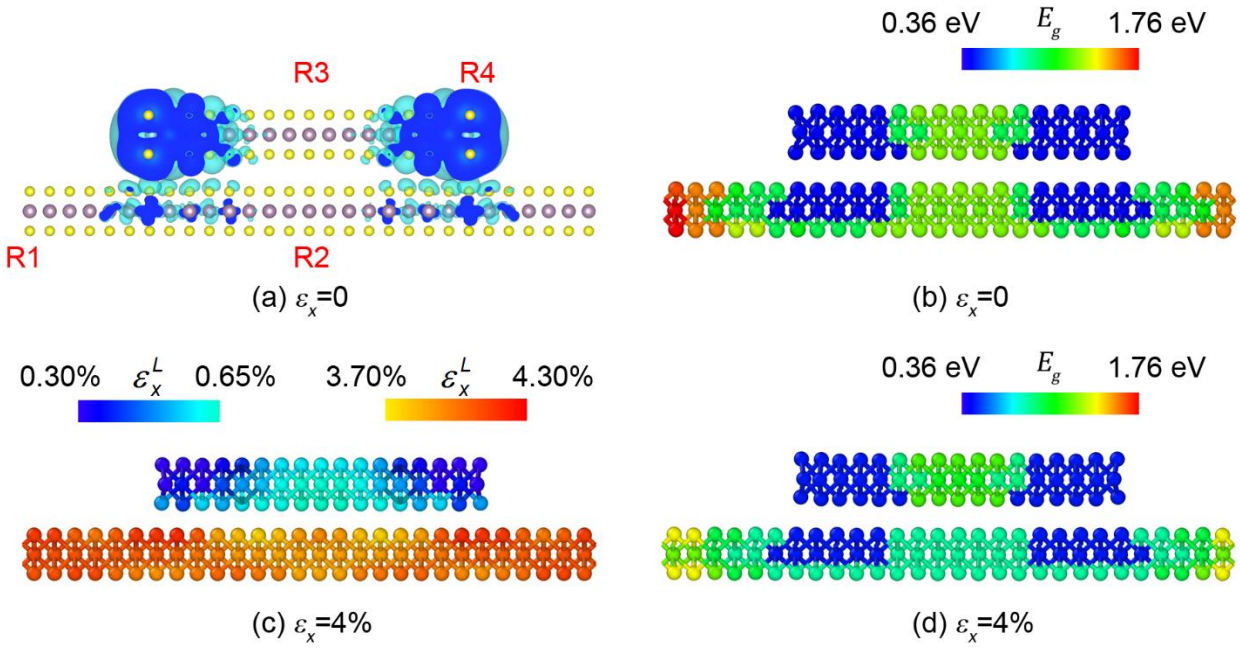

Figure 2.4 (a) Charge density of the dangling bonds of edge atoms in the top layer stripe, (b) local band gap energy (E_g) map, (c) local strain map under a uniaxial strain ε_x=4%, and (d) local E_g map of a Type (1) supercell under ε_x=4%.

The uniaxial strain condition, i.e. MBC (1), is first applied to the supercells. From Figure 2.4(c), the overall mechanical deformation in the bottom layer is much stronger in the bottom layer than in the top layer. As a result, the local band gap energy in the bottom layer [Figure 2.4(d)] is significantly decreased from the strain-free values [Figure 2.4(b)] whereas local E_g in the top layer stripe is little affected. ε_x^L, ΔL, and relative variation in local band gap energy (ΔE_g) at ε_x=2 % in R1, R2, and R3 are given in Table 2.2.

Table 2.2: Local uniaxial in-plane strain (ε_x^L), average variation in Mo−S bond lengths (ΔL), and relative changes in band gap energy (ΔE_g) in the strained supercells at ε_x=2 % under MBC (1).

Type of Supercell		R1	R2	R3
(1)	ε_x^L	2.083 %	1.640 %	0.161 %
	ΔL	0.298 %	0.264 %	0.061 %
	ΔE_g	−8.5 %	−13.6 %	−3.1 %
(2)	ε_x^L	2.410 %	1.638 %	0.520 %
	ΔL	0.341 %	0.226 %	0.058 %
	ΔE_g	−14.5 %	−13.5 %	−7.1 %

Here ΔE_g is taken as

$$\Delta E_g = (E_g - E_{g0}) / E_{g0}, \tag{2.5}$$

where E_{g0} is the strain-free local band gap energy in the supercells and are reported in Figure 2.5. From Table 2.2, there exists a positive correlation between the degree of lattice deformation (ε_x^L and ΔL) and ΔE_g. In both types of supercells, the central part of the top layer nanoribbon (R3) is much less deformed by the uniaxial strain than the bottom layer (R1 and R2). As a consequence, ΔE_g in R3 is much smaller than that in R1 or R2. It is noted that for a given ε_x and ε_x^L, ΔL, and ΔE_g are similar in Types (1) and (2) supercells

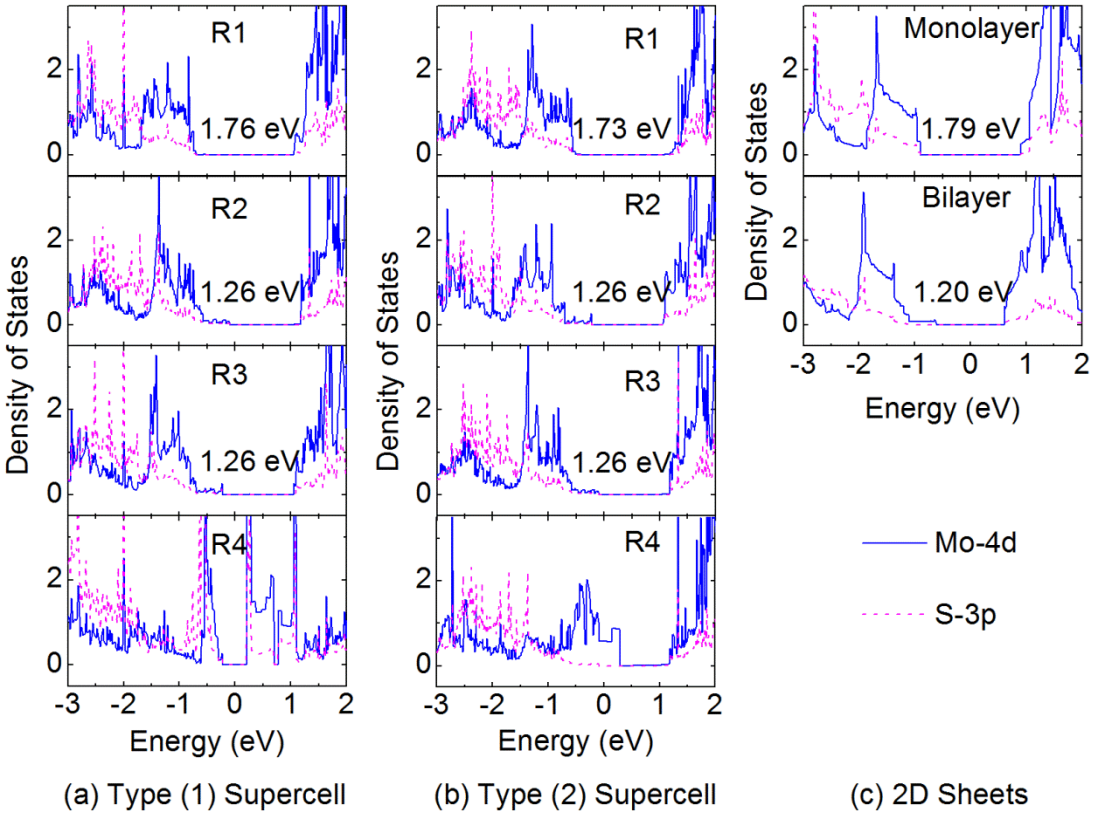

Figure 2.5 Density of states (DOS) in selected regions (R1, R2, R3, and R4) of (a) Type 1 supercell and (b) Type 2 supercell, and (c) DOS of infinitely large monolayer and bilayer MoS_2 sheets.

(see Table 2.2 as an example). Therefore, only the results of the Type (1) supercell will be presented in the rest of this section. Next, the supercells are studied under MBC (2), i.e., the uniaxial stress condition. In this case, the *y* direction of the supercells shown in Figure 2.3 is stress free (σ_y=0). This is achieved by introducing a commensurate strain ε_y to relax the supercell lattice along the *y* direction under the presence of ε_x. As an example, ε_y=−0.43 % for ε_x=2 % in Type (1) supercell. Note that ε_y is equally applied to the bottom and the top layers because these layers are of the same lattice size along the *y* direction [see Figure 2.3].

The results show that ΔL and ΔE_g in R1, R2, and R3 under MBC (2) are always smaller than the values under MBC (1) for a given ε_x. This can be seen by comparing the values in Tables 2.2 and 2.3. These reductions under MBC (2) are due to the additional atomic relaxations along the *y* direction. The overall band gap difference between R2 and R3 is 0.12 eV under MBC (2), the same as the value under MBC (1). This indicates that ε_y does not affect the relative band offset in the central regions of the bilayer structure (R2 and R3).

Table 2.3: ε_x^L, ΔL, and ΔE_g in the Type (1) supercell at ε_x=2 % under MBC (2).

	R1	R2	R3
ε_x^L	2.129 %	1.735 %	0.396 %
ΔL	0.238 %	0.217 %	0.031 %
ΔE_g	−6.9 %	−10.3 %	−0.7 %

Finally, the analysis on the strain effect is expanded to a broader range of the uniaxial strain in the supercell. ε_x^L and ΔL in R1 and R2, and R3 change monotonically as a function of ε_x for −6 %<ε_x<6 %. The local strain ε_x^L in R1 and R2 roughly equal ε_x, but ε_x^L in R3 is always smaller by an order of magnitude [Table 2.3]. For example, $\varepsilon_x^L = 0.57$ % for ε_x=4 %, and $\varepsilon_x^L = -0.25$ % for $\varepsilon_x = -4$ % (Table 2.3). Similarly, ΔL in R3 is much smaller as compared to that in R1 and R2 for a given ε_x. This indicates that the mismatch in lattice deformation between the top and the bottom layers increases with an increasing uniaxial strain that is applied on the bottom layer. This mismatch in the lattice deformation is attributed to the free edges of the top layer nanoribbon that enable more degrees of freedom to relax the strain.

The local band gap energies in R1, R2, and R3 are reported in Table 2.4 as a function of ε_x, from which one can see that the difference in E_g between R2 and R3 grows with an increasing ε_x in the tensile strain domain, but remains almost 0 eV in the compressive strain domain. E_g in R1 decreases monotonically as ε_x^L increases from 0 to 6 % in the tensile strain domain, but it increases first from $\varepsilon_x = 0$ to $\varepsilon_x^L = -2$ % and then drops for further in-plane compressions. This trend is analogous to that in infinitely large monolayer MoS_2 sheets under a uniaxial strain. The segmented variation trends of E_g originate from the shifting of VBM and CBM locations in the reciprocal space under different strain domains[99][114]. In monolayer MoS_2, VBM is shifted from the K point

for $\varepsilon_x^L < 1$ % to the Γ point for $\varepsilon_x^L \geq 1$ % and CBM is shifted from the Σ_{min} point (midpoint between K and Γ) for $\varepsilon_x^L \leq -1$ % to the K point for $\varepsilon_x^L > -1$ %.

Table 2.4: ε_x^L and ΔE_g in the Type (1) supercell for different ε_x values under MBC (1).

ε_x	R1		R2		R3	
	ε_x^L	E_g	ε_x^L	E_g	ε_x^L	E_g
−6 %	−5.94 %	1.75 eV	−5.90 %	1.34 eV	−0.10 %	1.34 eV
−4 %	−4.01%	1.81 eV	−3.90 %	1.32 eV	−0.25 %	1.32 eV
−2 %	−1.93 %	1.87 eV	−1.94 %	1.30 eV	−0.05 %	1.29 eV
0	0	1.76 eV	0	1.26 eV	0	1.26 eV
2 %	2.08 %	1.61 eV	1.84 %	1.09 eV	0.16 %	1.22 eV
4 %	4.11 %	1.41 eV	3.79 %	0.88 eV	0.57 %	1.19 eV
6 %	6.31 %	1.20 eV	5.76 %	0.73 eV	0.60 %	1.15 eV

To investigate if these results are affected by system size, additional DFT simulations are carried out for the unit cell in Figure 2.4 with a wider top layer stripe. It can be seen that the calculated local strain and band gap energies in the wider bilayer

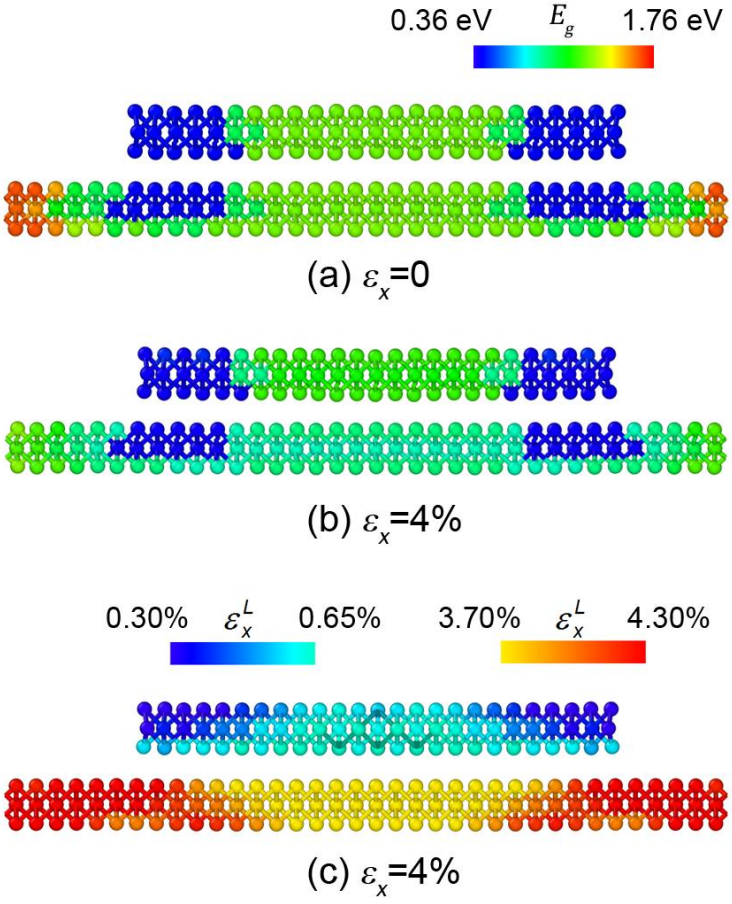

Figure 2.6 (a) Local band gap energy (Eg) map of the wider unconstrained Type (1) supercell. (b) local Eg map of the wider Type (1) supercell under a uniaxial strain ε_x=4%. (c) local strain map of the wider Type (1) supercell under ε_x=4%.

structure (Figure 2.6) are very close to the results in Figure 2.4. These results suggest that the trends are similar for bilayer structures with larger dimensions of the top layer in the MoS_2 bilayer structures. A more precise study to investigate strain effects in larger dimension structures will need molecular dynamics (MD) simulations to look into the

strain configuration of a bilayer MoS_2 that span dimensions ranging from several hundred nanometers to tens of microns in the top layer.

2.4 Conclusions

In summary, first principles DFT calculations are performed to study the effect of strain in 2D bilayer MoS_2 materials. The modeled bilayer structure is different from the conventional unit cell; it is composed of an infinitely large bottom layer and arrayed nanoribbons in the top layer. The edges of the nanoribbons allow the top layer to have more flexibility in terms of atomic relaxation compared to the bottom layer. As such, this model can be used to simulate a bilayer MoS_2 flake wherein the top layer is significantly smaller than the bottom one. The two layers are found to be subjected to different local strains under a tensile uniaxial strain/stress condition in the basal plane. The local strain ε_x^L, variation in the Mo−S bond length ΔL, and the variation in band gap energy ΔE_g at the center of the top layer are substantially smaller than those in the bottom layer under a tensile uniaxial strain/stress condition. The separation between the two band gap energies increases with an increasing uniaxial strain in the tensile strain domain. These results demonstrate that distinct band gap energies can be induced/achieved in the bilayer structures under tensile uniaxial strain. Such variations need to be accounted for when analyzing strain effects on electronic properties using experimental methods or in continuum models. These variations are likely to change with the dimensions and number of layers in multilayered structures. The possibilities to have distinct band gap energies under loading conditions of tensile strain for multilayered 2D structures show promise for

the use of strain engineering to generate inhomogeneous electronic properties for the design novel vertical transistors based on 2D stacked films.

The length scale of these novel phenomena is usually hundreds of nanometers or larger, which is beyond the capability of DFT studies. Therefore, a detailed investigation on these effects on is not included in this chapter. Molecular dynamics (MD) will provide more insights into strain effects in multiple layer MoS_2, which will be discussed in chapter 4 and 5.

CHAPTER THREE

3. ROLES OF DEFECTS ON ELECTRONIC AND MECHANICAL PROPERTIES OF BILAYER MoS_2

3.1 Introduction

The CVD grown MoS_2 sheets suggest the presence of intrinsic defects such as vacancies, interstitials and grain boundaries that are inevitable to form during the growth process [64]. It has been reported that these defects may be responsible for the reduced mobility in CVD-grown MoS_2 [115]. Therefore, A large number of theoretical [67, 116-128] and experimental [44, 65, 127, 129-133] efforts have been devoted to the fundamental understanding of the effects of defects on the modifications of the electronic, optical and transport properties. Ab initio calculations have demonstrated that the presence of defects in monolayer MoS_2 may introduce additional charge states at valence band maximum (VBM) or within the mid gap region [120, 124, 126, 128]. The mid gap states are observed by STM measurements at energies within the band gap, which confirms these charge states have either a triangular or circular shape in STM imaging [127]. These defect states activate new optical transitions and thus modify the optical and transport properties [122]. For example, due to the presence of point defects, the free electrons are drained from the materials via the charge states at defect sites, and the charged excitons are transitioned to neutral excitons. Such a transition is found to significantly enhance the overall PL intensity, especially at low temperature and in gas environments such as N_2 [65]. The presence of

defects alters the relative intensities of Raman peaks in monolayer MoS_2 [134] and also provide opportunities through doping to introduce long-range ferromagnetic ordering [135] and exhibit a Curie temperature in greater than room temperature [136]. Such modifications in the electrical, optical, vibrational, magnetic, and chemical properties of the materials opens up the possibility of "defect engineering" [43] to tailor the properties for desired applications. For example, it is possible to create multi-bandgap semiconductors by introduce point defects in the pristine 2D structures to obtain a broad spectrum response in the electronic devices [65]. However, in some cases the performance of the devices may be downgraded at the presence of defects because the activated charge states are likely to cause Fermi-level pinning [121]. As a result, defect engineering of 2D materials requires a

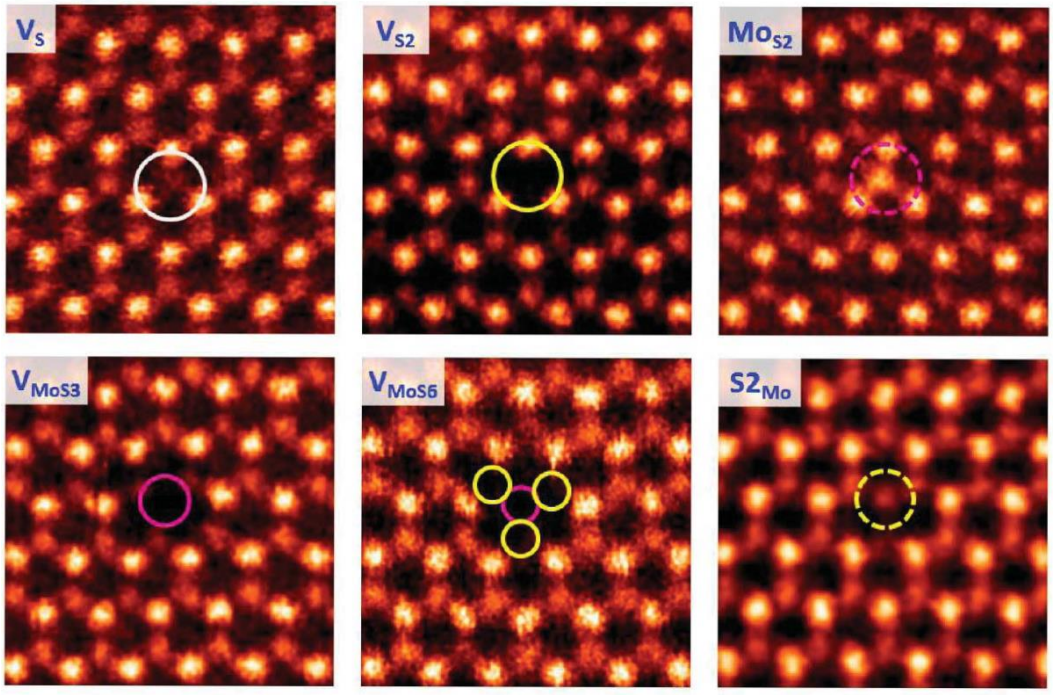

Figure 3.1 Atomic resolution ADF image of intrinsic defects found in CVD-grown monolayer MoS_2. Reproduced from Ref. [64].

fundamental understanding of the role of defects on the modifications in the local electronic structure.

However, the current understanding of the role of defects is largely limited to single layer MoS_2, while the effects of defects on bilayer MoS_2 remain unknown. It is unclear whether the modifications in electronic properties in the layer containing a defect are local or are also transferred to its adjacent perfect layer. As a result, it is important to understand the modification in electronic properties as well as the mechanical behavior of few-layered MoS2 structures due to the presence of defects in CVD-grown structures. The electronic structure is investigated by investigating the charge states that are generated in the atoms surrounding the vacancies and the mechanical behavior is studied by investigating the energy barriers for sliding in bilayer MoS_2 structures.

3.2 Simulation Details and Structural Relaxation

DFT calculations are carried out using projector augmented wave pseudo-potentials [137] as implemented in the VASP code [138]. The relatively large cutoff energy (600 eV) for the plane-wave expansions is selected to accurately determine the sliding energy barrier. The Monkhorst–Pack *k*-point mesh is 3×3×1 for relaxation and 5×5×1 for density of states (DOS) calculations. The exchange-correlation functional is treated within the Perdew–Burke–Ernzerhof (PBE) generalized gradient approximations (GGA) [139]. The conventional DFT energy is supplemented with a pairwise interatomic vdW potential which is determined by Tkatchenko and Scheffler (TS-vdW) from non-empirical mean-field electronic structure calculations [113]. The atomic positions are optimized until all components of the forces on each atom are reduced to values below 0.02 eV/Å.

Five types of vacancy-doped structures observed in CVD-grown few-layered MoS_2 [64] are investigated in this study: (a) single sulfur vacancy (V_S), (b) double sulfur vacancy (V_{SS}), (c) single molybdenum vacancy (V_{Mo}), (d) complex vacancy of one Mo and three surrounding sulfur atoms in one plane (V_{MoS3}), and (e) complex vacancy of one Mo and six surrounding sulfur atoms (V_{MoS6}). In addition, the defect-free pristine MoS_2 bilayer is also investigated to identify the modification in the electronic structures due to the presence of defects. An orthogonal unit cell comprised of 12 atoms with a lattice dimension of 3.17 Å × 5.46 Å is used for pristine bilayer MoS_2. For defect structures, a 3 × 3 supercell is adopted to lower vacancy concentration and avoid interaction between vacancy images in

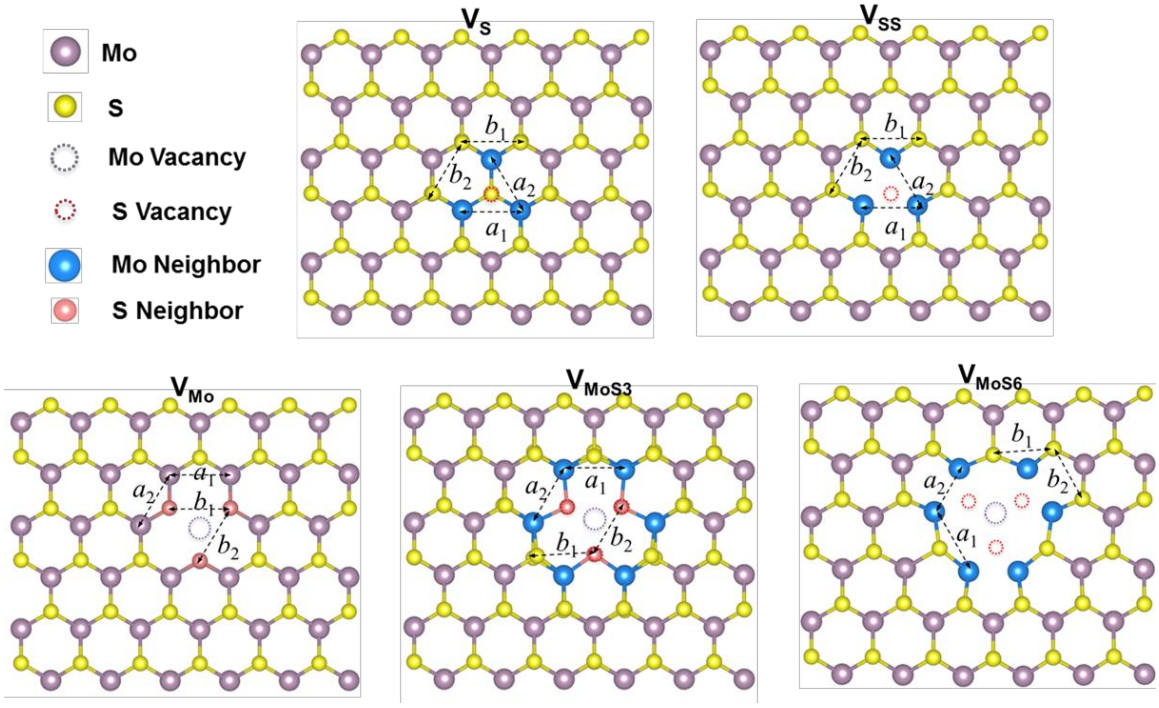

Figure 3.2 Top view of the relaxed structure of five-types of vacancy-doped MoS_2 bilayer: V_S, V_{SS}, V_{Mo}, V_{MoS3} and V_{MoS6}. The defect sites are indicated by dashed circles, and the direct neighbors of vacancies are denoted in different colors.

neighboring supercells. The vacancies are created at the center of the bottom layer by removing the corresponding atom(s) in the vacancy site(s). The top view of defect structures is displayed in Figure 3.2, in which the regular and defect sites are indicated by solid ball and dashed circle, respectively.

The relaxed MoS_2 bilayer structures with five types of defect configurations are shown in Figure 3.2. It should be noted that only the bottom layer containing the defect is shown here. The vacancy sites are indicated by dashed circles, and the direct neighbors to the vacancy atoms (i.e. with dangling bonds) are descripted in different color: blue for Mo neighbor, pink for S neighbor. The in-plane alignment of atoms suggest that the doping of vacancies leads to inward displacement of the direct neighbors to defect sites, which is also observed in defect structures of monolayer MoS_2 [123]. Such a displacement results in the modification/perturbation of bond lengths as compared to that in a pristine bilayer. Table 3.1 lists the binding energies for each type of defect as well as the bond length variations of the defect structures. The binding energies are calculated by

$$E_b = \frac{1}{n_{Mo} + n_S}\left(E_{def} + n_{Mo}\mu_{Mo} + n_S\mu_S - E_{prist}\right)$$

where n_{Mo} (n_S) is the number of Mo (S) vacancies, μ_{Mo} (μ_S) is the energy of one Mo (S) atom, E_{def} is the energy of defect structure, and E_{prist} is the energy of pristine structure. The chemical potential is assumed as the energy of an isolated atom.

Table 3.1. Binding energies and structural relaxation of five types of vacancy-doped MoS_2 bilayer. N_d is the number of direct neighbors to the defect sites. N_b is number of vacancy-affected bonds. R_{min}, R_{max}, R_{mean}, and σ is the minimum, maximum average and standard deviation of the vacancy-affected Mo-S bond length, respectively. a_1 and a_2 are vacancy-affected Mo-Mo bond length; b_1, and b_2 are vacancy-affected S-S bond length. The formation energies have units of eV and the bond lengths have units of Å.

	E_b	N_d	N_b	d_{min}^{Mo-S}	d_{max}^{Mo-S}	d_{mean}^{Mo-S}	σ	a_1	a_2	b_1	b_2
Pristine	N/A	N/A	N/A	2.40	2.40	2.40	0	3.16	3.16	3.16	3.16
V_S	5.91	3	15	2.37	2.39	2.38	0.008	3.06	3.06	3.07	3.07
V_{SS}	5.89	3	12	2.38	2.39	2.38	0.003	2.84	2.85	3.01	3.07
V_{Mo}	14.18	6	12	2.36	2.37	2.36	0.005	3.21	3.07	3.23	3.22
V_{MoS3}	6.73	9	28	2.26	2.39	2.36	0.051	3.19	3.21	3.23	2.86
V_{MoS6}	6.37	6	24	2.33	2.46	2.38	0.053	3.57	2.59	3.16	3.02

As shown in Table 1, di-sulfur vacancy has the lowest binding energy among all the investigated types, while single Mo vacancy requires largest energy to form. N_d is defined as the number of direct neighbors. N_b is the number of vacancy-affected Mo-S bonds (i.e. bonds with direct neighbors). Here, d_{min}^{Mo-S}, d_{max}^{Mo-S}, d_{mean}^{Mo-S}, and σ are the minimum, maximum average and standard deviation of the vacancy-affected Mo-S bond length, respectively. The vacancy-affected Mo-Mo bond lengths are defined by a_1 and a_2,

while b_1, and b_2 are vacancy-affected S-S bond lengths. For all the five defect structures, the Mo-S bond lengths (d_{mean}^{Mo-S}) reduce by 0.02 Å ~ 0.04 Å as compared to pristine structure (2.40 Å). The complex vacancies (V_{MoS3} and V_{MoS6}) exhibit larger fluctuations in Mo-S bonds due to the larger number of defect sites. The in-plane Mo-Mo and S-S bonds show more pronounced variation (up to 18%). These changes in bond lengths are likely to result in modifications in electronic properties. The role of these modifications in the bonding environment of defect sites is discussed below.

3.3 Electronic Properties Defect MoS_2 Bilayer

The modifications in the electronic properties due to point defects are investigated using the density of states (DOS) of atoms in defect structures in comparison to those in pristine MoS_2 bilayer. The energies are referred to the fermi levels of the system, i.e. 0 eV corresponds to the Fermi level of the investigated structure. As shown in Figure 3.3, additional charge states (labeled 1-4) are activated in defect structures in the band gap region or near the band edges for bilayer structures with V_S, V_{SS}, V_{Mo}, V_{MoS3}, and V_{MoS6} defects. The energies of these states are displayed in Figure 3.4. The conduction band

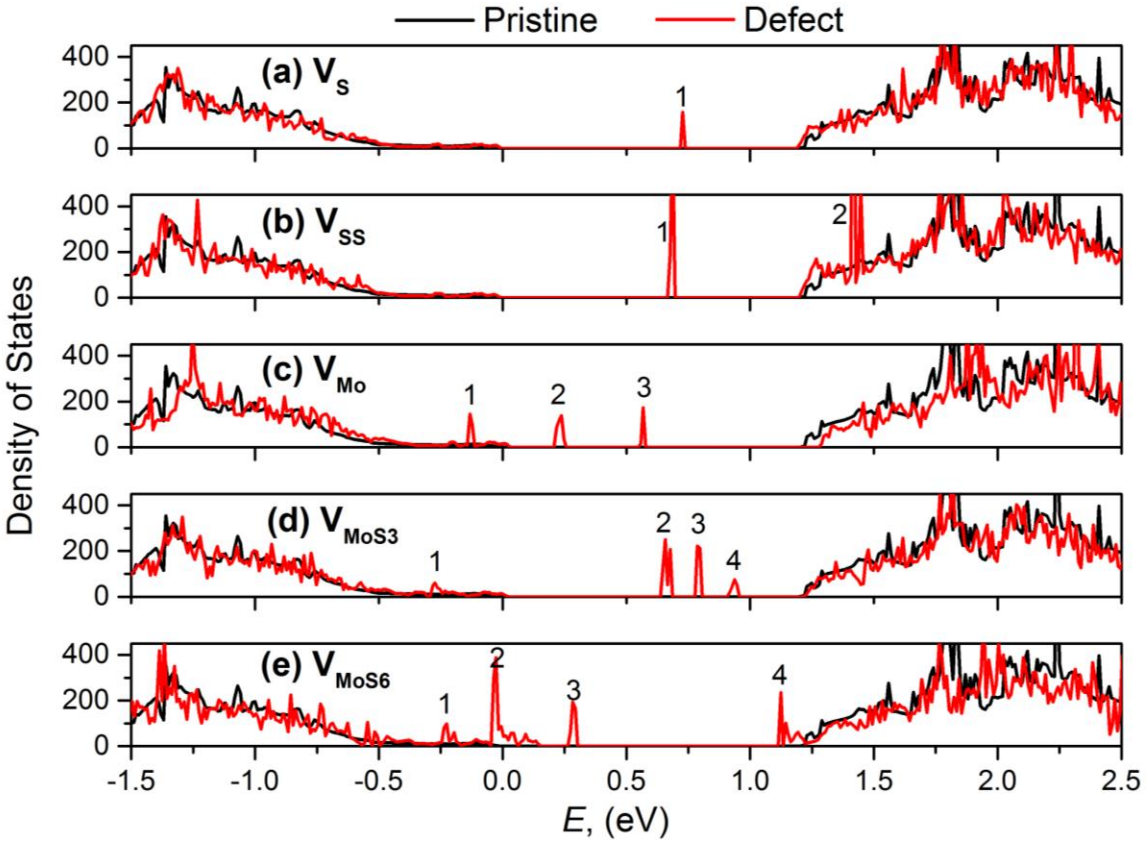

Figure 3.3 Comparison of total density of states between pristine and defect structures: (a) V_S, (b) V_{SS}, (c) V_{Mo}, (d) V_{MoS3} and (e) V_{MoS6}. The defect charge states are labeled by numbers.

minimum (CBM) and valance band maximum are indicated by dash lines to show the band edges. A charge state at 0.73 eV is observed for V_S, while multiple states are activated for other types. It is clearly shown that most of the defect charge states locate within the gap region, which could be employed to develop multi-bandgap semiconductors for wide-spectrum devices.

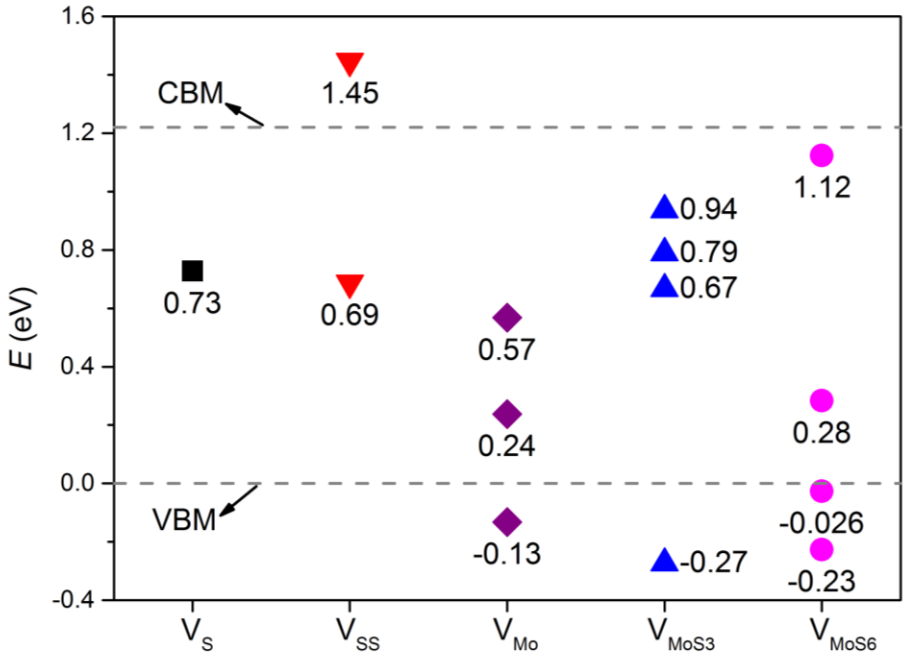

Figure 3.4 The energies of defects charge states for various types of vacancies. The band edges of pristine structure are indicated by dashed line.

In addition, partial density of states for atoms near the vacancy sites are investigated to study the variations in orbital contributions due to the defects. The on-site projected DOS from major contributed atomic orbitals (*d* orbitals for Mo atoms and *p* orbitals for S atoms) are included. Four representative atoms are selected to determine the effects of vacancies: Mo and S in bottom layer adjacent to the vacancy site(s) (denoted as Mo1, and S1, respectively), Mo and S in top layer atop the vacancy site(s) (denoted as Mo2 and S2, respectively). The pDOS of these four atoms in V_S-doped bilayer in comparison with the

pristine bilayer system are shown in Figure 3.5. As indicated by the total pDOS of pristine bilayer MoS_2 (dashed orange line), the band gap energy of clear bilayer MoS_2 is 1.2 eV, which is consistent with the previous studies [54, 140].. Similar to sulfur deficient monolayer MoS_2 [118, 121, 128], two distinct defect states are clearly observed in pDOS of V_S-doped bilayer (solid line) as compared to those of pristine structure (dashed line). The first state is located below the valence band edge (around -0.6 eV), and another is close to the conduction band maximum (CBM), around 0.73 eV. The pDOS of all the four atoms, either in top or bottom layer, are affected by the presence of the vacancy. The bottom layer, where vacancy situates, is observed to be modified to a larger extent, which can be implied from the much more significant peaks in pDOS of the atoms (Mo_1 and S_1) in the bottom layer. On the other hand, the contributing orbitals for the two defect states are noticeably different. For the first state, the major contributing orbitals are $d_{xz} + d_{yz}$ for Mo1 atom, d_{z^2} for Mo2 atom, and p_z for S1 and S2 atom. The second states are mainly contributed from $d_{x^2} + d_{xy}$ for Mo atoms and p_{x+y} for S atoms. As a result, the in-plane orbitals dominate in the second defect state for all the four atoms, which suggests that this state may be related to the structural reconstruction within the plane.

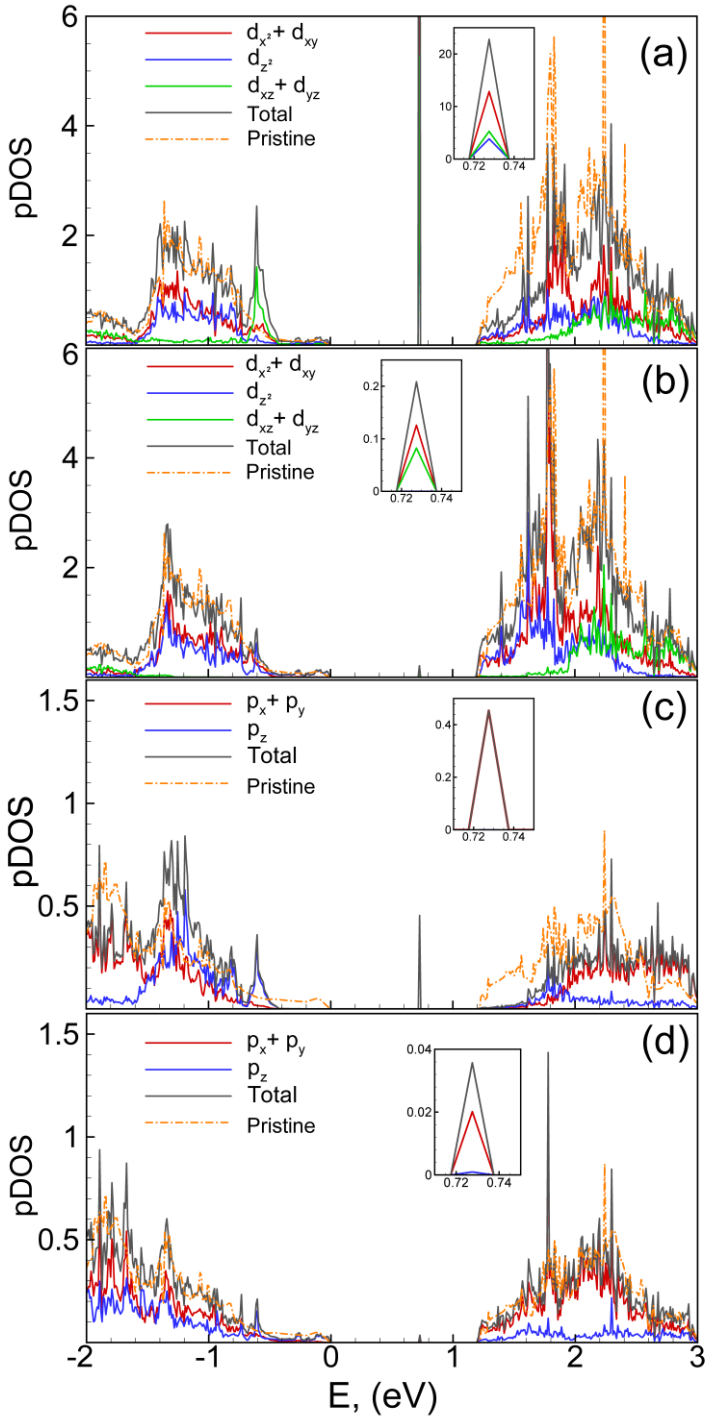

Figure 3.5 Partial density of states of different atoms in VS-doped MoS2 bilayer: (a) Mo1, (b) Mo2, (c) S1, (d) S2. Inserted plots illustrate the orbital contributions of the defect states.

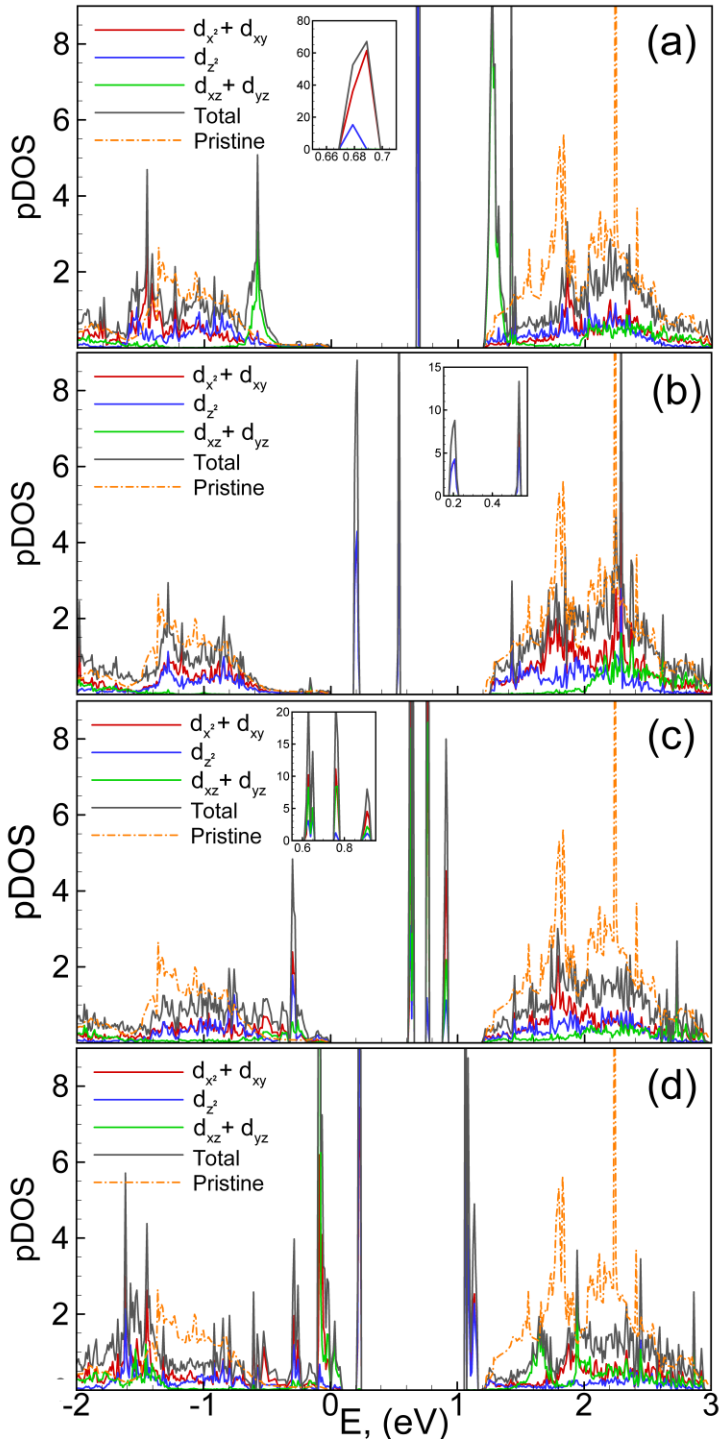

Figure 3.6 Partial density of states of Mo1 atom for different types of defect MoS2 bilayer: (a) V_{SS}, (b) V_{Mo}, (c) V_{MoS3}, (d) V_{MoS6}. Inserted plots illustrate the orbital contributions of the defect states.

The effects of different types of vacancies on modification of pDOS are presented in Figure 3.6. Because Mo and S atoms show similar charge state for the same defect type, only the pDOS of Mo1 atoms are shown here. It is found that more defect charge states appear with the increasing number of vacancies. For di-sulfur deficient structure (Figure 3.6(a)), additional defect state arises at the conduction band edge, which is mainly contributed by $d_{xz} + d_{yz}$ orbitals. In V_{Mo}-doped structure (Figure 3.6(b)), three defect charge states are observed: two distinct states at 0.2 eV and 0.54 eV in the mid gap region, and a shallow state at -0.83 eV below the VBM. In two complex types of vacancy V_{MoS3} and V_{MoS6}, the pDOS are considerably changed. The V_{MoS3} (Figure 3.6(c)) causes four sharp charge states, three in the mid gap region, one below the VBM. In V_{MoS6}-doped structure (Figure 3.6(d)), six distinct defect states are observed.

The nature of the defect charge states can be further investigated by the partial charge density within the energy range of the corresponding states. For example, the charge density within the energy range of the second defect charge state (0.73 eV) of V_S-doped structure is presented in Figure 3.7(a). Only atoms in the bottom layer are shown because the charge density for atoms in the top layer is negligible under the selected isosurface

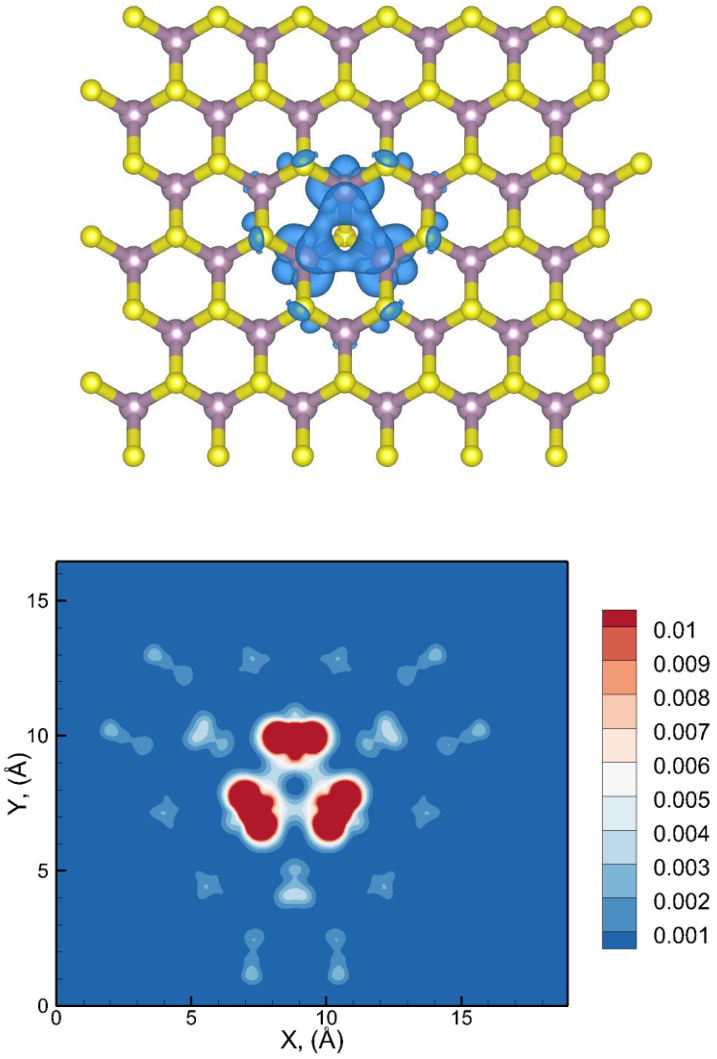

Figure 3.7 : Charge density of the defective states around 0.73 eV in the mid gap region (peak 1) for the bottom layer for vacancy type of V_S. and projected charge density along Mo plane of the defect states around 0.73 eV.

(0.003 e/Bohr^3). It is clearly shown that the defect state preserves the trigonal symmetry in V_S-doped structure, and has a triangular shape, which is frequently observed in the atomic resolution STM images of native point defects in MoS_2 single layer [127]. The defect state is mainly contributed by Mo1 atom with a hybridized orbital shape of d_{x^2}, d_{xz} and d_{z^2}, which is consistent with the observations in the pDOS plot (Figure 3.5(a)). The d_{xz} orbitals of three Mo1 atoms overlap with each other and form a bonding with a triangle shape. The S1 atom has a slightly distorted p_z symmetry. The projected charge density on Mo plane of the bottom layer is presented in Figure 3.7(b), from which, one can conclude that the defect state is rapidly diminished in the atoms far away from the vacancy site. The charge density and the projected charge density along Mo plane in the bottom layer for the other four vacancy types around various energy levels are presented in Figure 3.8. For all the four types of vacancies considered in this study, the activated charge states are limited in

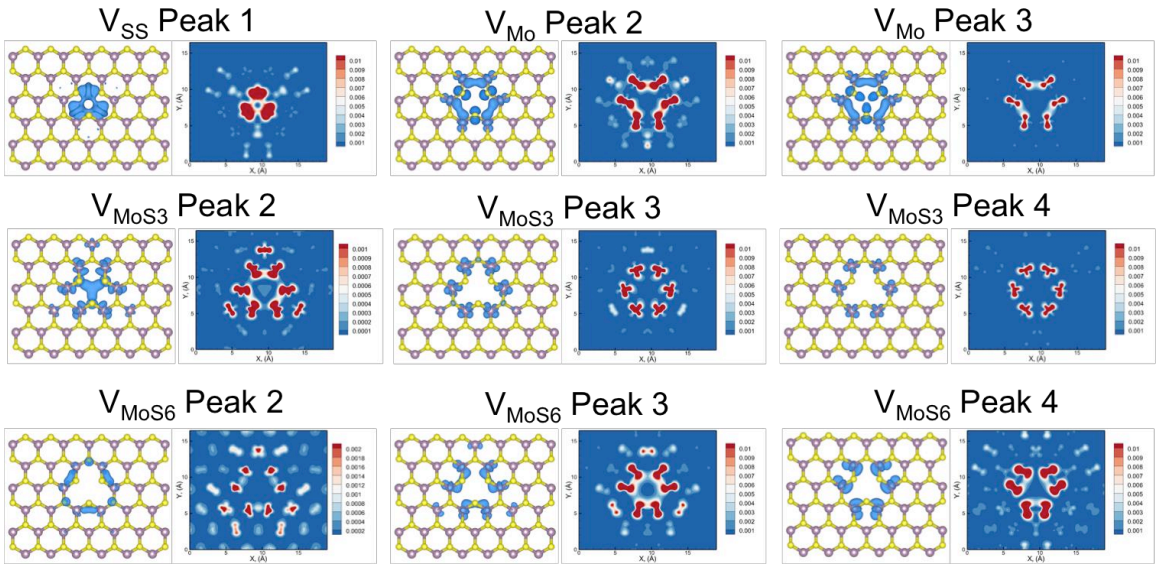

Figure 3.8 Charge density of the defective states and projected charge density along Mo plane of the defect states in the mid gap region for the bottom layer for other four types of vacancies. The peaks are numbered the same as **Figure 3.3**.

the atoms near the vacancies. Therefore, the effects of defects are anticipated to be confined within the local regions. The modifications of electronic properties due to the presence of defects are, hence, localized around atoms adjacent to the vacancies.

3.4 Strain Response of Vacancy-doped MoS_2 Bilayer

These defects also determine the strain response of bilayer MoS_2 system. The band gap energy of the multilayer MoS_2 terrace structure are observed to shift at a random layer [141]. The shift is speculated to be attributed to the sliding of the layers, which are caused by the relatively lower energy barrier for sliding in regions with defects [141]. As a result, the effect of presence of defects on the energy barriers for sliding are investigated using DFT simulations. The energy barriers for a pristine bilayer MoS_2 structure can be obtained along zigzag sliding pathway through AA'-AB'-AA', which is demonstrated to be most energetically favorable for bilayer MoS_2 [141-144]. It starts from AA' stacking, noted by sliding coordinate = 0 (SC=0). AA' stacking is the normal 2*H* phase (Figure 3.9 (a)), in which the S atoms in the bottom layer are eclipsed by the Mo atoms in the top layer. The optimized route is along zigzag direction as indicated by the black arrow. Four intermediate stacking sequences (SC = 1, 2, 3, 4) are selected to obtain the energy profiles along zigzag pathway AA' - AB'. In AB' stacking (SC=5), S atoms in the top layer are situated at the hexagonal hollow site, and Mo atoms in the top layer are over Mo atoms in the bottom layer. The sliding direction rotates 120^0 and shifts back from AB' (SC=5) to AA' (SC=10). Again, four intermediate sequences are added (SC = 6, 7, 8, 9). The entire sliding route is indicated by the red arrow in the top view of left panel of Figure 3.9(a).

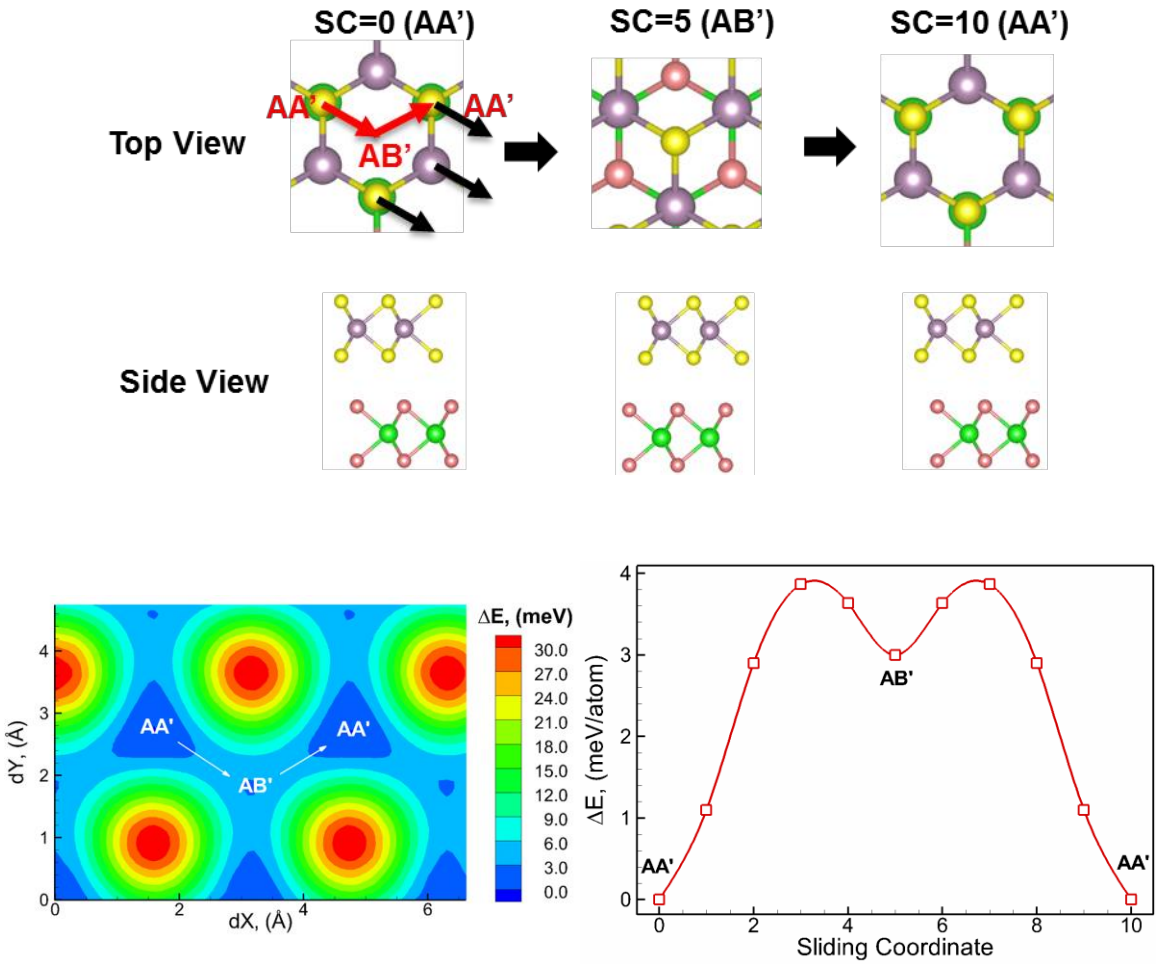

Figure 3.9 Top view and side view of AA' and AB' stacking as well as the sliding pathway. PES is shown in the left and energy profile of pristine MoS_2 bilayer along zigzag sliding pathway is shown in right.

The potential energy surface (PES) for interlayer sliding are calculated to study the sliding behavior of bilayer MoS_2. The energy of AA' stacking (SC=0) is considered as the reference energy. The inclusion of vacancies lowers the energy barrier for all the stack sequences and has no effect on the shape of the energy profile. The energy barrier for sliding increases at first and reaches to the maximum approximately at SC=3, i.e. 3/5 along AA'-AB'. The energy barrier declines to metastable state at AB' stacking. For pristine

bilayer, the highest energy barrier along the zigzag route, ΔE_{max}^{P}= 3.91 meV. The PES of pristine bilayer is also shown in Figure 3.9 (a). The PES is constructed by relatively displacing the bottom layer in X and Y coordinate while keeping the top layer fixed. Again, the energy of AA' stacking (dX=0, dY=0) is chosen as the reference. A 6 ×10 grid in X-Y plane is used for the displacement of the orthogonal unit cell of 3.158 Å × 5.41 Å. A contour plot of energy surface with a 0.1 Å resolution is interpolated from the energies of the 60 grid points. Then the contour plot is repeated in X direction to obtain an explicit view of completed AA'-AB'-AA' sliding route, which is indicated by the white arrows. It confirms that the zigzag sliding route is the least energetically corrugated. AA' stacking is the most favored structure while AB' is metastable. To investigate the effects of these defects on sliding stability, the energy profiles of defect structures are compared with that of pristine structure.

The PES of various types of vacancies are plotted in Figure 3.10 (a)-(f) to identify the changes in the optical pathway and energy barriers as compared to pristine structure (Figure 3.10 (a)). Here the PES plots are focused specifically along the AA'-AB' route. As seen in Figure 3.10 (a), the energy in other directions are much higher (red) as compared to the zigzag route. Along the zigzag pathway, the highest energy locates at the narrowest point (noted as *N*) of the channel connecting AA' and AB'. As for the defect structures in Figure 3.10 (a)-(f), the PES of defects structure indicates the zigzag sliding pathway retain as the minimum energetical corrugation path. Although the inclusion of vacancies does not change the nature of the sliding behavior, the highest energy barrier

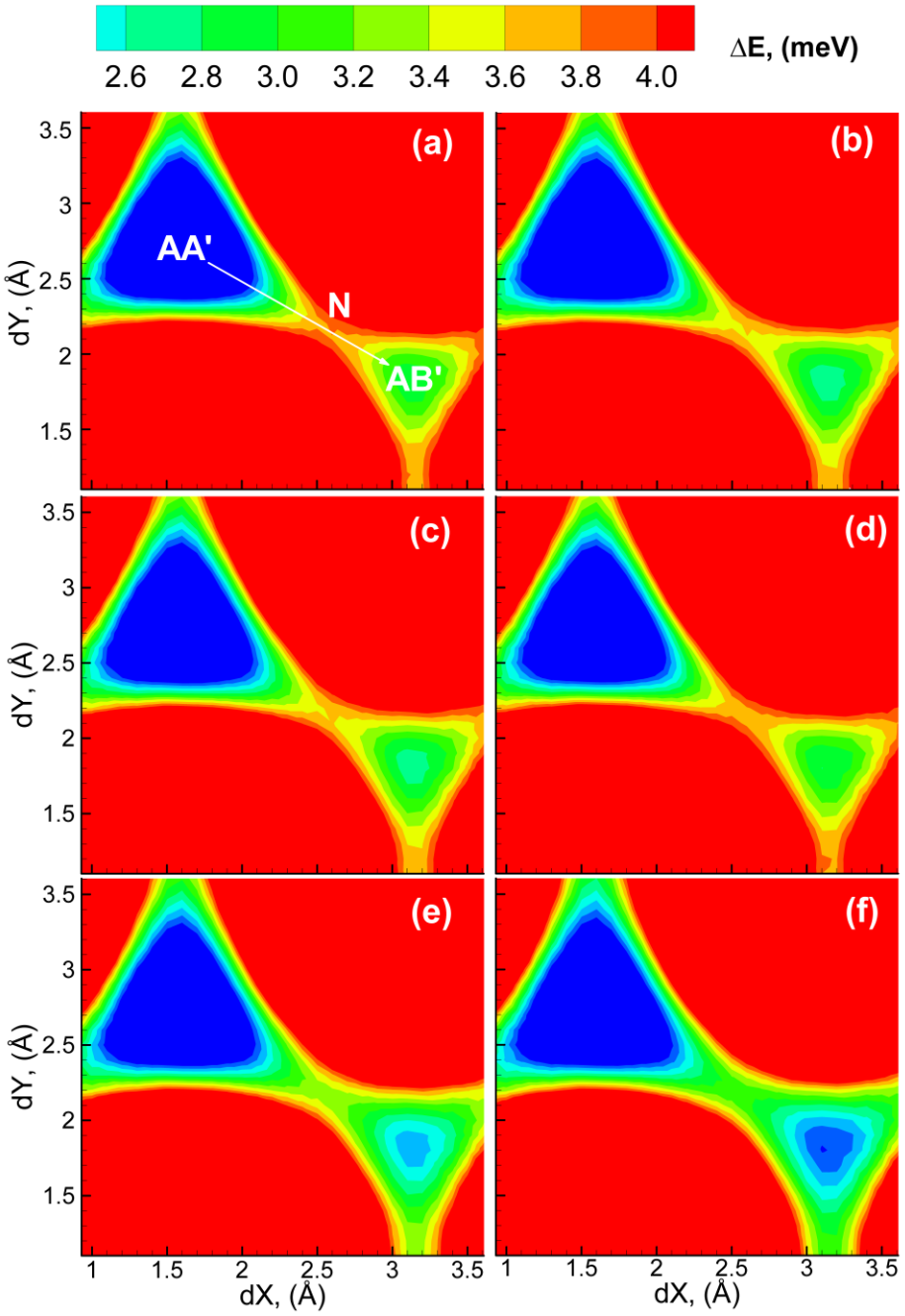

Figure 3.10 PES plot along the zigzag pathway of (a) pristine and five-types of vacancy-doped MoS_2 bilayer (b) V_S, (c) V_{SS}, (d) V_{Mo}, (e) V_{MoS3} and (f) V_{MoS6} depicts the variations in the energy barriers in defect structures.

ΔE_{max}, is significantly reduced in the defect structures. From the variations in the color of the channel, one can evidently conclude that the chance for slipping (from low to high) is pristine, V_{Mo}, V_S, V_{SS}, V_{MoS3}, V_{MoS6}. The energy profiles along zigzag pathway for various vacancy types are compared with that of pristine bilayer MoS_2 structure in Figure 3.11.

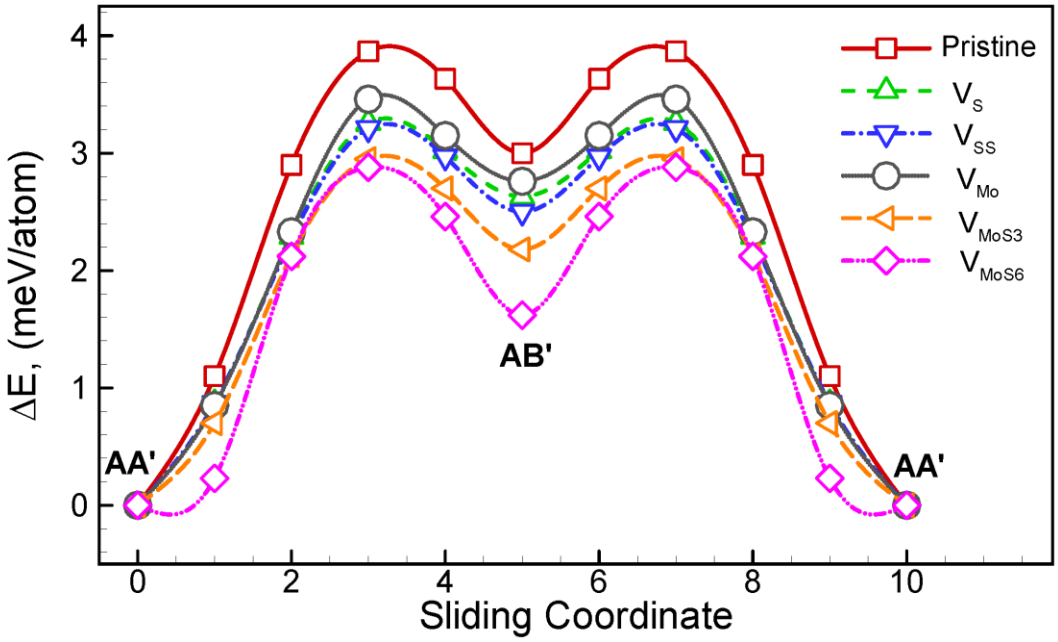

Figure 3.11 Energy profile of pristine and five-types of vacancy-doped MoS_2 bilayer along zigzag sliding pathway.

Similar to the previous study on sulfur vacancies [141], a reduction for energy barrier is observed for all types of defects. V_{Mo} defect causes less decrease as compared to V_S type, which is expected as the S-S interlayer vdW interaction prevails over Mo-Mo or Mo-S interlayer coupling. The energy barrier in V_{SS} type is slightly lower as compared to V_S, which indicates another S vacancy in the same layer do not play a significant role in reducing the energy barrier. The complex vacancy of V_{MoS3} and V_{MoS6} substantially weaken the interlayer coupling, thus decrease the energy barrier to 2.98 meV and 2.88 meV,

respectively. Such considerable reductions in energy barrier are anticipated to enhance the possibility of slipping in regions with defects of complex vacancies.

3.5 Conclusions

DFT calculations are performed to investigate the modifications in electronic properties and sliding behavior of MoS_2 bilayer at the presence of vacancies. Five types of vacancies including V_S, V_{SS}, V_{Mo}, V_{MoS3} and V_{MoS6} are studied and compared to pristine structure. Localized charge states are activated due to the presence of vacancies both within the band gap region and near the band edges. The number of defect charge states increase with the number of vacancies. The defects embodied in the bottom layer are found to affect the local density of states of atoms in both top and bottom layer. However, the modifications in electronic properties are limited to the atoms surrounding the vacancies. Therefore, the effects of vacancies are anticipated to be regional.

Moreover, the potential energy surfaces for various types of vacancy are studied and compared with that of pristine bilayer to identify changes in the most favored sliding pathway due to the presence of defects. It has been found that the optimal sliding route, zigzag route, is not affected by the defects. However, the presence of vacancies is likely to increase the chance for sliding because of the lowered energy barriers. As a result, the interlayer coupling is considerably reduced in defect structures.

CHAPTER FOUR

4. ORIGINS OF RIPPLES IN STRAINED CVD-GROWN MoS_2 MULTILAYER

4.1 Introduction

The optimization of the applicability of 2D MoS_2 as a building block in future electronic devices hinges on a fundamental understanding of the stability and variations in the microstructure of 2D MoS_2 structures as a function of strain, i.e. the strain response. The strain response of such CVD-grown MoS_2 structures is determined by the presence of edges and also results in slippage between the layers [63]. The CVD-grown structures result in terrace regions with varying number of layers that terminate as edges on top of the layer below it (Figure 4.1). The presence of these edges is likely to affect the strain-induced electronic and mechanical response of 2D MoS_2 structures observed for the case of mechanically exfoliated flakes that do not include such edges. The strain response of these structures suggests a hysteretic shift of the in-plane Raman peak position and PL energy at a large applied strain (Figure 1.15) [63]. It has been shown in chapter 3 that such a shift may be related to the sliding due the presence of local strain. It is very interesting to study the strain response of multilayer to investigate the microstructures and the underlying mechanisms

In addition, structural ripples have been frequently observed as a strain relaxation mechanism in 2D materials, such as graphene [145], ML and FL MoS_2 [146], and other vdW layered materials [147]. The formation of ripples results in the degradation of mobility of the carrier mass and alteration of electronic structures in these 2D materials. Buckling and ripple formation has also been predicted using molecular dynamics (MD) simulations under uniaxial compression [148]. The size of the ripples generated during compression is observed to be associated with the strain rate and length of the sample [149].

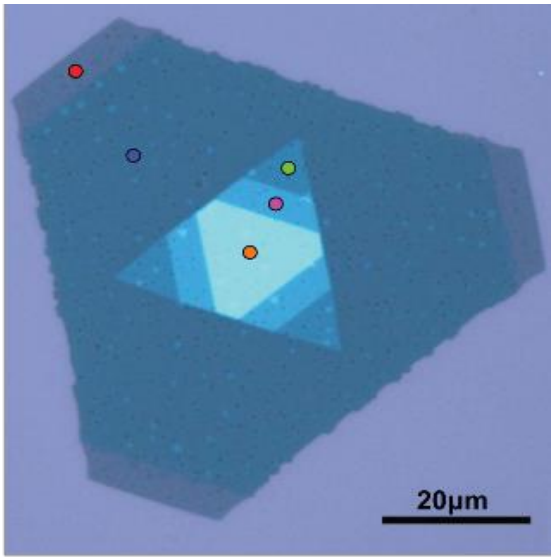

Figure 4.1 Optical image of CVD-grown structures of five-layer MoS_2. Reproduced from Ref. [63].

Recently, ripples are observed near edge terminals in CVD-grown MoS_2 structures (Figure 4.2) [66]. These ripples, with a typical height of ~11 Å, are reported to be responsible for the reduction of band gap of the MoS_2 sheets near edge terminals from 1.96 eV to 1.46 eV. A recent study [150] suggests the formation of ripples in CVD-grown bilayer MoS_2 structures that is induced by strong interlayer edge-to-basal plane coupling.

In addition, the rippling instability is observed in the lower layer due to the interactions with the edges in the top layer.

Thus, while the strain response of MoS_2 structures has been investigated extensively for the case of mechanically exfoliated flakes (with equal dimensions), the understanding of the effects of strain on the mechanical and electronic behavior of CVD-grown MoS_2 structures is still in infancy. Although DFT simulations in chapter 2 suggest that the response of such 2D structures (with unequal dimensions) is likely to create an inequality in the amounts of strain across the layers and hence exhibits inhomogeneous electronic properties [151], these simulations are limited to a system size on the order of a

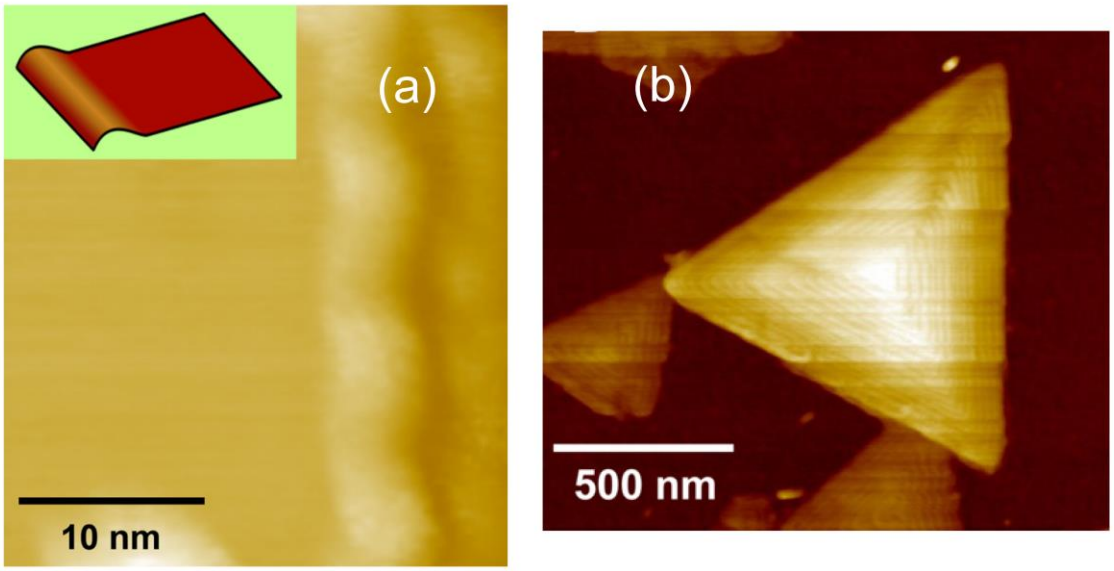

Figure 4.2 (a) STM images of the curved MoS_2 few-layer on GaN substrate. (b) AFM images of multilayer MoS_2 stacked triangles. Reproduced from Ref. [66].

few nanometers. It is also likely that the effect of the presence of edges on the strain response observed at the nanoscale dimensions of the layers is significantly different at the micron scale dimensions as observed experimentally.

Micron scale exceeds the capacity of DFT method, yet can be handled using classical molecular dynamics (MD). Moreover, the DFT simulations focused on the strain response of bilayer structures, hence, the effect of number of layers as well as the mechanism of strain relaxation at the atomic scale remain unknown. As a result, the current study aims to investigate the effect of the size of the layers and mechanism of the strain relaxation of CVD-grown multilayered MoS_2 structures at the experimental length scales using classical MD simulations.

4.2 Simulation Details

In this study, the deformation response of CVD-grown few-layered MoS_2 structures is investigated using a series of large-scale MD simulations with the interatomic interactions defined using a combined reactive empirical bond-order (REBO) [152] and Lennard Jones (LJ) potential. Large-scale MD simulations of model CVD-grown systems are carried out using LAMMPS [153]. The time step for all simulations are defined to be 1 fs. All systems created are first equilibrated at 0 K for 10 ps at constant temperature and zero pressure (NPT ensemble using the Nose-Hoover algorithm), then the equilibrated structure is used as a strain free configuration for the following deformation simulations.

To demonstrate the capability of the combined potential to model the strain response of the CVD-grown MoS_2 structures, MD simulations are first carried out to reproduce the strain response of bilayer MoS_2 structure with free edge as observed using DFT simulations in chapter 2. The bilayer edge structure is shown in Figure 4.3 or Figure 2.3 for details.

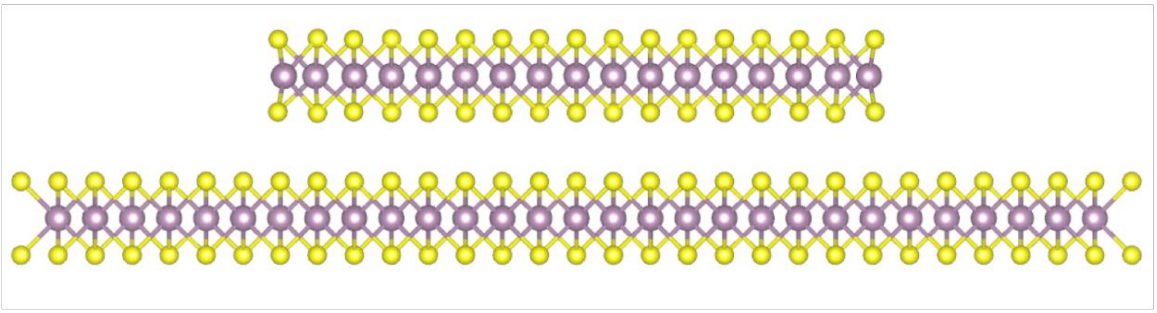

Figure 4.3 Schematic show of the bilayer supercell used in this study.

The system in the 2*H* stacking sequence is rectangular in the basal (XY) plane with the thickness of the two layers to be equal (Y direction), but relatively smaller along the X direction. Three dimensional periodic boundary conditions are applied in the calculations so that the bottom MoS_2 layer is actually infinitely large along X and Y directions, whereas the top layer has a finite width in the X direction and infinitely long along the Y direction. A vacuum space of 20 Å thick is used along the vertical direction of the system to prevent unphysical interactions between adjacent images along this direction. The strain response is investigated under loading conditions of uniaxial tensile strain ($\varepsilon_x \neq 0$, $\varepsilon_y = 0$, $\sigma_x \neq 0$, and $\sigma_y \neq 0$,) where ε_x and ε_y (σ_x and σ_y) are the *average* strains (stresses) of the entire system along the X and Y directions.

The local strain maps [151] under an applied uniaxial strain of ε_x=4 % as computed using DFT and MD simulations are shown in Figure 4.4. It can be seen that the MD simulations using the combined REBO-LJ potential is able to reproduce the strain variations in the two layers as predicted using DFT simulations [151]. The strain in the top layer is observed to be significantly lower as compared to the bottom layer that corresponds to the value of the applied strain (around 4%). Moreover, both methods show that the residual strain in the edge region of the top layer is smaller than the center region, while the opposite trend is observed for the bottom layer. These results demonstrate the capability of the REBO-LJ potential to investigate the mechanical response of the CVD-grown multilayered MoS_2 structures.

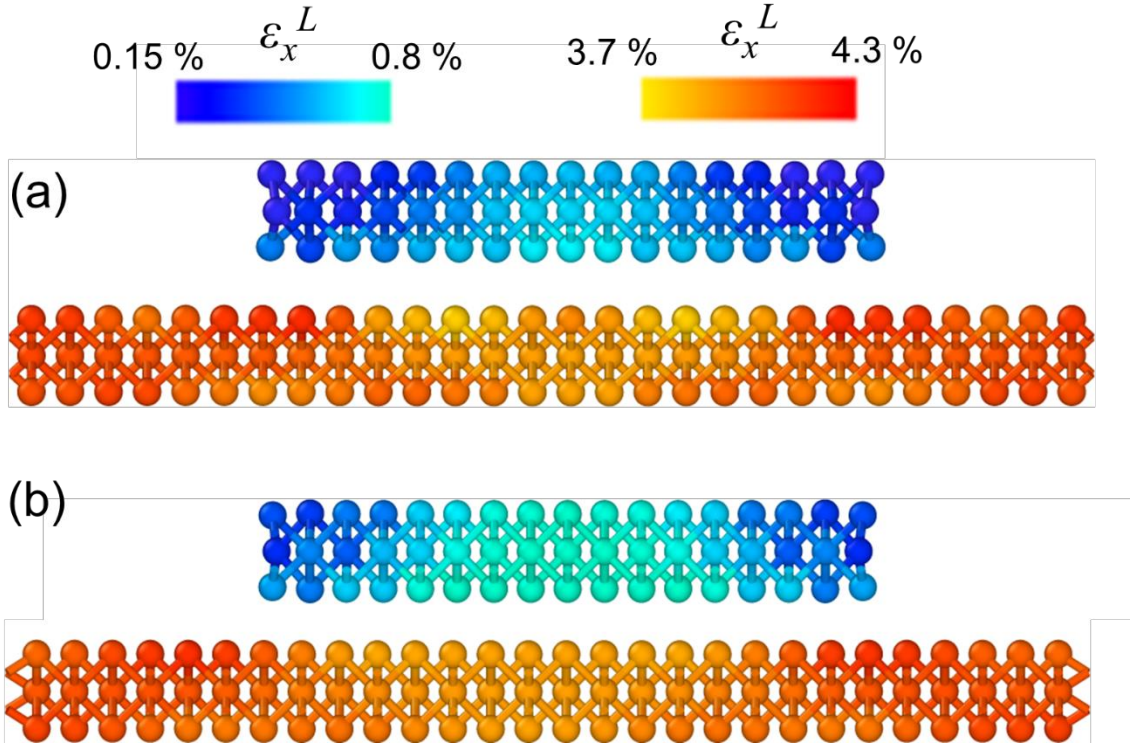

Figure 4.4 Comparison of (a) DFT and (b) MD in local strain map of a bilayer MoS_2 system under an applied uniaxial strain ε_x=4%.

The CVD-grown structures comprise of flakes of few layers wherein the top layers are relatively smaller in size than the bottom layers, resulting in the formation of edges/steps across adjacent layers. To model such a system, a simplified five-layered MoS_2 rectangular system in the basal plane with edges along X direction is created and shown in Figure 4.5. All the layers have the same width in the Y direction (~11 nm), but have varying dimensions in the X direction. The model CVD-grown pyramid structure is created to have a 1/5 decrease in the length of each layer in the X direction as compared to the length of the layer below it. The X dimensions of the as-created pyramid system correspond to ~317

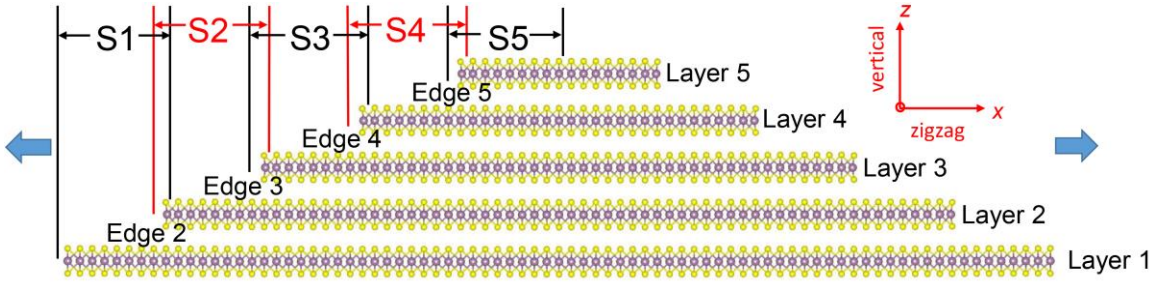

Figure 4.5 Schematic of a model pyramid system used in the study. Uniaxial strain is applied along the X direction as indicated by blue arrow.

nm for the bottom most layer (layer 1), ~254 nm for layer 2, ~203 nm for layer 3, ~164 nm for layer 4, and ~130 nm for layer 5. The thickness of each individual layer is 0.62 nm from our simulation, which leads to 3.1 nm for the five-layer system. The total dimensions of the representative system are 317 nm × 10.98 nm × 31 nm. Periodic boundaries are applied in X and Y directions, and a vacuum space of 20 nm is added in the vertical direction. Such a simplified system creates edges along the X direction, and allows the investigation of the strain response of a particular layer when the free edges may appear both above and below it.

4.3 Strain Configurations of Individual Layer

A uniaxial tensile strain is applied along the X direction in increments of 0.1 % and the system is allowed to relax to minimize the total energy of the system at each increment. The straining is continued to reach a total tensile strain of 6 % which is within the elastic region [154] for the MoS_2 system for the REBO potential. At each increment, a layer strain ($\varepsilon_x^{L_i}$) is calculated for each individual layer as

$$\varepsilon_x^{L_i} = \frac{x_i - x_{i0}}{x_{i0}} \tag{4.1}$$

where i is the layer-id (1, 2, 3, 4, 5); x_i and x_{i0} are final and initial layer length of i^{th} layer in X direction, respectively. The analysis of the layer strain, $\varepsilon_x^{L_i}$, provides the strains of

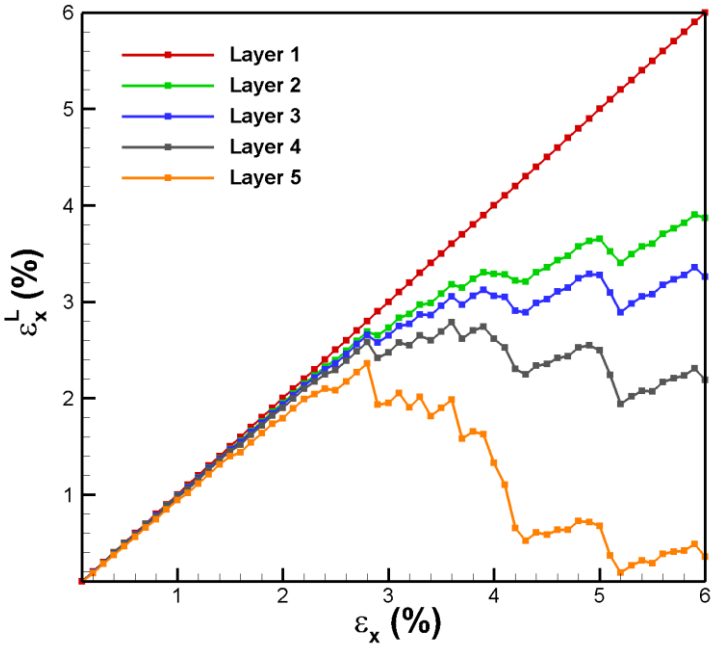

Figure 4.6 Variating of layer strain for each layer as a function of applied strain for 317 nm MoS_2 multilayered structure under uniaxial tension.

each individual layer and enables the investigation of the relaxation of each layer during the straining process.

The variating of $\varepsilon_x^{L_i}$ is plotted as a function of the applied uniaxial tensile strain (ε_x) for each individual layer, from layer 1 to layer 5, in Figure 4.6. It can be seen that the layer strain in the bottom layer varies as the applied external strain. No relaxation of the bottom layer is observed as there are no edges on the bottom layer. However, the variation in the layer strain for the upper layers i.e. layers 2 through 5, is observed to deviate from that observed for the bottom layer with the layer strains being lower than that for the bottom layer. The deviations are observed to be earlier and larger for the higher layers. Such a deviation suggests that the top layers start to relax first due to the presence of a free surface above the top layer, followed by the lower layers. The deviation in the layer strain is therefore larger for the upper layers where vertical relaxation is possible. The layer strain continues to increase with applied strain for each layer up to a certain value, after which a further increase in applied strain results in a drop in the local strain. These reductions in layer strain are observed to occur simultaneously for layer 2 through layer 5. Each reduction is then followed by a small increase in layer strain when strained further. Such increases and decreases in the applied strains continue to occur simultaneously as the applied strain increases, but the deviation in the magnitude of the layer strains is also observed to increase as the applied strain increases. For example, at an applied strain of $\varepsilon_x = 4\,\%$, the layer strains, from layer 2 to layer 5, reduce to 3.29 %, 3.06 %, 2.62 %, 1.33 %, respectively. However, it is not clear if these simultaneous variations are related to the sliding between the layers or due to the slipping of the edges on top of the layers.

4.4 Origins of Ripples under Tensile Strain

To investigate the strain relaxation mechanisms of the various layer strains, an out-of-plane vertical displacement is computed for each atom along the length of layers in the multilayered structure. This vertical displacement (δz_i), at a certain atom *i*, is computed as $\delta z_i = z_i - z_{0i}$, where z_i and z_{0i} are the instantaneous and initial Z-coordinate of atom *i*, respectively [145, 150, 155]. The vertical displacement will be expected to be uniform for the case of sliding between the layers as the strain relaxation mechanism. For the case of the slipping of the edges on the bottom layers, a vertical displacement profile will show high displacements at the edges of each layers. The visual analysis of these vertical displacements for the entire sample, however, become challenging due to the large X-to-Z

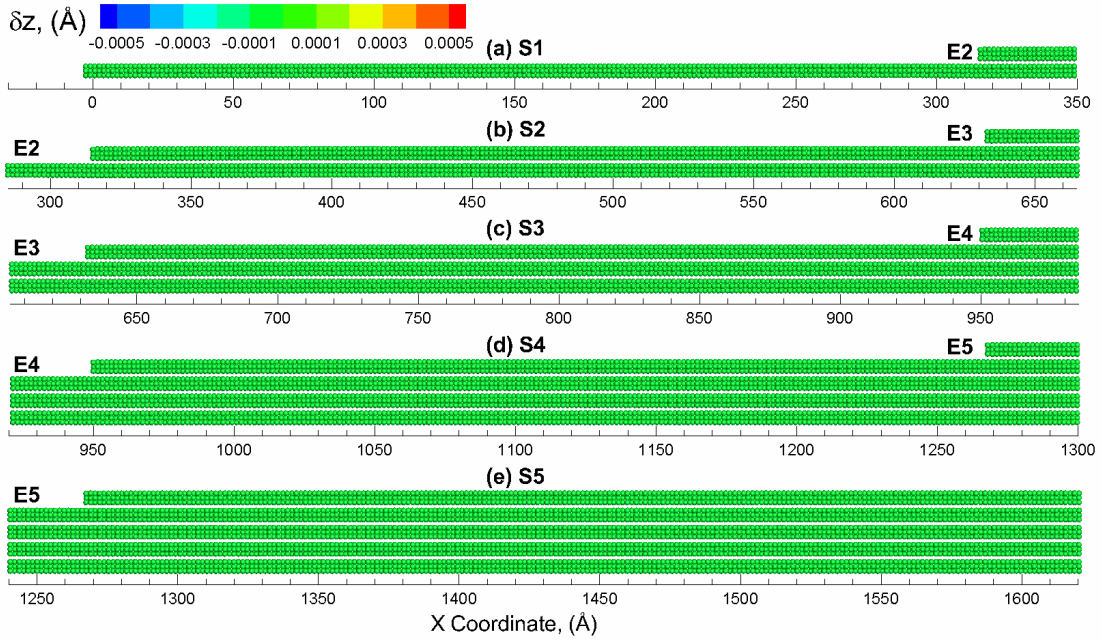

Figure 4.7 The vertical displacement map in the unstrained configuration at different sections: (a) S1, (b) S2, (c) S3, (d) S4 and (e) S5.

ratio (2D structure) of the pyramid structure. As a result, the discussion is now focused on only the left half of the structure along the X direction as the structure is symmetric on both sides. The left half of the pyramid sheet is partitioned to five sections, S1 to S5, to visualize the local variations in vertical displacements at the atomic scale, as shown in Figure 4.5. The five sections overlap with each other to include the terrace and an edge. A total number of four edges are investigated in this paper, noted as E2 to E5.

Figure 4.7 shows the displacement map for sections S1 to S5 of the left half of the MoS_2 pyramid at unstrained configuration. The atoms are colored by the displacement in the Z direction with the positive value (red color) corresponding to an upward displacement and a negative value (blue color) indicating a downward displacement as compared to the unstrained configuration. At strain free configuration ($\varepsilon_x = 0\%$), there is no displacement along vertical direction for all atoms. Therefore, δz_i of all the atoms equals to zero and these atoms are colored in green, as shown in Figure 4.7.

The vertical displacement can now be applied to investigate the response of the pyramid structure. The vertical displacements in the various sections of the pyramid structure at an applied strain of $\varepsilon_x = 0.1\%$ are shown in Figure 4.8. As can be seen in the snapshots, the top layer (sulfur atoms) of each section is displaced downwards (blue) and the bottom layer (sulfur atoms) is displaced upwards. It can be seen that the displacement is uniform along the length of each section and the maximal displacement is computed to be ~ 0.0005Å at an applied strain of $\varepsilon_x = 0.1\%$. The uniform straining of the layers

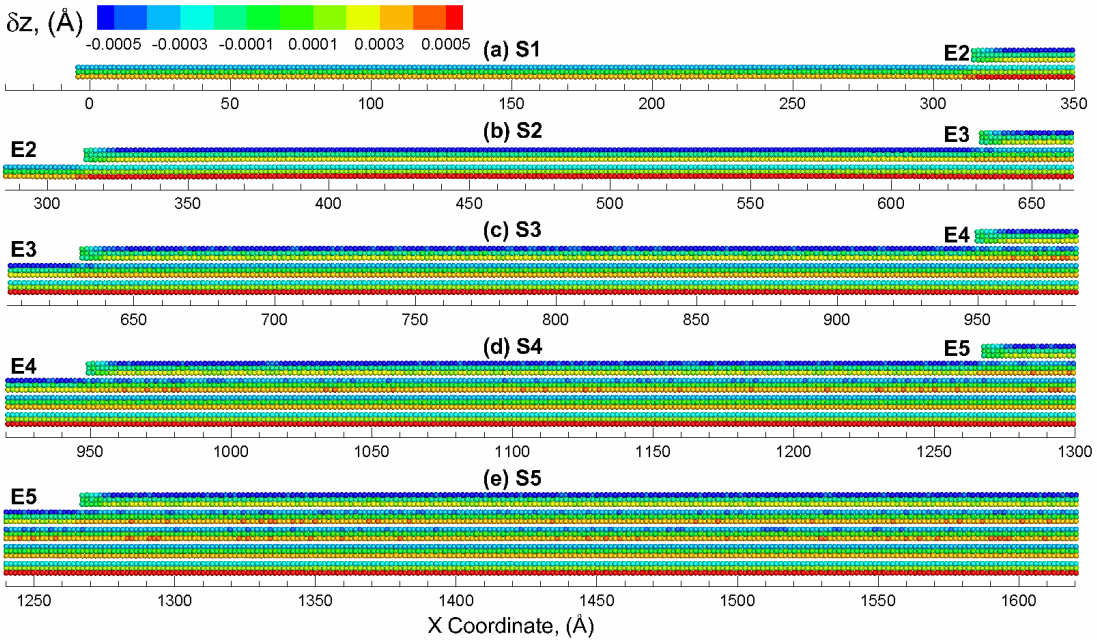

Figure 4.8 The variation of the vertical displacement in the various sections (a) S1, (b) S2, (c) S3, (d) S4 and (e) S5 of the multilayered structure at an applied strain of 0.1 %

continues to increase up to an applied strain of $\varepsilon_x = 2\,\%$, wherein a deviation is observed in the layer strains in Figure 4.6.

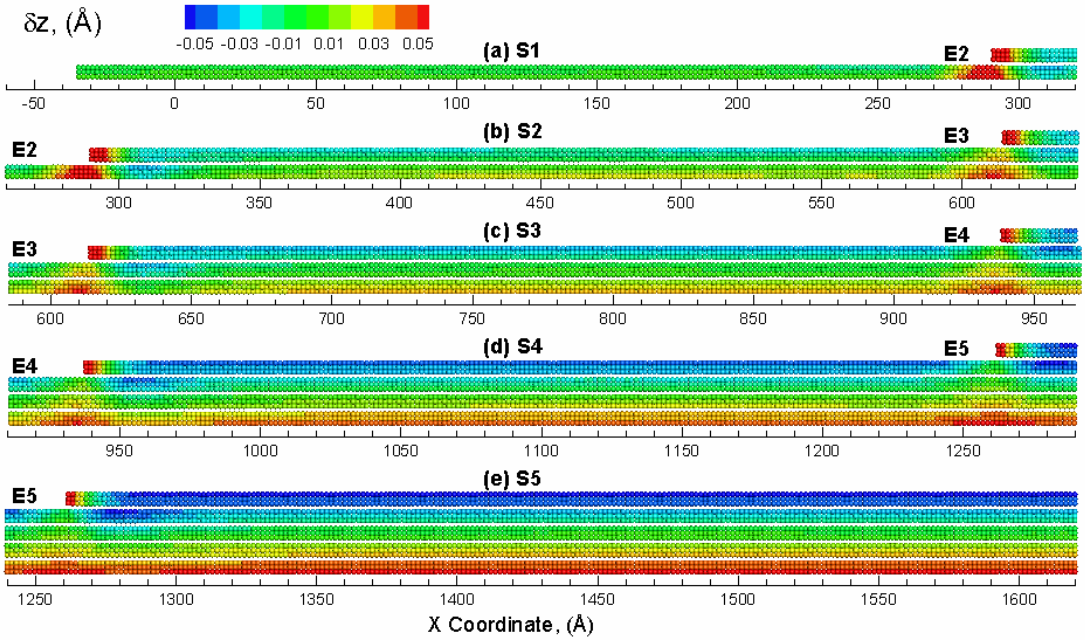

Figure 4.9 Snapshots of different sections (a) S1, (b) S2, (c) S3, (d) S4 and (e) S5 of the multilayered structure at 2% strain showing formation of ripples at the edge region.

The vertical displacements in the various sections of the pyramid structure at an applied strain of $\varepsilon_x = 2\,\%$ are shown in Figure 4.9. It can be seen from the snapshots that a vertical displacement is observed at the edges in each of the sections. This vertical displacement of the edge also results in a vertical displacement of the layers below in the edge region as suggested by the red colored atoms. This vertical displacement of the edge region is also compensated by having a slight downward displacement (as shown by blue color) in the region next to the edge region. This upward/downward displacement of the edges, as will be discussed later, results in the nucleation of ripples that result in the

variations in the layer strains plotted in Figure 4.6. The generated ripple can be observed at the right side of E2 as shown in Figure 4.9 (b). The ripple is more visible at the right side of E3 (Figure 4.9 (c)), E4 (Figure 4.9(d)) and E5 (Figure 4.9(e)). No ripple is nucleated in S1, as indicated by Figure 4.9 (a). This strain (~2 %) coincides with the strain at which the local layer strain of top layers starts to deviate the applied strain (as discussed before). As a result, the relaxation of the top layers may be attributed to the ripples induced by the edge.

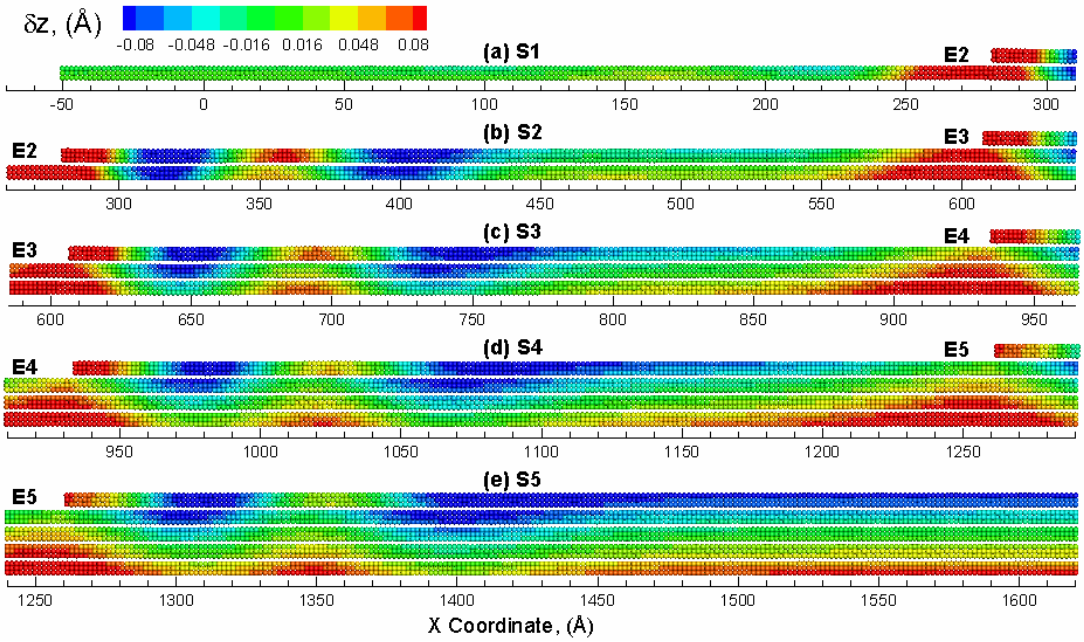

Figure 4.10 Snapshots of different sections (a) S1, (b) S2, (c) S3, (d) S4 and (e) S5 of the multilayered structure at 3 % strain showing propagation of ripples from edge towards center.

Further straining of the structure results in propagation of the nucleated ripples as well as nucleation of new ripples. The vertical displacements in the various sections of the pyramid structure at an applied strain of $\varepsilon_x = 3\%$ are shown in Figure 4.10. As shown in Figure 4.10 (a), ripples are still not seen in section S1 as the strain increases to 3%.

However, another ripple is nucleated at the edge region in other four sections (Figure 4.10 (b) to (e)). All of these ripples propagate from edge region towards the center of the structure, i.e., from left towards right. The number of ripples propagating in each section, i.e. 2 at $\varepsilon_x = 3\%$ is the same. It should be noted that the top layers in each section show significant downward displacement (suggested from more blue atoms) as compared to the remaining layers in each section. This displacement attributed to the edges of the top layers results in the reduction in the layer strain for the top layers, as seen in Figure 4.6.

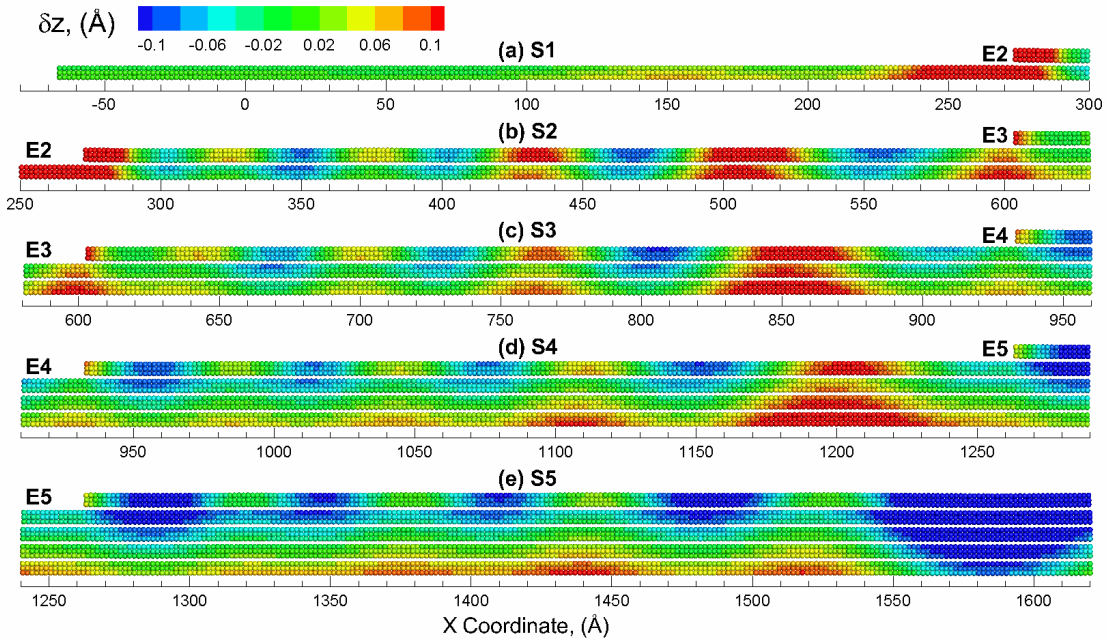

Figure 4.11 Snapshots of different sections (a) S1, (b) S2, (c) S3, (d) S4 and (e) S5 of the multilayered structure at 4 % strain showing ripples across the length of each section.

An applied strain of $\varepsilon_x = 4\%$ results in the propagation of ripples across the length of the sections as shown in Figure 4.11. The number of ripples propagating in each section is the same except for that observed in section S1, where the ripples only propagate towards the half way for an applied strain of $\varepsilon_x = 4\%$. However, five ripples are observed (indirectly

implied by number of blue regions in the area) to be propagating in section S2. For sections S3, S4 and S5, five propagating ripples can be explicitly observed. It is also interesting to note that the ripples generated in section 4, propagate along the length of the section and interact with the edge (E5) in section 5 where ripples are nucleated in section 5.

For the section S5 which belongs to the left half of the system, ripples are also

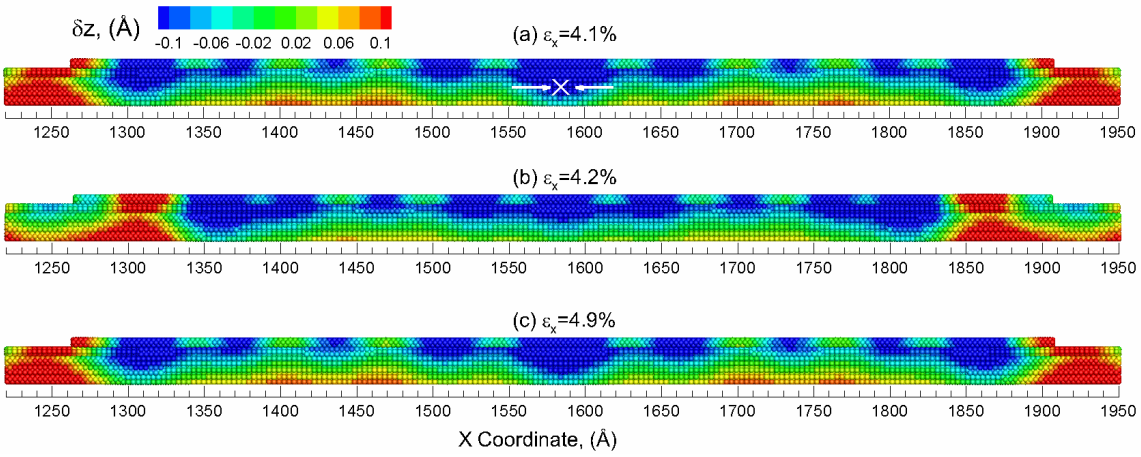

Figure 4.12 Snapshots of center of pyramid system at various strains (a) 1%, (b) 4.2%, and (c) 4.9% showing propagation of ripples at the edge region.

generated in the right half of the system due to the edge that propagate towards the center of the multilayered structure i.e. from right to left. The ripples created meet and interact at the center of the system to create a large downward displacement (blue) region at the center of the multilayered system as shown in Figure 4.12(a). Further strain results in the propagation of this downward displacement region in the opposite direction of the ripples as shown in Figure 4.12(b). Continued applied strain results in the nucleation of new ripples at the edges that propagate again towards the edges as shown in Figure 4.12(c).

4.5 Formation of Ripples under Compressive Strain

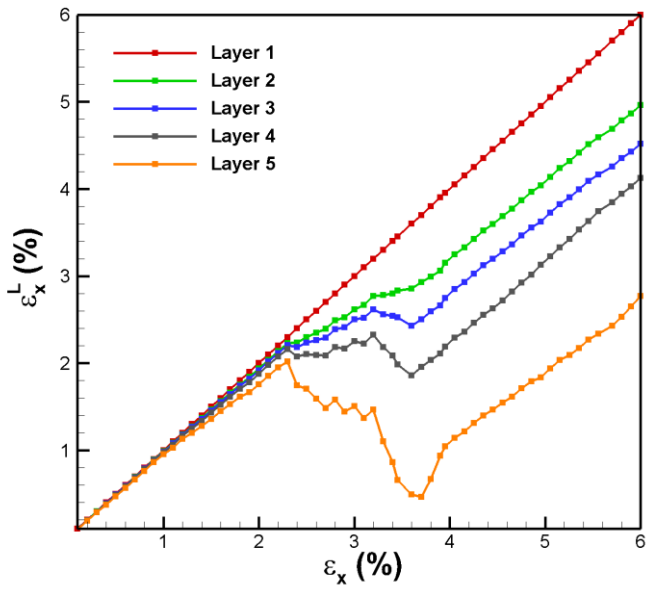

Figure 4.13 Variating of layer strain for each layer as a function of applied strain for 317 nm MoS2 multilayered structure under uniaxial compression.

The discussion so far has focused on the strain relaxation response under loading conditions of uniaxial tensile strain. The multilayered structure is also subjected to compressive strains to investigate the strain response and ripple formation behavior. The variation of layer strain ($\varepsilon_x^{L_i}$) for each individual layer in multilayered structure as a function of applied uniaxial compressive strain (ε_x) is shown in Figure 4.13. The variation of $\varepsilon_x^{L_i}$ is initially linear with ε_x . Similar to that observed for tensile strains, $\varepsilon_x^{L_i}$ is observed to relax at larger applied strains through the nucleation and propagation of ripples. However, there exist a few noticeable differences in the case of compressive loading. The amount of layer strain relaxation in top layers during compression is considerably larger than that observed during tension. As will be discussed later, the larger relaxation of strain

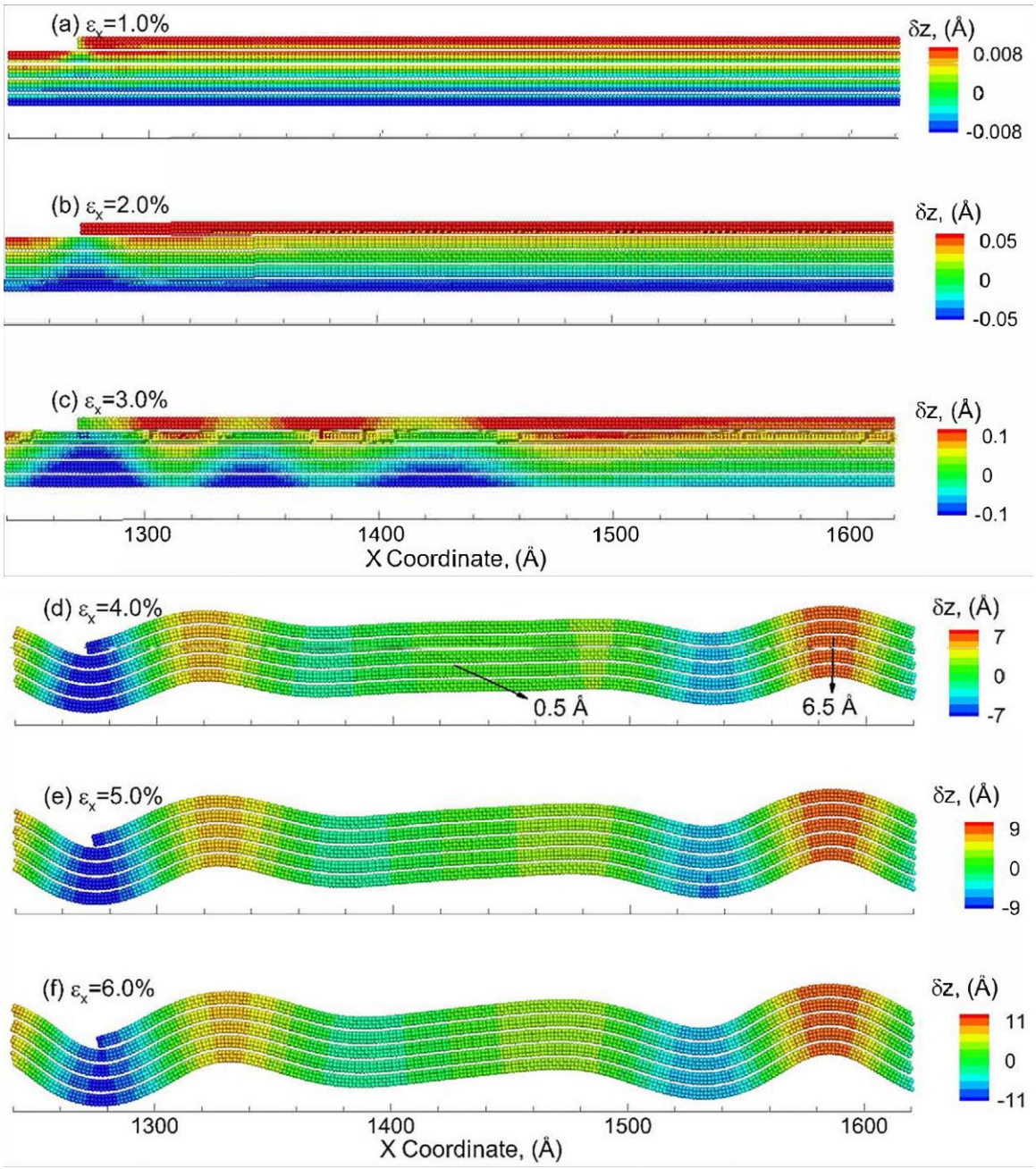

Figure 4.14 Snapshots of S5 showing propagation of ripples at the edge region at applied compressive strains of (a) 1%, (b) 2%, (c) 3%, (d) 4%, (e) 5% and (f) 6%.

is attributed to the larger amplitudes of the ripples under compression as compared to that under tension. In addition, as the applied compressive strain exceeds $\varepsilon_x = 3.75\,\%$, $\varepsilon_x^{L_i}$ increases consistently with the applied strain. Such a re-emerged increase in the layer strain

indicates that no additional strain is relaxed through additional nucleation of ripples. Thus, there is a limit for the relaxation of the layers that can be attributed to the formation of ripples.

The vertical displacements in the section S5 of the pyramid structure at various values of applied strain of are shown in Figure 4.14. The right side of the multilayered structure is shown here. The vertical displacements are fairly uniform in the section at an applied compressive strain of $\varepsilon_x = 1$ % as shown in Figure 4.14(a). Continued strain results in the nucleation of ripples at the edge E5 as shown in Figure 4.14(b). Further applied strain nucleates more ripples that propagate towards the center of the structure as shown in Figure 4.14(c). The most significant difference under compressive loading is observed at an applied compressive strain of $\varepsilon_x = 4$ %, wherein the amplitude of the ripples exceeds 8 Å (~8.6 Å) at the edge of section S5. The amplitude, however, reduces to 6.5 Å at the center of the pyramid (right side of S5 in Figure 4.14(d)) where the ripple initiated from the right edge merges with the left one. The maximum number of ripples are observed at an applied compressive strain of $\varepsilon_x = 4$ %. Application of additional compressive strain does not result in nucleation of additional ripples. This can be seen from vertical displacements in Figure 4.14(f) at an applied compressive strain of $\varepsilon_x = 6$ % wherein the number of ripples propagating across section S5 is the same as those observed at an applied compressive

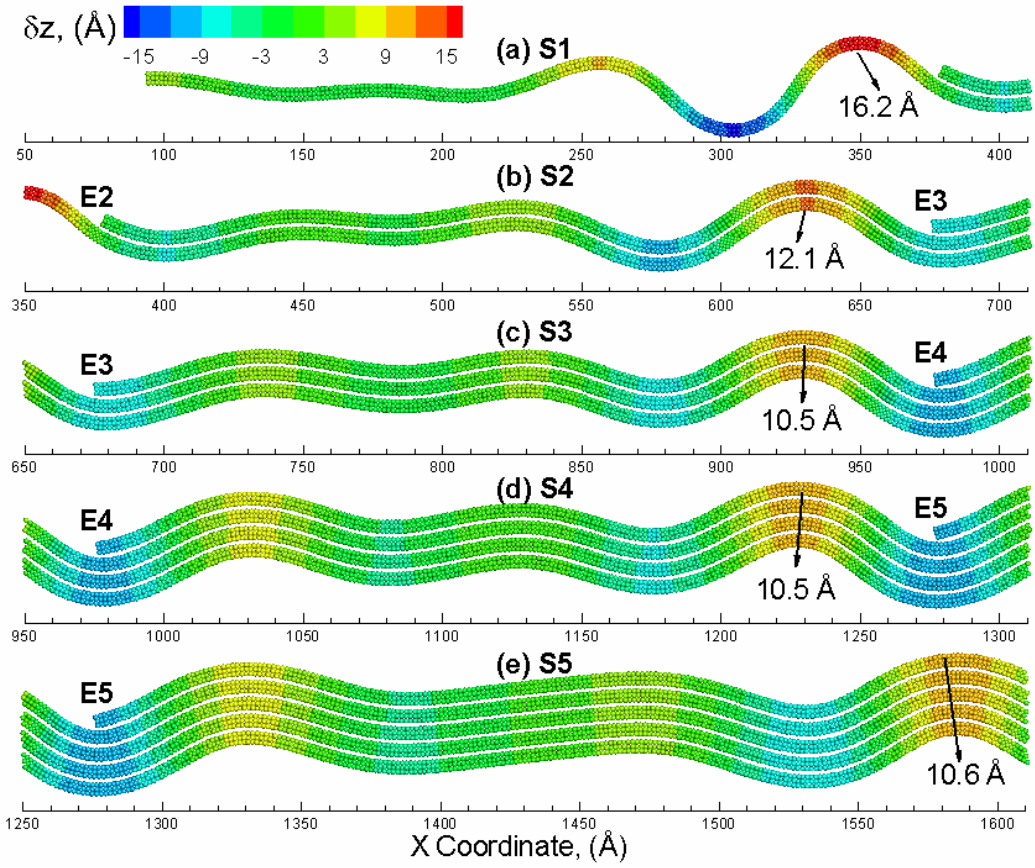

Figure 4.15 Snapshots of the sections (a) S1, (b) S2, (c) S3, (d) S4 and (e) S5 of 317 nm as-grown MoS_2 structure at applied compressive strains of 6%.

strain of $\varepsilon_x = 4\,\%$. The only difference at the two strains, however, is the amplitude of the ripples, which is implied by the different legends of the two snapshots.

The vertical displacements for sections S1 to S5 at an applied compressive strain of $\varepsilon_x = 6\,\%$, are shown in Figure 4.15. Ripples are observed to nucleate at the edges for all the sections and propagate towards the center of the multilayered structure. The peak amplitude of the ripples in sections S1, S2, S3, and S5 are calculated to be 16.2 Å, 12.1 Å, 10.5 Å, 10.5 Å, 10.6 Å, respectively. These amplitudes of the ripples are comparable to the

amplitudes of the ripples observed experimentally. Thus, a larger amplitude is observed for sections with lower number of layers, especially when the number of layers is less than three. The slightly larger amplitude in S5 (5 layers) as compared to that observed for section S4 (4 layers) is attributed to the interaction and merger of two ripples in S5.

While ripple formation has been reported using previous MD studies for the case of single layer MoS_2 sheets, the mechanism of ripple formation is attributed to buckling of the sheet under compression. The presence of edges in the multilayered structure considered here provides the necessary displacements to relax strain through the formation of ripples. These edge configurations therefore form the origins of ripple formations in these CVD-grown structures. To verify this, a five-layered MoS_2 sheet with the same dimensions as section S5 of the multilayered structure is created with equal dimensions of all layers (i.e. no edges) and is subjected to uniaxial compression as discussed before. The no-edge multilayered MoS_2 structure comprises of 317 nm in X direction and 10.98 nm in y direction, which is of same size as the bottom layer in 317 nm CVD-grown MoS_2 multilayer. The top four layers are of the same dimensions as bottom layer in this no-edge multilayered MoS_2 structure. The MD simulations of uniaxial tensile strain indicate that no strain relaxation is observed in the periodic sheet and the layer strain $\varepsilon_x^{L_i}$ for each layer is observed to the be the same as the applied strain for all the layers up to an applied strain of $\varepsilon_x = 4\,\%$. Thus, no ripples are generated without the presence of the edges, verifying the primary role of edges in ripple formation and strain relaxation of CVD-grown multilayered structures.

4.6 Size Effects on Strain Response

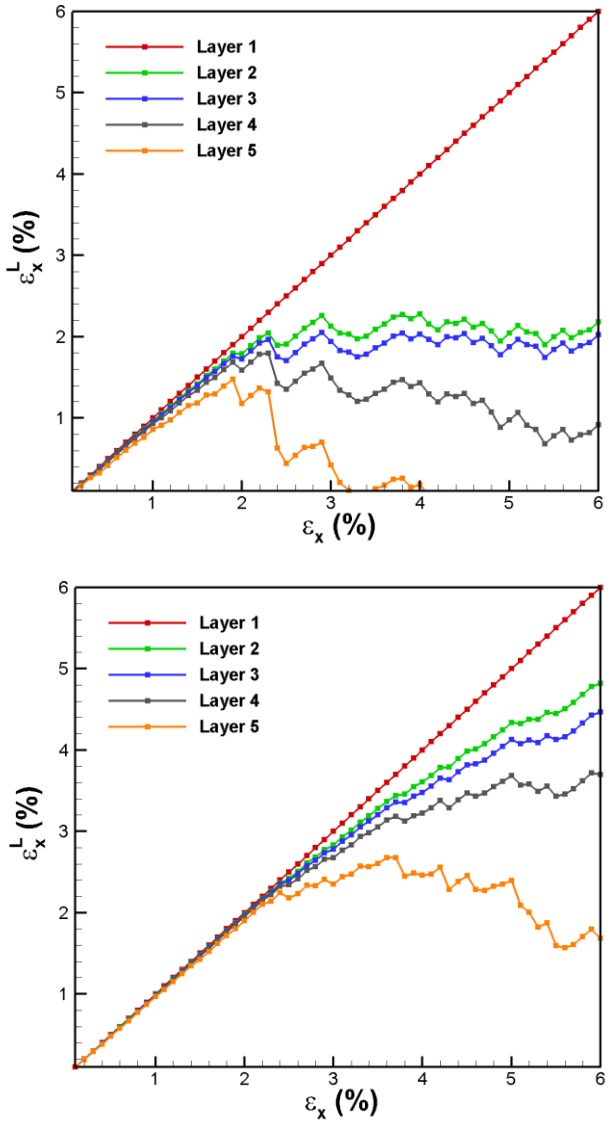

Figure 4.16 Local layer strain as a function of applied strain for (a) 127 nm, (b) 634 nm as-grown multilayered MoS_2 structure under uniaxial tensile strain.

Another factor to consider in the role of edges on the formation of ripples is the size of the terrace structures between the edges. As a result, two multilayered MoS_2 systems are created with the same ration of the lengths of the layers, but with the dimensions of ~127 nm for the bottom layer (defined as the small system) and ~634 nm for the bottom layer

(defined as the large system). The variation of the layer strain ($\varepsilon_x^{L_i}$) for each individual layer in the no-edge MoS_2 multilayer structure as a function of applied uniaxial tensile strain (ε_x) is presented in Figure 4.16. Simultaneous relaxation is noticeably observed in 127 nm system and slightly in 634 nm system. For all the cases, $\varepsilon_x^{L_i}$ in the bottom layer is identical to ε_x, and top four layers relax to various extent. The relaxation strains of the top layer (fifth layer) are calculated to be 1.85%, 2.75% and 3.75% for 127 nm, 317 nm and 634 nm system, indicating the strains required to nucleate ripples increases with the larger dimensions of the terraces (layers). An edge-to-bulk ratio (EBR) ratio can be defined for the layers in 2D MoS_2 structure to investigate the significance of edges in strain relaxation. For the multilayered structure considered here that is periodic in the Y direction, it is evident that a larger length in X direction will result in a smaller EBR, thus decreasing edge effect. It is revealed from Figure 4.6 and Figure 4.16 that the values of the $\varepsilon_x^{L_i}$ decrease from bottom to the top layer, which is attributed to the diminishing EBR. The atoms in the top layers tend to relax to a larger extent due to more severe edge effect that results in vertical displacements and formation of ripples. Similarly, the layers in a larger sized pyramid have a smaller EBR, thus a smaller amount of strain reduction.

4.7 Conclusions

Molecular dynamics simulations are carried out to investigate the strain response of CVD-grown MoS_2 structures at the atomic scales. To investigate the strain response, a model multilayered system with terraces and edges is created to mimic the CVD-grown system. The interatomic interactions between the Mo/S atoms are defined using a hybrid

REBO/LJ potential that is able to reproduce the strain response of a bilayer system with an edge as predicted using DFT simulations. The MD simulations suggest that the strain response of the multilayered system is layer dependent and the relaxation of individual layers is attributed to nucleation, propagation and interaction of ripples. The ripples are observed to nucleate at the locations of the edges of the layer in the regions below the edge and propagate inward to the center of the multilayered structure. It is also predicted by the MD simulations that the ripples formed have vertical displacements of ~0.1 Å for uniaxial tensile strain and ~10 Å for uniaxial compressive strain. The strains required for the formation of ripples are observed to be dependent on the dimensions of the layers. It should be pointed out that current study is performed without a substrate so that the model is simplified enough to reveal the underlying origins of the ripples. As a result, the effects of substrate are not considered. In more realistic cases, the interaction between substrates and MoS_2 sample is supposed to create Moiré patterns, and the relations between these Moiré patterns and the formation/propagation of ripples will be also very intriguing to study. The formation of ripples in CVD-grown few-layered structures under strain need to be accounted for when analyzing strain effects on electronic properties of these CVD-grown structures materials using experimental methods or in continuum models. The strain response of CVD-grown structures through ripple formation also shows promise for the use of strain engineering to generate inhomogeneous electronic properties for the design novel devices based on CVD-growth MoS_2 structures.

CHAPTER FIVE

5. ORIGINS OF MOIRÉ PATTERNS FOR STRAINED CVD-GROWN BILAYER MoS_2 TRIANGLES

5.1 Introduction

As shown in chapter 4, the strains in top layers of the multilayered MoS_2 structures are not necessarily identical to those at bottom layers. relaxed through nucleating ripples at the presence of edges. It has been observed that the strains in top layers of the multilayered MoS2 structures may be relaxed through nucleating ripples [66, 150, 156] or slippage [141]. Similarly, due to the weak interacting nature (van de Waals) between substrate and samples, the strain subjected to the substrate cannot be completely transferred to the 2D samples, especially in multilayered MoS_2 structures. The vertically heterogenous strain configurations across layers can induce/engender lattice mismatch between different layers, which results in a Moiré-like superstructure in individual layers, i.e., Moiré pattern [157] .

The lattice-mismatched Moiré-pattern structures are considered as the evidence of successful alignment/growth of heterostructures, and have been extensively observed in many vdW heterostructures [68-72], graphene-metal interface [73] as well as MoS_2-metal interfaces [74-77]. For example, the graphene-hBN heterostructure with a lattice mismatch of 1.8% shows a Moiré pattern with a well-defined periodicity of ~15 nm [68, 70, 71],

which is confirmed by the molecular dynamic simulations [158]. These superlattices are reported to have a non-uniform out-of-plane displacement in the magnitude of ~0.2 nm [158]. The Moiré pattern with a periodicity of 8.7 nm also emerges in rotationally aligned MoS_2-WSe_2 bilayer [72]. The Moiré-like superstructures exhibit distinct electronic properties as compared to the constituent layers. It has been observed that the Moiré structure in MoS_2-WSe_2 bilayer presents a periodic local-bandgap variation with an amplitude of ~ 150 meV and the band edges are observed to be located at different layers [72]. Recently, large-area single layer MoS_2 ($SLMoS_2$) are epitaxially grown on Au (111) surface [74-77, 159]. A relatively large Moiré distance of ~ 30 nm is reported. Although the interaction between metal substrate and $SLMoS_2$ has less pronounced consequences on the electronic structure as compared to graphene-metal interface due to the in-plane nature of the orbitals in MoS_2 [159], the band structure near the K-point are evidently affected and a noticeable Mo 4d states are observed [159, 160].

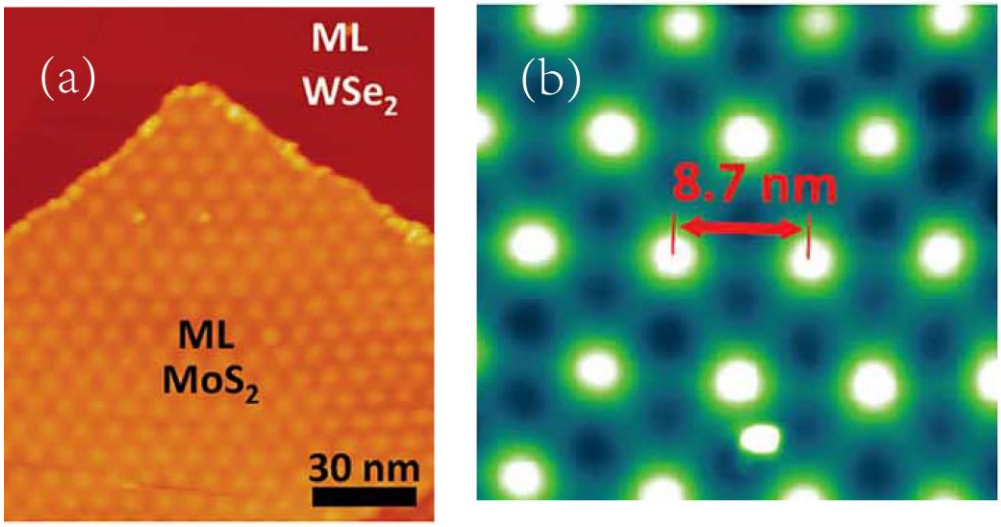

Figure 5.1 (a) STM images of MoS_2/WSe_2 heterostructure; (b) Close-up STM image show the Moiré pattern with a periodicity of ~8.7 nm. Reproduced from Ref. [72].

Although the strain configurations of the CVD-grown MoS_2 structures have been investigated under the external strain with both DFT (chapter 2) [151] and MD simulations (chapter 4) [156], the modeled MoS_2 multilayer has a rectangular shape with edges only in X direction, while the system is periodic in Y direction. It was a simplified model to qualitatively study the effect of edge on the electronic structure and the strain response. In realistic, CVD-grown MoS_2 structures have a structure of stacked triangles. The top layers are relatively smaller in size and rotate 180^0 as compared to the bottom ones, forming more complicated edges/steps. In this study, MD simulations are carried out to investigate the strain response of bilayer MoS_2 with a triangular shape. This bilayered MoS_2 triangle is placed on top of a relatively larger rectangular MoS_2 monolayer, which is treated as a substrate layer. The external strain is applied to the MoS_2 substrate layer, and the strain response of the stacked bilayer shows a Moiré-like picture due to the non-uniform distribution of out-of-plane displacement. The strains in the bilayer are found to be relaxed by the nucleation of "Moiré islands".

5.2 Computational Methods and Interatomic Potential

Large-scale MD simulations of model CVD-grown systems are carried out using LAMMPS [153] with the interatomic interactions defined using the reactive empirical bond-order (REBO) potential [95] combined with a Lennard Jones (LJ) potential. The time step for all simulations are defined to be 1 fs. All systems created are first equilibrated at 0 K for 10 ps at constant temperature and zero pressure (NPT ensemble using the Nose-Hoover algorithm), then the equilibrated structure is used as a strain free configuration for the following deformation simulations. The energy for an atom in the REBO formulation is calculated as:

$$E_{REBO} = \frac{1}{2}\sum_{i \neq j} f_{ij}^{C}(r_{ij})\left[V^{R}(r_{ij}) - b_{ij}V^{A}(r_{ij})\right] \tag{5.1}$$

where r_{ij} is the distance between atoms i and j, $f_{ij}^{C}(r_{ij})$ is a cutoff function and smoothly switches REBO to LJ. $V^{R}(r_{ij})$ and $V^{A}(r_{ij})$ are repulsive and attractive portion, respectively.

$$V^{R}\left(r_{ij}\right) = \left(1 + \frac{Q_{ij}}{r_{ij}}\right) A \cdot e^{-\alpha \cdot r_{ij}}, \; V^{A}(r_{ij}) = B \cdot e^{-\beta \cdot r_{ij}} \tag{5.2}$$

The intralayer vdW interaction is described by the LJ potential:

$$E_{LJ} = 4\varepsilon_{ij}\left[\left(\frac{\sigma_{ij}}{r_{ij}}\right)^{12} - \left(\frac{\sigma_{ij}}{r_{ij}}\right)^{6}\right] \tag{5.3}$$

Table 5.1 (a) Optimized parameters for the Mo-S interatomic potential. The energy is in the unit of eV, and the length in Å.

Parameter	Mo-Mo	S-S	Mo-S
A	123.5155	859.9026	401.7058
B	494.3735	1049.054	947.8501
α	1.075007	1.10775	1.192679
β	1.161003	1.126736	1.269738
σ	4.6	3.13	3.625741
ε	0.000586	0.01876	0.003315

To model strain response of triangular-shaped MoS_2 2D structures, it is essential to the interatomic potential is able to capture the correct strain configuration of individual layers. As discussed before, these stacked triangles exhibit more realistic and sophisticated edge configuration. As a result, the original potential parameters are re-optimized to better capture the strain response at the presence of edges/steps. The strain relaxation of the elastic deformation depends not only on the in-plane covalent bonds, but also on the vertical van de Waals interaction between interlayer atoms. The lattice constants and the elastic constants predicted are chosen as the structural and energetic indicators, respectively. First, the pair-terms of the covalent parameters, *A, B, α, β* in Eq. (2) are tuned to provide accurate lattice constants and cohesive energy. Then the well-depth, ε_{ij}, and the equivalent distance, σ_{ij}, in the LJ potential are adjusted to match the elastic constants and bulk modulus. After more than hundreds sets of parameters (Table 5.1 (b) and (c)), an optimal parameterization of REBO potential is shown in Table 5.1 (a).

Table 5.1 (b) The parameters tried in this thesis. The parameters are the listed as the ratio with respect to corresponding parameters of the original REBO paper from Liang [95].

	A11	*A12*	*A22*	*B11*	*B12*	*B22*	*a11*	*a12*	*a22*	*b11*	*b12*	*b22*	σ *22*	ε *22*
Case 1	1.000	1.000	1.000	1.000	1.000	1.000	1.000	1.000	1.000	1.000	1.000	1.000	3.130	0.01600
Case 8	0.700	0.700	0.700	0.700	0.700	0.700	0.980	0.980	0.980	0.980	0.980	0.980	3.130	
Case 15	0.700	1.000	0.700	0.700	1.000	0.700	0.980	0.980	0.980	0.980	0.980	0.980		
Case 21	0.700	0.700	0.700	0.700	0.702	0.700	0.980	0.980	0.980	0.980	0.980	0.980		
Case 33	0.700	0.700	0.700	0.700	0.701	0.700	0.980	0.980	0.980	0.980	0.980	0.980	3.230	
Case 40	0.700	0.700	0.700	0.700	0.705	0.700	0.980	0.975	0.980	0.980	0.980	0.980	3.230	
Case 55	0.700	0.700	0.700	0.700	0.702	0.700	0.975	0.975	0.975	0.975	0.975	0.975	3.200	
Case 62	0.700	0.700	0.700	0.700	0.702	0.700	0.977	0.975	0.975	0.975	0.975	0.975	3.200	
Case 82	0.700	0.700	0.700	0.700	0.700	0.700	0.980	0.980	0.980	0.980	0.980	0.980	3.230	
Case 91	0.690	0.700	0.700	0.700	0.705	0.700	0.980	0.975	0.980	0.980	0.980	0.980	3.150	
Case 102	0.690	0.698	0.700	0.700	0.705	0.700	1.000	1.000	1.000	1.000	1.000	1.000	3.130	0.01876
Case 103	0.621	0.628	0.630	0.630	0.635	0.630	1.000	1.000	1.000	1.000	1.000	1.000	3.130	0.01876
Case 104	1.000	1.000	1.000	1.000	1.000	1.000	1.000	1.000	1.000	1.000	1.000	1.000	3.130	0.01600
Case 105	0.690	0.698	0.700	0.700	0.705	0.700	1.000	1.000	1.000	1.000	1.000	1.000	3.130	0.02000
Case 117	0.690	0.698	0.700	0.700	0.705	0.700	1.000	1.000	1.000	1.000	1.000	1.000	3.130	0.01890
Case 122	0.690	0.698	0.700	0.700	0.705	0.700	1.000	1.000	1.000	1.000	1.000	1.000	3.130	0.01876

Table 5.1 (c) The lattice constants and elastic properties of bulk MoS_2 from DFT, experiments and MD calculation with different parameterization.

	c11	c33	c12	c13	c44	c66	b0	E_{coh}	*a*	*c*	d_{mos}	d_{ss}	d_{intra}
DFT	**218.80**	**47.30**	**51.30**	**5.40**	**14.10**	**83.70**	**37.80**	**-16.009**	**3.158**	**12.112**	**2.400**	**3.120**	**2.936**
Exp.	**238.00**	**52.00**	**-54.00**	**23.00**	**19.00**				**3.160**	**12.294**	**2.417**	**3.172**	**2.975**
Spearot	255.32	36.62	77.21	7.71	6.13	89.01	32.16	-21.584	3.166	12.173	2.443	3.241	2.845
Liang	269.00	50.00	81.50	10.70	8.45	93.19	42.41	-21.668	3.174	12.180	2.445	3.238	2.852
Case 1	266.00	47.40	80.70	10.10	8.03	92.75	40.45	-21.651	3.173	12.179	2.445	3.239	2.851
Case 8	215.53	47.01	66.04	9.84	7.99	75.01	38.79	-17.239	3.169	12.148	2.438	3.222	2.851
Case 15	267.51	46.31	74.49	9.52	8.01	96.28	39.48	-22.988	3.194	12.103	2.444	3.209	2.843
Case 21	227.64	47.81	68.90	9.89	8.00	79.37	39.66	-17.930	3.156	12.097	2.423	3.195	2.854
Case 33	232.55	46.82	70.37	8.87	7.25	80.91	38.84	-17.502	3.186	12.341	2.440	3.205	2.965
Case 40	213.65	45.54	64.76	8.70	7.22	74.23	37.43	-15.575	3.206	12.417	2.462	3.248	2.961
Case 55	239.99	47.68	72.58	9.19	7.47	83.58	39.70	-18.417	3.174	12.254	2.431	3.194	2.934
Case 62	242.24	48.15	73.75	9.35	7.48	84.45	40.12	-18.609	3.160	12.261	2.425	3.194	2.937
Case 82	226.33	46.43	68.82	8.90	7.24	78.69	38.44	-17.162	3.192	12.366	2.447	3.219	2.964
Case 91	208.40	47.60	65.02	10.06	7.84	71.90	39.02	-16.028	3.160	12.289	2.448	3.264	2.880
Case 102	242.88	50.58	74.21	10.11	8.03	84.63	41.91	-17.903	3.112	12.031	2.390	3.150	2.865
Case 103	228.25	50.38	69.35	9.93	8.02	79.18	41.26	-16.375	3.112	12.008	2.386	3.139	2.865
Case 104	260.12	41.41	78.89	8.98	6.98	90.71	35.96	-21.614	3.169	12.177	2.444	3.240	2.849
Case 105	246.26	53.30	74.96	10.57	8.50	85.63	43.83	-17.917	3.115	12.032	2.390	3.150	2.866
Case 117	243.24	50.89	74.32	10.16	8.09	84.74	42.13	-17.905	3.113	12.031	2.390	3.150	2.865
Case 122	242.88	50.58	74.21	10.11	8.03	84.63	41.91	-17.903	3.112	12.031	2.390	3.150	2.865

Table 5.2 The lattice constants and elastic properties of bulk MoS_2 from DFT, experiments and MD calculation with different parameterization.

	a (Å)	c (Å)	d_{Mo-S} (Å)	d_{S-S} (Å)	d_{int} (Å)	E_{coh} (eV)	C_{11} (GPa)	C_{33} (Gpa)	B_0 (GPa)
DFT	3.16	12.11	2.4	3.12	2.94	-16.01	218.8	47.3	37.8
exp. [a, b]	3.16	12.29	2.42	3.17	2.98	N/A	238	52	53.4 [c]
Liang	3.17	12.18	2.45	3.24	2.85	-21.67	269	50	42.41
Stewart	3.17	12.17	2.44	3.24	2.85	-21.58	255.32	36.62	32.16
this work	3.11	12.03	2.39	3.15	2.87	-17.9	242.88	50.58	41.91

[a] reference [161], [b] reference [162].

In Table 5.2, the value of structural and energetic indicators calculated from the parameterization of Liang [95], Stewart [96], and this work are listed and compared to DFT and available experimental results. Although the structural indicators are similar, the

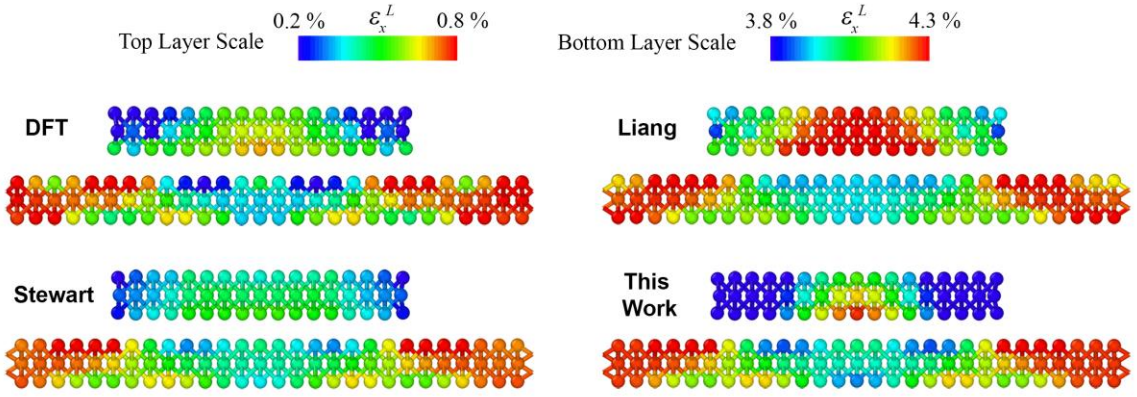

Figure 5.2 Comparison of Liang's, Stewart's, and our parameterization of Mo-S interatomic potential with DFT results: local strain map of a bilayer MoS_2 system under an applied uniaxial strain of 4%.

cohesive energy of MoS_2 molecular is remarkably improved by 23.54% (23.0%) as compared to Liang's (Stewart's) parameters.

The final and essential criterion of the optimization of the potential in this work is to reproduce the DFT-predicted strain configuration of CVD-grown bilayer MoS_2 structure with free edges as used in chapter 3 and chapter 4 [151]. The local strain maps [151] under an applied uniaxial strain of ε_x=4 % as computed using DFT and MD simulations with different sets of parameters are shown in Figure 5.2. The strain configuration of the bottom layer and top layer are distinct, which is indicated by the different scale for the two layers. The strain in the bottom layer is comparable to the applied strain (4%), while the strain in the top layer are significantly reduced to ~0.5% due to the presence of edges. All the three potentials are capable to predict a relatively accurate strain configuration of the bottom layer. However, Liang's (Stewart's) parameters overestimate (underestimate) the residual strain of the top layer. For example, for the Mo atom in the center of the top layer, DFT, Liang's, Stewart's, and our parameters predict the local strain at the value of 0.64%, 0.83%, 0.46% and 0.57%. As a result, our parametrization will be used in this work for the interatomic potential of Mo-S system.

5.3 Strain Response of Stacked MoS_2 Bilayer on Arbitrary Substrate

5.3.1 Model of Triangular MoS_2 Bilayer on Substrate

CVD-grown MoS_2 triangular flakes comprise of few layers wherein the top layers are smaller triangles with a rotation angle of 180^0 as compared to the bottom ones. During the strain loading process, the sample are attached to the substrate and the strain are directly

subjected to the substrate. To model such a system, a substrate layer with a rectangular shape is included. For simplification, we use single layer MoS_2 as a substrate in this section.

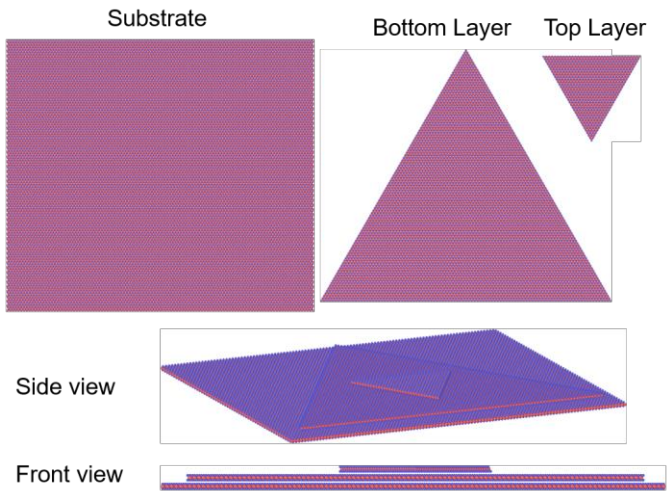

Figure 5.3 The structure of triangular MoS_2 bilayer with a substrate. Top row: the top view of substrate, bottom layer and top layer; middle row: side view; bottom row: front view.

The bilayer triangular system with a rectangular substrate is presented in Figure 5.3. *2H* stacking sequence is used in all the three layers. The substrate layer is a rectangle in the basal plane with the dimension of 34.8 nm × 30.7 nm. The bottom layer and top layer are both equilateral triangles with a side length of 31.1 nm and 10.3 nm, respectively. The center of top layer is right above that of the bottom, and the top layer rotates 180^0 with respect to the bottom layer. A vacuum space of 10 nm thick is used along the vertical direction of the system to prevent unphysical interactions between adjacent images along this direction. This model provides realistic edge configuration as observed in the CVD-grown MoS_2, and allows the investigation of the strain response of the triangular shaped flakes with substantial amount of edge.

5.3.2 Strain Response under Biaxial Tension

As discussed before, it is assumed that the strain is directly subjected to the substrate layer. As a result, the forces on the atoms in the substrate are rescaled to zero at each time step, so that the atoms are prohibited to move and the strain in the substrate atoms is exactly identical to the applied strain. The strain response is investigated under the loading condition of biaxial tensile strain ($\varepsilon_x \neq 0$, $\varepsilon_y \neq 0$, $\sigma_x \neq 0$, and $\sigma_y \neq 0$). The biaxial tensile strain is applied along the X and Y direction in increments of 0.1 % and the system is allowed to relax to minimize the total energy of the system at each increment. The straining is continued to reach a total tensile strain of 15 % which is within the elastic region [154] for the MoS_2 system using the REBO potential. At each increment, a layer strain along X and Y direction ($\varepsilon_x^{L_i}$ and $\varepsilon_y^{L_i}$) is calculated for each individual layer as

$$\varepsilon_x^{L_i} = \frac{x_i - x_{i0}}{x_{i0}} \ , \ \varepsilon_y^{L_i} = \frac{y_i - y_{i0}}{y_{i0}} \tag{5.4}$$

where i is the layer-id (1, 2; 1 corresponds to bottom layer and2is top layer); x_i (y_i) and x_{i0} (y_{i0}) are final and initial layer length of i^{th} layer in X (Y) direction, respectively. The analysis of the layer strain provides the strains of each individual layer and enables the investigation of the relaxation of each layer in each direction during the straining process.

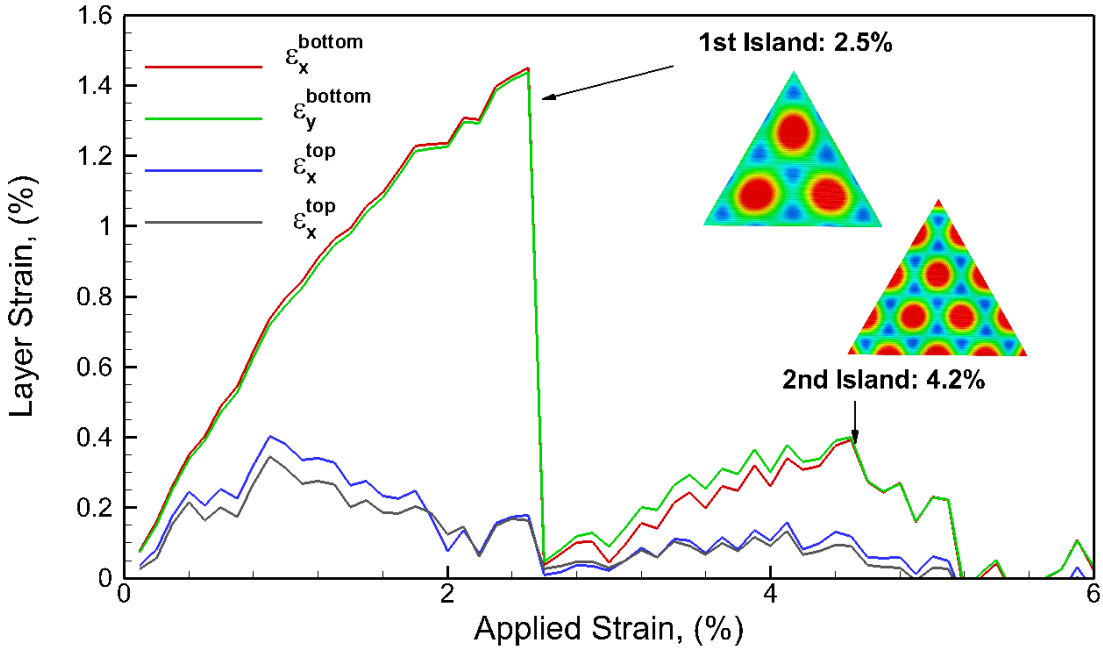

Figure 5.4 Local layer strains as a function of applied tensile strain ε show the emergence and nucleation of Moiré island under biaxial tensile strain.

The variations of $\varepsilon_x^{L_i}$ and $\varepsilon_y^{L_i}$ are plotted as a function of the applied biaxial tensile strain (ε_{xy}) for each individual layer, i.e., bottom layer and top layer, in Figure 5.4.

The layer strain in X and Y direction are almost the same for both bottom and top layer, which indicates the strain relaxation is direction-independent. It can be seen that the layer strain in the bottom layer and the top layer both present a periodical fluctuation every ~3.5% applied strain. At a small the applied strain, both the top layer and bottom layer show a linear increase with ε_{xy}. It should be pointed out that the strain subjected to the substrate is not completely transferred to the bilayered MoS_2 triangles. For example, the layer strain in the bottom layer is $\varepsilon_x^{L_1}$=0.8% at the applied strain ε_{xy}=1%. As a result, the layer strain in the bottom layer shows about 20% relaxation at this stage. The top layer

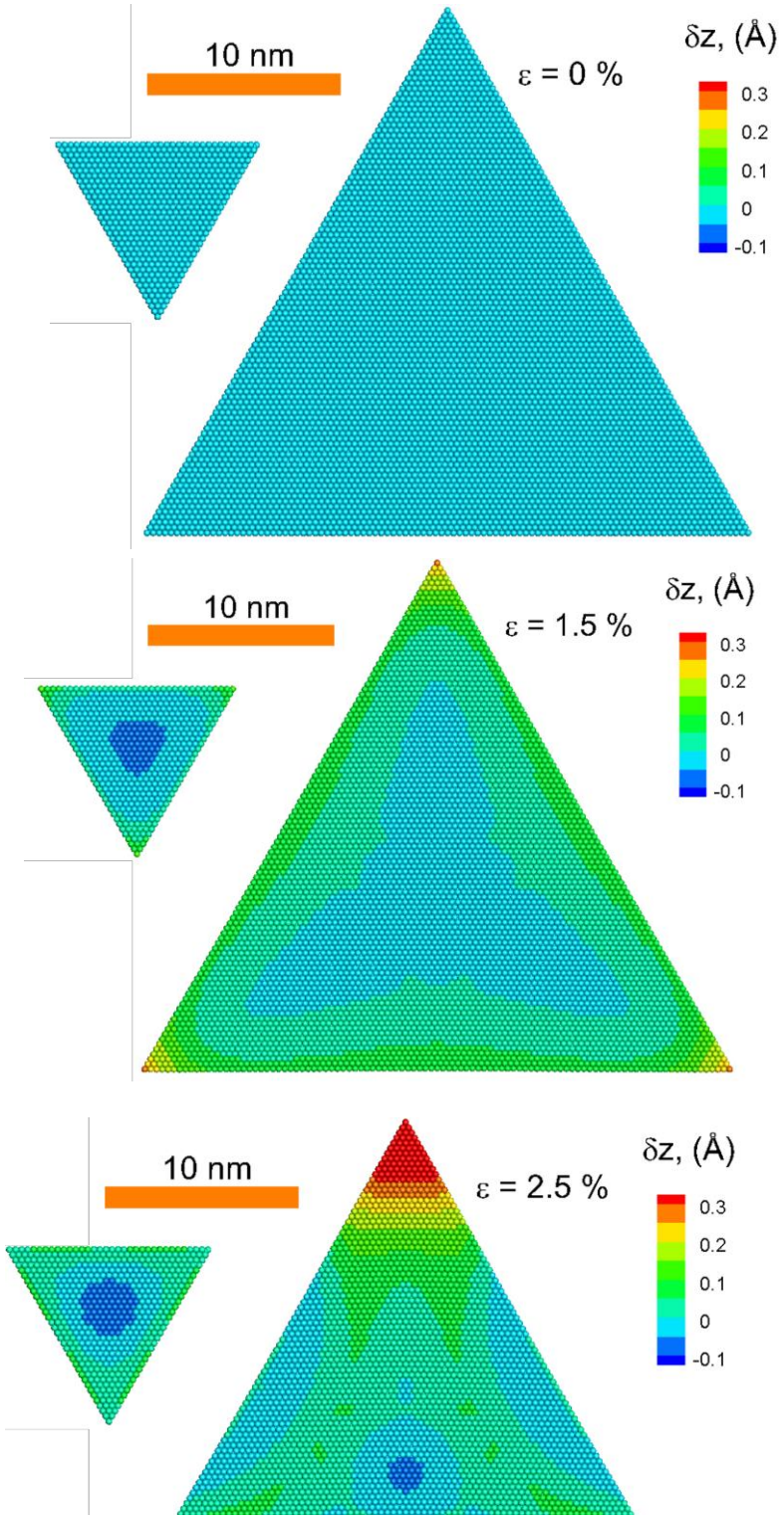

Figure 5.5 The vertical displacement map in the top layer and bottom layer at different applied biaxial tensile strain: (a) 0%, (b) 1.5%, (c) 2.5%.

presents more noticeable relaxation. Such an incomplete strain transfer between substrate

and the MoS_2 bilayer is supposed to create a lattice mismatch, and it is reasonably speculated that the Moiré pattern will be produced due to such a lattice mismatch. The layer strain continues to increase with applied strain for each layer up to a certain value, after which a further increase in applied strain results in a drop in the local strain. Then the layer strain periodically rises and drop every ~3% applied strain. Each increase in the strain is followed by a small reduction in layer strain when strained further. Such increases and decreases in the applied strains are observed to occur simultaneously for bottom layer and top layer as the applied strain increases. The layer strain in the bottom layer is consistently higher than that in the top layer, suggesting a larger relaxation in the top layer due to the presence of a free surface above the top layer. However, it is not clear if these simultaneous variations are related to the sliding between the layers or due to the presence of Moiré patterns.

To investigate the strain relaxation mechanisms of the various layer strains, an out-of-plane vertical displacement is computed for each atom along the length of layers in the bilayered structure. This vertical displacement (δz_i), at a certain atom *i*, is computed as $\delta z_i = z_i - z_{0i}$, where z_i and z_{0i} are the instantaneous and initial Z-coordinate of atom *i*, respectively. The vertical displacement will be expected to be uniform for the case of sliding between the layers as the strain relaxation mechanism. For the case of the emergence of Moiré pattern, a vertical displacement profile will show high displacements at the edges of the top layer and bottom layer. The map of δz_i are shown in Figure 5.5 to visualize the local variations in vertical displacements at different applied strain at the atomic scale. The atoms are colored by the displacement in the Z direction with the positive

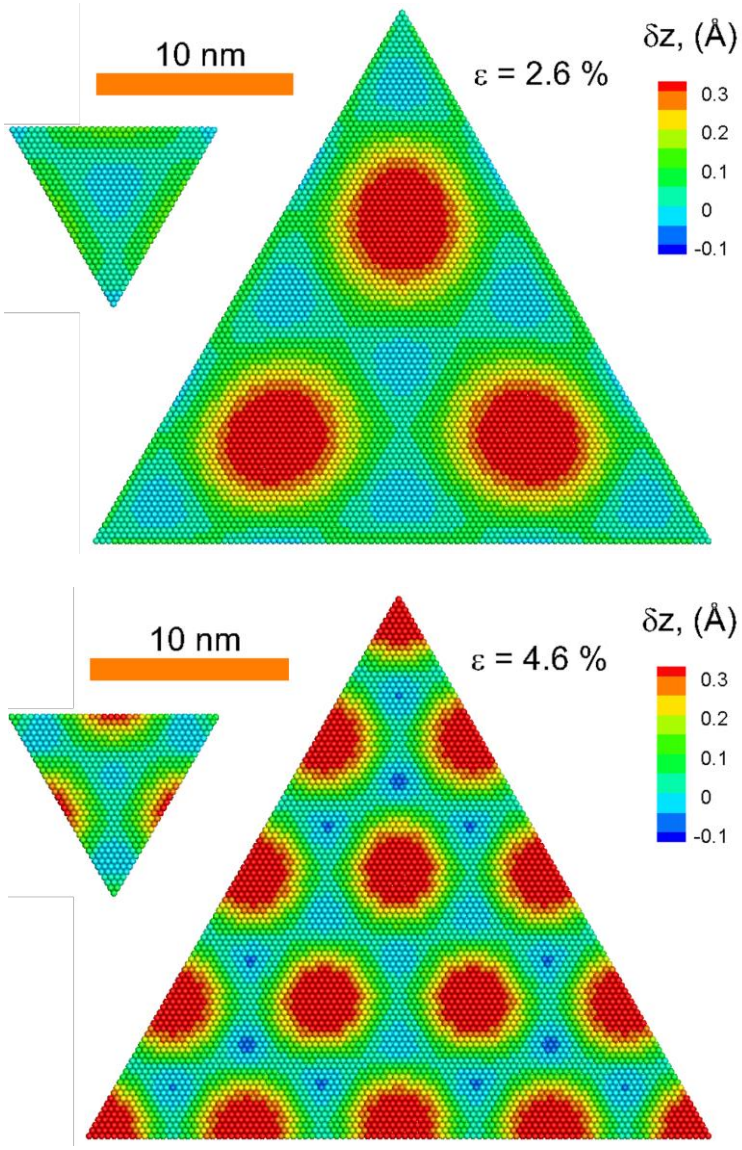

Figure 5.6 The vertical displacement map shows the nucleation of displacement islands and the formation of Moiré pattern in the top layer and bottom layer at different applied biaxial tensile strain: (a) 2.6%, (b) 4.6%.

value (red color) corresponding to an upward displacement and a negative value (blue color) indicating a downward displacement as compared to the unstrained configuration. At strain-free configuration (ε_{xy} = 0%), there is no displacement along vertical direction for all atoms. Therefore, δz_i of all the atoms equals to zero and these atoms are colored in light

blue, as shown in Figure 5.5 (a). As shown in Figure 5.5(b), at an applied strain of ε_{xy} = 1.5 % the atoms in the corner of bottom layer triangle are displaced upwards (yellow/orange) and the atoms in the center are gradually displaced downwards (dark blue). The maximal upward and downward displacement are computed to be 0.28 Å and -0.03 Å. The downward displacement of the top layer is -0.053 Å, which is larger than that in the bottom. The corner of the top layer is also displaced upward as much as 0.087 Å. It is interesting to mention that the downward displacement pattern found at ε_{xy} = 1.5 % is incredibly similar to the PL intensity map of stacked bilayered triangular system under a strain, where the PL intensity of bottom layer is low at the center and increases with a sharp tail towards the corner (a shape of three-pointed star), while the PL intensity of top layer is noticeably low at the center as compared to the bottom layer and slightly high at the edge [150]. The comparable results further suggest that the current interatomic potential is capable to capture the strain response of the bilayer system. As strained further to ε_{xy} = 2.5 % (Figure 5.5(c)), the bottom layer shows more upward displacement at the corner with an enhanced magnitude to 0.39 Å, and the tail of the "three-pointed star" turns to be broad. It is noticed that the edges of the bottom layer present a downward displacement around -0.024 Å. Besides, the downward displacement of the center in bottom layer also increases, with a maximum of -0.056 Å.

At applied strain of ε_{xy} = 2.6 % (Figure 5.6(a)), where the layer strain undergoes a substantial reduction as shown in Figure 5.4, the downward displacements at the corner shift to the center and form three displacement island. The dramatic decrease in the layer strain is attributed to the emergence of such Moiré-like patterns. The maximal upward

displacement in the center of the Moiré island is observed to be 0.42 Å, which is comparable to those observed in MoS_2-WS_2 (0.51 Å) or MoS_2-WSe_2 (0.39 Å) heterostructures [158] from continuum simulations. The periodicity of the Moiré pattern is 13.09 nm as computed from the distance of two Moiré island, which is slightly larger than that in MoS_2-WS_2 bilayer, ~ 8.7 nm, and lower than that in MoS_2-Au (111) interface, ~30 nm [74-77, 159]. No Moiré pattern is observed in the top layer at the current applied strain. However, it should be noticed that the edges of the top layer undergo a recognizably large upward displacement, 0.13 Å as indicated by the noticeable green color on the edges. Meanwhile, the downward displacement in the center of the top layer slightly decreases to -0.037 Å as compared to -0.056 Å at $\varepsilon_{xy} = 2.5$ %.

Table 5.3 The maximal upward displacement, $\delta z_{\max}^{up}$, downward displacement, $\delta z_{\max}^{down}$, and periodicity of Moiré pattern, Δ_{rep} during the tension.

	Bottom Layer			Top Layer		
ε_{xy}	$\delta z_{\max}^{up}$	$\delta z_{\max}^{down}$	Δ_{rep}	$\delta z_{\max}^{up}$	$\delta z_{\max}^{down}$	Δ_{rep}
1.5%	0.28	-0.032	N/A	0.087	-0.053	N/A
2.5%	0.39	-0.024	N/A	0.064	-0.072	N/A
2.6%	0.42	-0.036	13.09	0.13	-0.037	N/A
4.6%	0.41	-0.058	7.65	0.31	-0.034	N/A

As shown in Figure 5.6(b), further straining of the structure to $\varepsilon_{xy} = 4.6$ %, where the layer strain of the bottom layer reduces for the second time, results in emergence of additional set of Moiré island at the edges, and the old Moiré islands are pushed towards the center. The correlation between the formation of Moiré islands and the reduction in layer strain is reconfirmed. The maximal displacement of the new Moiré island is 0.41 Å, which is almost the same as those nucleated at an applied strain of $\varepsilon_{xy} = 2.5$ %. The downwards displacement shows a maximal amplitude of -0.053 Å. With the emergence of additional islands, the repeated distance is reduced to 7.65 nm. The edges of top layer are continued to push upward, and a set of Moiré islands are clearly being generated.

5.4 Strain Response under Biaxial Compression

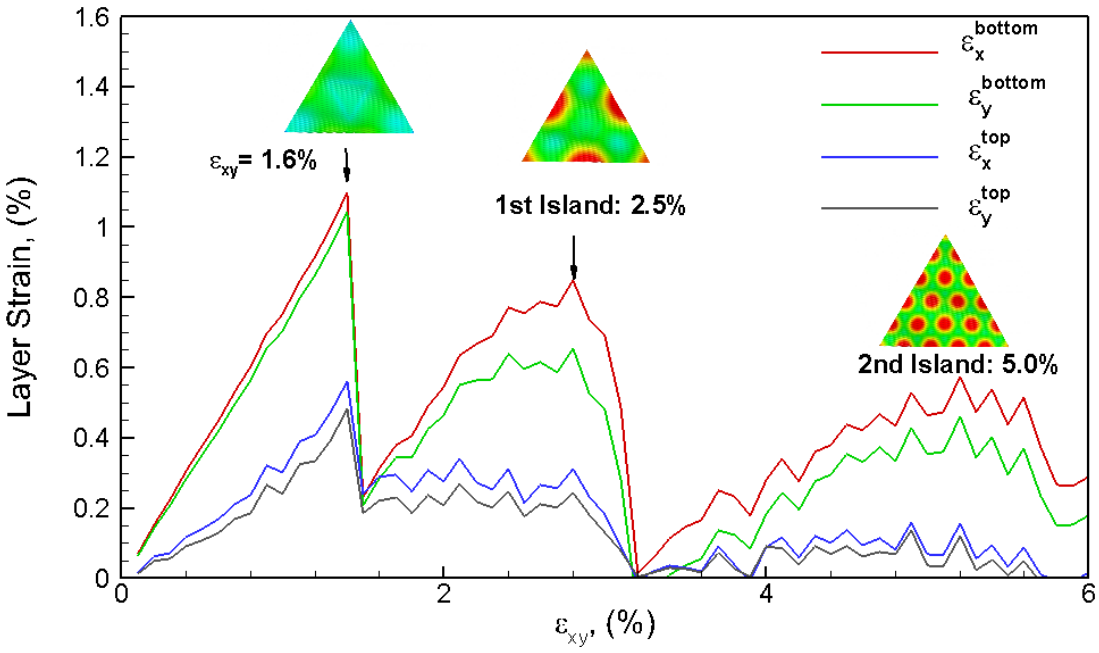

Figure 5.7 Local layer strain as a function of applied strain show the emergence and nucleation of Moiré island under biaxial compressive strain.

The biaxial compressive strain is also applied to the triangular MoS_2 bilayer with a monolayer MoS_2 substrate to understand the strain response under the condition of compression. The variation of layer strain ($\varepsilon_x^{L_i}$) for each individual layer (bottom and top) in bilayered structure as a function of applied biaxial compressive strain (ε_x) is shown in Figure 5.7, and the vertical displacement map of bottom layer and top layer at different applied strain are presented in Figure 5.9.

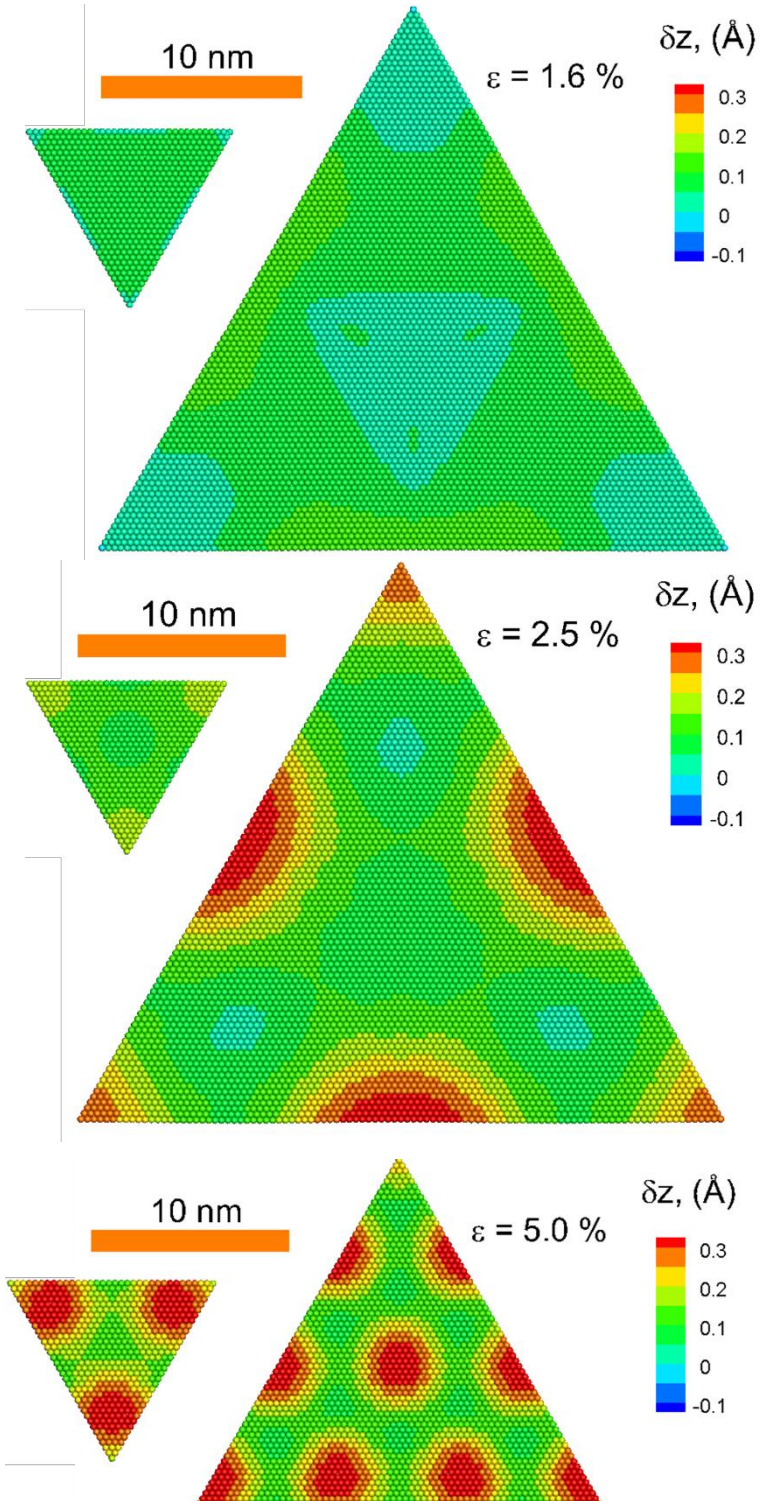

Figure 5.8 The vertical displacement map shows the nucleation of displacement islands and the formation of Moiré pattern in the top layer and bottom layer at different applied biaxial compressive strain: (a) 1.6 %, (b) 2.5 %, (c) 5.0 %.

Similar to the case of tension, the layer strains in the bottom layer and top layer present simultaneous fluctuation with a periodicity of 2.5%. Each reduction in layer strain corresponds to the nucleation of new group of Moiré islands. However, the application of compressive strain also exhibits some noticeable differences as compared to tension. At first, the strain is first observed to be substantially relaxed at the applied strain of 1.6% through extensive upwards displacement (green) at the edges. Such a relaxation is not seen during the tension. Secondly, at an applied strain of $\varepsilon_{xy} = 2.5$ %, six displacement islands, instead of three in the case of tension, emerge at the edges of the bottom layer (Figure 5.9(b)), which results in the reduction of layer strain in both top layer and bottom layer. Meanwhile, the corners of top layer show upwards displacement with a maximal magnitude of 0.19 Å. In addition, unlike tension, no downwards displacement is seen during the compression, which is shown in Table 5.4. The Moiré islands are distinct from the atoms in adjacent region by presenting larger upwards displacement.

Table 5.4 The maximal upward displacement, $\delta z^{up}_{\max}$, minimal upward displacement, δz^{up}_{min}, and periodicity of Moiré pattern, Δ_{rep} during the compression.

	Bottom Layer			Top Layer		
ε_{xy}	$\delta z^{up}_{\max}$	δz^{up}_{min}	Δ_{rep}	$\delta z^{up}_{\max}$	δz^{up}_{min}	Δ_{rep}
1.6 %	0.14	0.02	N/A	0.072	0.048	N/A
2.5 %	0.35	0.038	17.92	0.19	0.087	N/A
5 %	0.35	0.074	6.82	0.34	0.12	6.21

5.4 Conclusions

Molecular dynamics simulations are carried out to investigate the strain response of CVD-grown MoS_2 structures at the atomic scales. The interatomic interactions between Mo/S atoms are optimized in the form of hybrid REBO/LJ potential to best capture the structural and energetic properties, as well as the strain configuration at the presence of edges. A bilayer MoS_2 triangles over a MoS_2 substrate layer is created to model CVD-grown structure with realistic edge configurations. The MD simulations suggest that the strain subjected to the substrate is not able to completely transferred to the bilayered MoS_2 sample, and the difference in the layer strain causes lattice match, which results in the formation of Moiré pattern. The emergence of Moiré islands is correlated to the reduction in the layer strain. A new group of Moiré islands are nucleated every 3.2 % applied strain in tension and 2.5 % in compression, which results in a periodic reduction in the layer strain. Besides, the strain response at an applied tensile strain of 1.5% shows a "three-pointed star" shape in displacement map, which is astonishingly similar to the PL intensity map of the bilayer MoS_2 triangle found in recent experiments.

CHAPTER SIX

6. STRAIN EFFECTS ON OTHER 2D TMDS

6.1 Introduction

As discussed in the introduction, the possibility of fabricating multilayer van der Waals heterostructure opens up new opportunities for building "Legos" with atomic thin TMDs for a wide range of applications. [48, 163, 164] These stacked vdW solids offer great tunability and provide new functionality compared with conventional devices. [165] However, as summarized in a recent review [165], integration with other materials and controlling the resulting interfaces would be a challenge for technologically relevant applications. In this chapter, we will expand the study of strain effects to other 2D TMDs and vdW solids built from these materials, such as HfS_2, WSe_2.

HfS_2 is a good candidate for realizing ultra-low power circuits thanks to its well-balanced mobility (1800 $cm^2/V{\cdot}S$) and bandgap (1.2 eV) in 2D structures [166]. The FETs based on few-layer HfS_2 are recently reported and present large on-off ratio and high drain current [166, 167]. WSe_2 is known for a giant split at the valley in the valance band due to spin-orbit coupling, which may be implemented in the spintronic devices. [168, 169] Recently, the single-photon emission has been discovered in monolayer WSe_2, which is interesting for the applications of quantum optics. [170, 171] It has been speculated that such localized emitters in monolayer WSe_2 is likely to be attributed to the strain. [172, 173]

Therefore, the strain effects on the electronic and optical properties of HfS_2, WSe_2 are discussed in this chapter, and the heterostructures built from MoS_2, HfS_2 and WSe_2 will be investigated in the future.

6.2 Simulation Details and Electronic Properties

DFT calculations are carried out using projector augmented wave pseudo-potentials [137] as implemented in the VASP code. [138] The cutoff energy is 550 eV for the plane-wave expansions and the Monkhorst–Pack *k*-point mesh is 17×17×17 for bulk and 17×17×1. The exchange-correlation functional is treated within the Perdew–Burke–Ernzerhof (PBE) generalized gradient approximations (GGA). [139] To study the effects of interlayer coupling, the conventional DFT energy is supplemented with a pairwise interatomic vdW potential which is determined by Tkatchenko and Scheffler (TS-vdW) from non-empirical mean-field electronic structure calculations. [113] The atomic positions of a unit cell are optimized until all components of the forces on each atom are reduced to values below 0.01 eV/Å.

The lattice constants and elastic properties of HfS_2 and WSe_2 are shown in Table 6.1 and Table 6.2, respectively. Our calculations are compared with experiments and previous calculations. The simulations without supplemented vdW interaction is noted as PBE, and PBE-TS denotes the simulations with supplemented vdW coupling. PBE-DF and PBE-D are previous calculations with different supplemented vdW interactions. It is clearly shown that without supplemented vdW potential, PBE is not able to accurately predict the lattice spacing in the vertical direction (*c* lattice parameter), although the in-plane lattice constant *a* is not affected. Without TS potential, the *c* parameter in HfS_2 and

WSe_2 are overestimated by 14.7% and 15.3%, respectively. When a supplemented vdW potential is considered, the out-of-plane spacing is well predicted to the second decimal. On the other hand, the elastic constants are underestimated without TS vdW interaction, especially for the C_{33} and C_{13}, which are related to the vertical direction. For example, C33 of WSe_2 is 12.2 GPa from PBE simulation, which is significantly deviated from the value from the experiment, 50 GPa. It is not surprising that the cohesive energies are similar for PBE and PBE-TS results because the out-of-plane vdW is much weaker as compared to the in-plane covalent bonds. As a result, the PBE-TS simulations are used for HfS_2 and WSe_2 in this chapter.

Table 6.1. The lattice constants and elastic properties of bulk HfS_2 from DFT, experiments and MD calculation with different parameterization.

	a (Å)	c (Å)	E_{coh} (eV)	C_{11} (GPa)	C_{33} (GPa)	C_{12} (GPa)	C_{13} (GPa)	C_{44} (GPa)	B_0 (GPa)
PBE	3.64	6.70	-22.93	125.23	6.61	18.38	2.03	53.42	6.33
PBE-TS	3.62	5.86	-23.73	137.07	36.73	15.24	6.83	60.91	27.72
exp. [a]	3.63	5.84							
PBE-TS [b]	3.61	5.84		141.98	32.99	25.95	6.53	58.01	35.07
PBE-DF [b]	3.77	6.31							
exp. [c]	3.63	5.85							

[a] reference [174], [b] reference [175], [c] reference [176].

Table 6.2. The lattice constants and elastic properties of bulk WSe_2 from DFT, experiments and MD calculation with different parameterization.

	a (Å)	c (Å)	E_{coh} (eV)	C_{11} (GPa)	C_{33} (GPa)	C_{12} (GPa)	C_{13} (GPa)	C_{44} (GPa)	B_0 (GPa)
PBE	3.32	14.95	-21.63	161.17	12.20	34.01	6.97	63.58	11.91
PBE-TS	3.30	12.99	-21.57	200.57	61.95	37.82	17.93	81.38	48.61
exp. [a]	3.28	12.96			52.1				
PBE-DF [b]	3.28	13.014			57.3				
exp. [c]				200	50				
MD [d]	3.39	12.92		193.7	50.1	81.9	16.3	9.1	58.4
PBE-D [e]	3.30	13.092		190.76	59.62	41.71	21.18	39.26	63.7

[a] reference [177, 178] , [b] reference [179], [c] reference [180], [d] reference [181], [e] reference [182].

The band structure of monolayer (ML), bilayer (BL) and trilayer (TL) HfS2 are considered in this section to study the effect of layer thickness on the electronic properties of HfS_2. The band structures are shown in Figure 6.1. The band transitions from valence band maximum (VBM) to conduction band minimum (CBM) are indicated by the dashed arrows. It is an indirect band transition for ML HfS_2, and the VBM and CBM locate at Γ and M, respectively, which is different from the direct transition (K to K) in the case of monolayer MoS_2. Such a difference is contributed to the contrasting *1T* structure in HfS_2 as compared to the *2H* structure in MoS_2. These band edges are not changed as the layer thickness increases. The band gap energy decreases as the layer thickness increases. There

is a noticeable decrease from monolayer (1.32 eV) to bilayer (1.2 eV), and a less pronounced decrease from BL to TL (1.17 eV).

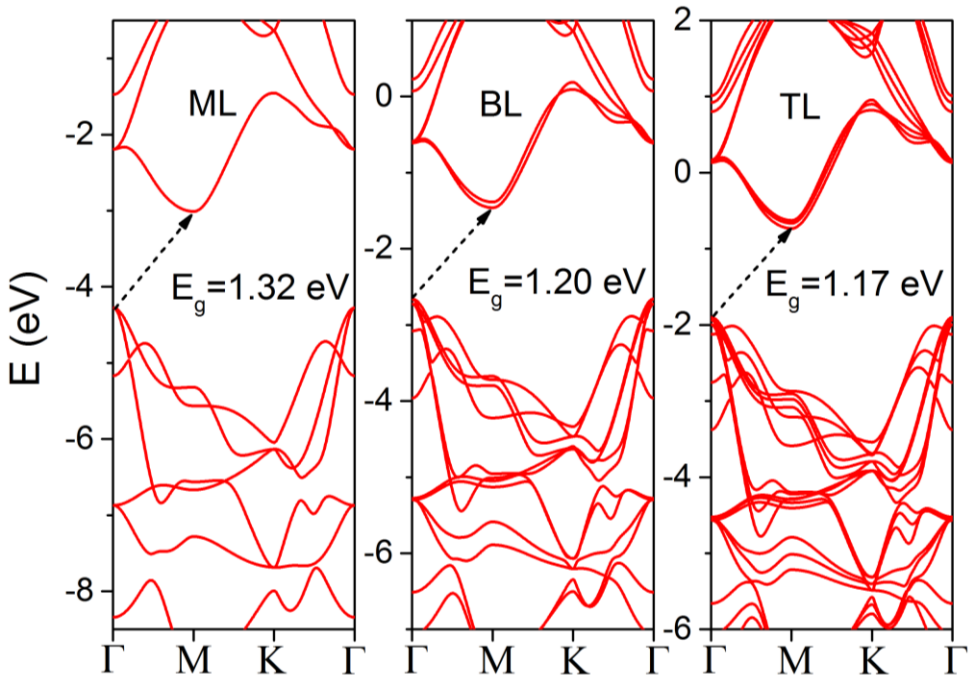

Figure 6.1 The band structures of monolayer, bilayer and trilayer HfS_2. The band transitions from VBM to CBM are indicated by the black dashed arrows.

As discussed in the introduction, the spin-orbit coupling (SOC) plays a vital role on electronic and optical properties of WSe_2. Due to the inversion-asymmetry of the 2D TMDs, the SOC results in the two non-degenerate valance bands, i.e. band splitting, and the spin projection is well defined as spin up and spin down. [169] It has been reported that the spin splitting of the valence band may reach around ~140 meV for MoS_2 and ~450 meV for WSe_2. [31, 183, 184] Therefore, the effect of SOC on the bandstructure of BL WSe_2 is first studied.

In Figure 6.2, the band structure from PBE suggests a direct K–K band transition. The conduction band edge appears at K_C of the Brillouin zone, whose energy is slightly

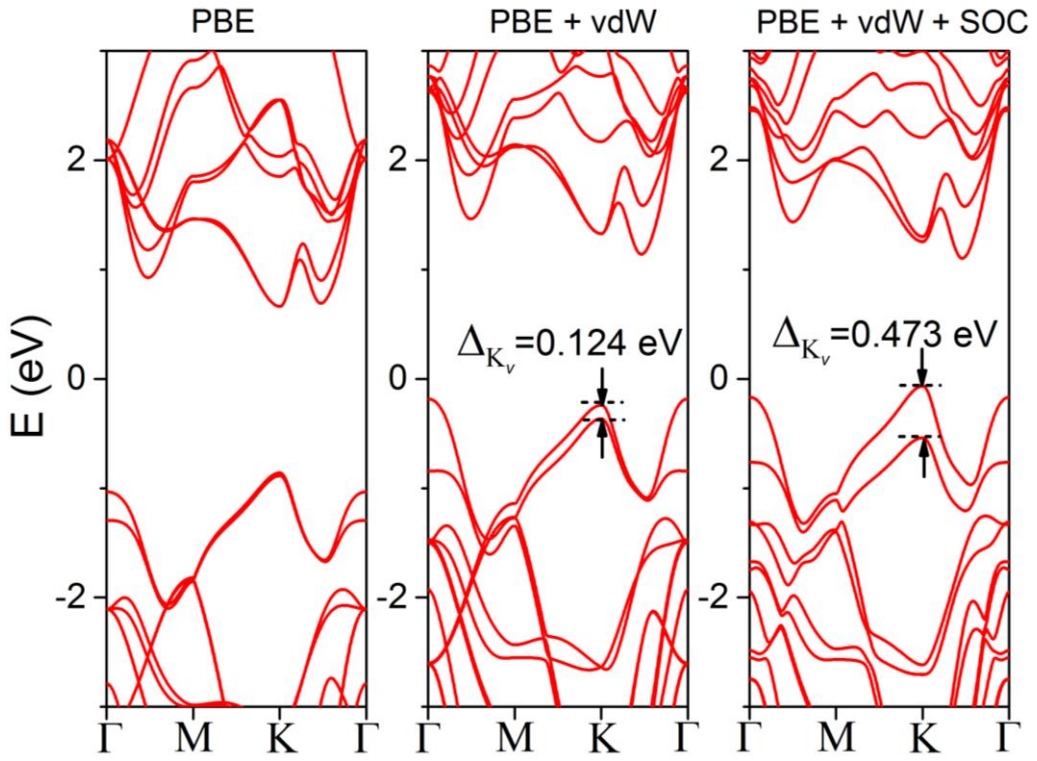

Figure 6.2 The band structures of bilayer WSe_2 using different computational methods: PBE, PBE with TS supplemented vdW interaction (PBE + vdW), and PBE with TS potential with spin orbit coupling (PBE + vdW + SOC).

lower than that of Σ_C. The valence band shows no splitting at K_V. At the case of PBE + vdW, the band splitting at Σ_C is so giant that the energy of Σ_C becomes lower than K_C. As a result, the CBM changed to Σ_C from Kc. At the valence side, the band splitting at Γ_V shows large enough that the energy of Γ_V surpasses K_V. The VBM locates at Γ_V instead of K_V. The band transition from PBE + vdW is predicted as Γ–Σ. A visible band splitting is observed at K_V, denoted as Δ_{K_v}=0.124 eV. When the SOC is considered, the most noticeable difference is the valence band splitting at K_V. The Δ_{K_v} is observed to increase to 0.473 eV. Such a giant spin splitting is originated from the loss of the inversion symmetry from bulk to 2D structures, and the $d_{x2-y2} + d_{xy}$ states of W atoms are responsible

for the splitting. [183] The VBM appears at K_V point of the Brillouin zone, while CBM still locates at Σ_C, resulting in an indirect K–Σ transition. Our results from PBE, PBE + vdW and PBE + vdW + SOC show that the bandstructure of bilayer WSe_2 is sensitive to the SOC. The band nature such as the band edges and band splitting is largely dependent on the supplemented vdW and SOC. Therefore, the SOC and vdW are supposed to be considered in the straining studies of bilayer WSe_2 in this section.

6.3 Strain Response of 2D HfS_2

The band structure of ML HfS_2 under biaxial strain is shown in Figure 6.3 for various strains. It is evident that the band edge is not altered under strain, and it remains an indirect Γ–M transition under the applied biaxial strain. The energy of CBM remains almost constant at ~-3eV under strain, while the energy of VBM remarkably increases with the applied strain, leading to a crossover of VBM and CBM after a certain strain. It is clearly shown at 15% compressive strain, the VBM stays above CBM, indicating a metallic nature of the band structure. The reason for the distinct behaviors of band edges under strain can be explained from the contributing orbitals. The major contributing orbital at VBM is S p_{x+y}, while Hf d_{z2} and S p_z are dominated at CBM. The in-plane strain has a predominate influence for the in-plane orbitals (S p_{x+y}), and the effects on vertical

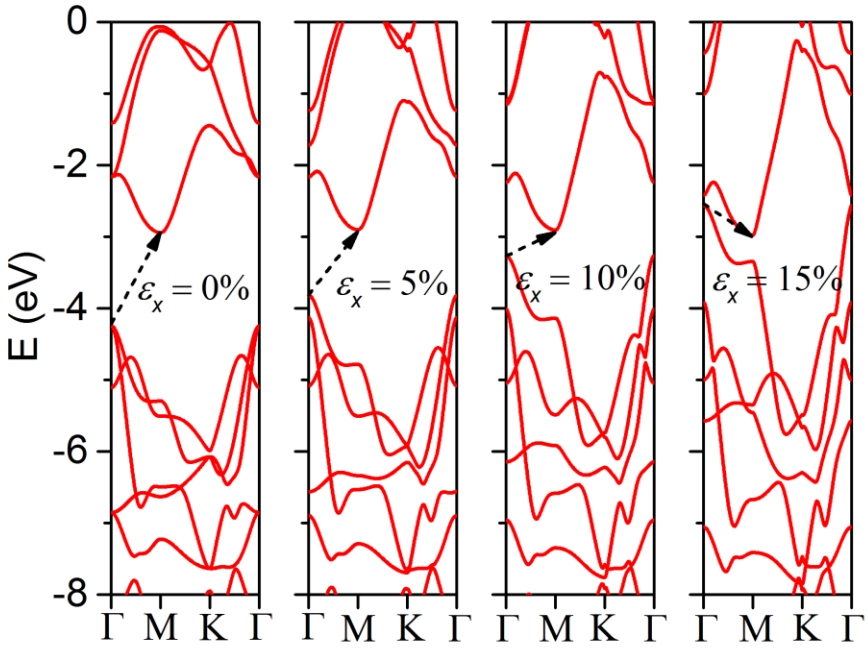

Figure 6.3 The band structures of monolayer HfS_2 under various biaxial compressive strains showing the metallization.

directions (Hf d_{z2} and S p_z) are negligible. As a result, the energy of VBM is dramatically altered while the CBM stays unchanged under the applied in-plane strain.

It has been shown that there exists a semiconductor-metal transition in 2D TMDs under the external pressure [185-187]. For example, theoretical studies have predicted that the band gap of BL MoS_2 reduced to zero at a uniaxial tension of 20% and a biaxial tension of 5% [188, 189]. It remains unknown that whether a metallization of 2D HfS_2 may occur under the applied strain. Therefore, uniaxial strain and biaxial strain are applied to ML, BL, TL HfS_2 system. The applied strain ranges from -15% (compression) to 10% to probe the limit of the metallization. As shown in Figure 6.4, for all the cases, the band gap energy increases with tensile strains and decreases with compressive strains unlike MoS_2, where a converse trend is observed. The metallization of 2D HfS_2 is observed at the compressive domain. Another difference in HfS_2 is that the mechanical boundary condition (MBC) has

a negligible effect on the metallization as compared to MoS_2. For example, BL HfS_2 changed to metal at a compressive strain of 11.2% under uniaxial MBC and 10% under biaxial MBC, while for MoS_2 the metallization occurs at a tensile strain of 20% under uniaxial MBC and 5% under biaxial MBC. The metallization strain is observed to be smaller as the layer thickness increases. In the tensile domain, the band gap energy almost linearly increases with strain at a small applied strain. After a certain strain, the band gap energy remains invariant with the further increasing strain, which suggests an upper limit for the band gap energy under a certain MBC.

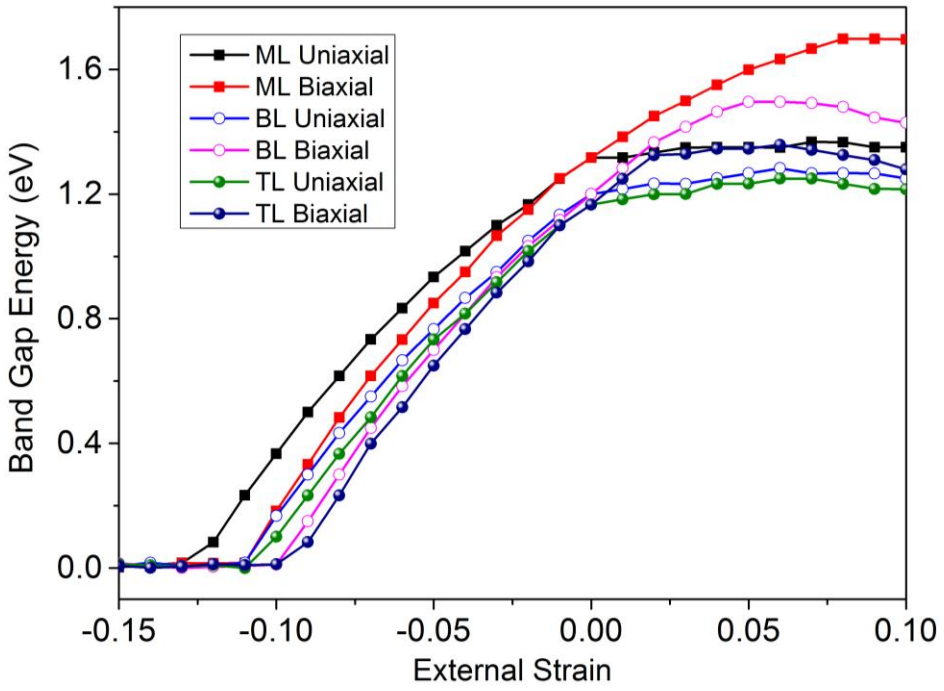

Figure 6.4 The band structures of monolayer, bilayer and trilayer HfS_2. The band transitions from VBM to CBM are indicated by the black dashed arrows.

6.4 Strain Effects on Bilayer WSe_2

The strain effects on bilayered WSe_2 is studied in this section. To study the strain effects on the band structure, a uniaxial strain is applied along the zigzag direction of bilayer WSe_2. The applied tensile strain ranges from 0% to 4% with an increment of 0.5%. The tensile strain subjected to the zigzag (*x*) direction is supposed to induce a compressive strain along armchair (*y*) direction due to the Poisson effect. It is necessary to consider the Poisson ratio when one wants to compare the theoretical predictions with the experimental values. The Poisson ratio of the PET substrate (0.4) is used as the strain is directly subjected to the substrate in experiments. That is to say, a compensate compressive strain of 0.4% is applied in the *y* direction for every 1% tensile strain subjected in the *x* direction. As a result, four different cases are considered: (a) PBE, (b) PBE with TS supplemented vdW potential (PBE + vdW), (c) PBE with TS potential with SOC (PBE + vdW + SOC), and (d) PBE + vdW + SOC with the consideration of the Poisson effect. The band structures of these four cases at various tensile strains are presented in Figure 6.5. In absence of SOC (Figure 6.5 (a) and (b)), no splitting of energy bands at the band edges are observed. The tensile strain downshifts the energies of electronic bands, and the effects are more noticeable with the vdW interaction (Figure 6.5 (a) and (b)), leading to a wider spread under strain. Also, the decreases in energies at K points (both K_C and K_V) are considerably dramatic as compared to the Γ_V points. In the case of PBE + vdW, the conduction band edge shifts from Σ point to K point under tensile strain. When the SOC is considered (Figure 6.5 (c) and (d)), a remarkable band splitting at K_V is observed for all the applied strain. The strain spread is reduced when the Poisson effects are included. It is easy to understand that the Poisson

effects can offset the increasing of the W-Se bond length under the tensile strain, and the strain effects are reduced.

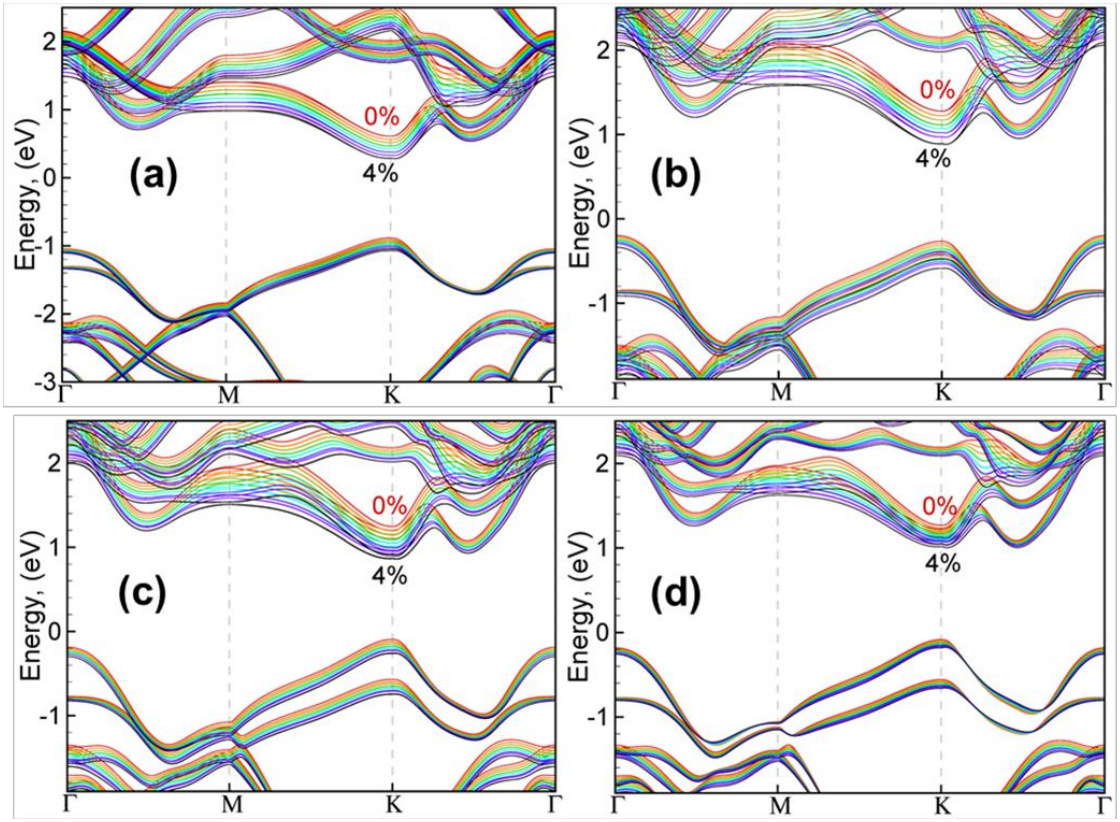

Figure 6.5 The band structures of bilayer WSe_2 at various uniaxial strains from 0% to 4% using different computational methods: (a) PBE, (b) PBE + vdW, (c) PBE + vdW + SOC, and (d) PBE + vdW + SOC + Poisson.

It can be seen from Figure 6.5 that four critical points are suggested from our calculations for the band transitions: Γ_V, K_V, K_C, Σ_C. As a result, the energy differences between these four points, i.e., Γ_V–K_C, K_V–K_C, Γ_V–Σ_C, and K_V–Σ_C are calculated to determine the variation in the band gap energy for the bilayer WSe_2 under uniaxial tensile strain. The band transitions for the for cases are shown in Figure 6.6. Only the energy gaps of K_V–Σ_C transition increase with the strain; the other three transitions show a reduction in energy gaps under the uniaxial tensile strain. The slope of Γ_V–K_C energy gap with respect

to the strain is largest among all the four transitions, followed by the direct K_V–K_C transition. The large slopes of these two transitions can be explained by the strong effect of strain in the band energy at K_C as indicated in Figure 6.5. The PBE result (Figure 6.6(a)) suggests an unphysical direct band transition even in a strained bilayer WeS_2. With the vdW interaction (Figure 6.6(b)), the indirect Γ_V–Σ_C transition is observed to be the lowest gap energy at small strain, and Γ_V–K_C appears lower at around 3% tensile strain. The involvement of SOC results in a giant band splitting at K_V, which remarkably decreases the gap energy of K_V–K_C. As a result, the gap energy of direct K_V–K_C transition is

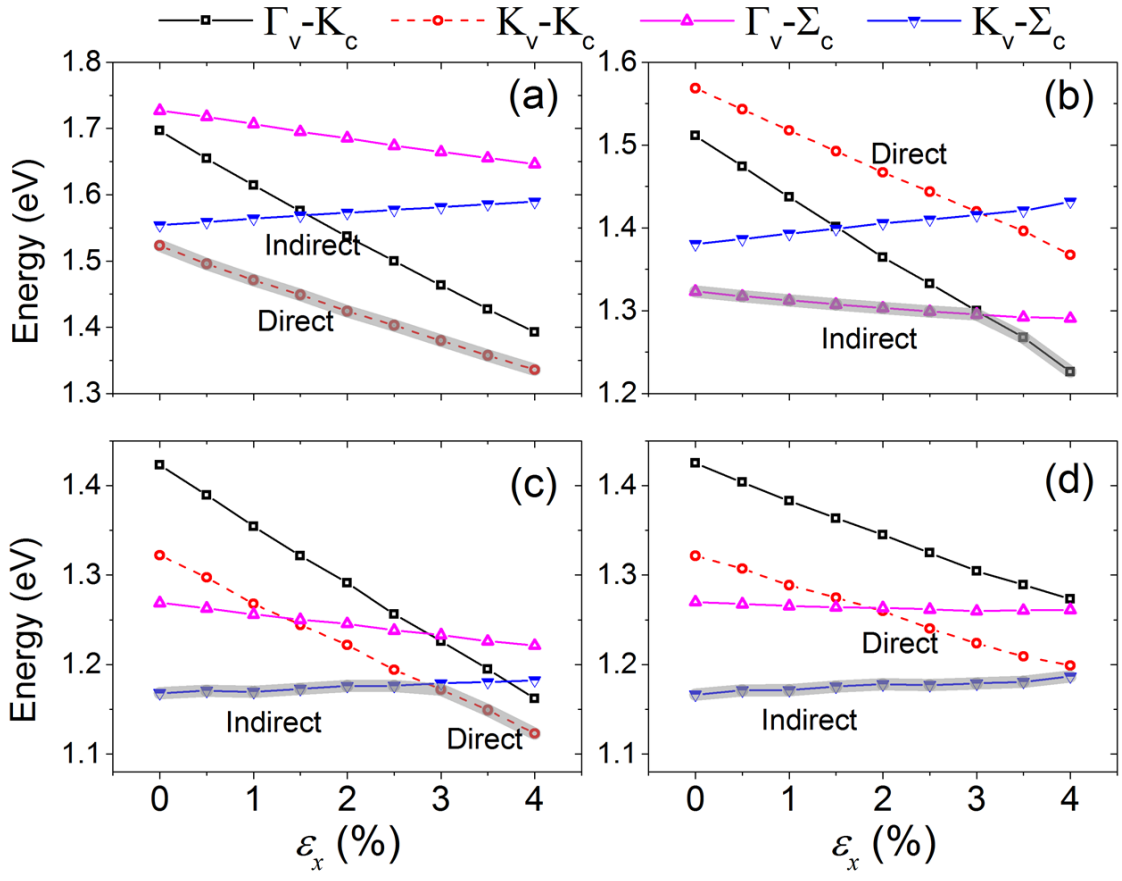

Figure 6.6 The band transitions of bilayer WSe_2 under uniaxial strains from 0% to 4% using different computational methods: (a) PBE, (b) PBE + vdW, (c) PBE + vdW + SOC, and (d) PBE + vdW + SOC + Poisson.

substantially lowered as compared to non-SOC case in Figure 6.6 (b). An interesting indirect-to-direct crossover in the band transition is observed at around 3% strain in Figure 6.6 (c). As discussed before, the inclusion of Poisson ratio reduces the strain effects, and the crossover is postponed as shown in Figure 6 (d). At 4% strain, the direct K_V–K_C transition is almost below the indirect Γ_V–K_C transition. According to the trends of these two transitions, it is obvious that the further strain is supposed to create a crossover.

Apart from the band gap energies, the effect of strain also modifies the curvature of the profiles at the band edges. These curvatures are directly related to the effective carrier mass of electrons and holes at CB and VB, respectively. The effective masses are defined as:

$$m_e = \hbar^2 \left(\frac{\partial^2 E_C}{\partial k^2} \right)^{-1}$$

and

$$m_h = \hbar^2 \left(\frac{\partial^2 E_V}{\partial k^2} \right)^{-1}$$

where $\hbar$ =1.05×10^{-34} kg·m^2/s, E_C (E_V) is the conduction (valence) band energy, and k is the wavevector in the reciprocal lattice. Similarly, four critical points are considered Γ_V, K_V, K_C, Σ_C. As a result, m_e at the K_C and Σ_C points of the conduction band ($m(e_K)$ and $m_e(e_\Sigma)$) as well as m_h at the K_V and Γ_V points of the valence band ($m(h_K)$ and $m(h_\Gamma)$) are calculated. Since electrons and holes accumulate primarily around CBM and VBM, respectively, the effective masses at CBM and VBM are more important than those at other points of the band structure. As shown in Figure 7, the effective mass at Γ_V point is

noticeably larger than the other three points, suggesting the carrier concentration at the Γ_V be much higher. With the applied tensile strain, $m(h_\Gamma)$ shows decreasing trend and $m_e(e_\Sigma)$ shows increasing. The mobilities of charge carriers at K points are mainly related to W d_{z2} electrons, which is negligibly affected by the in-plane strain. [190] As a result, the effective mass at K points are almost invariant with respect to tensile strain, as shown in Figure 6.7. As for the different methods, the PBE (Figure 7(a)) shows a significantly larger effective mass, especially at Γ_V point; the other three methods predict similar trend and values for the effective masses.

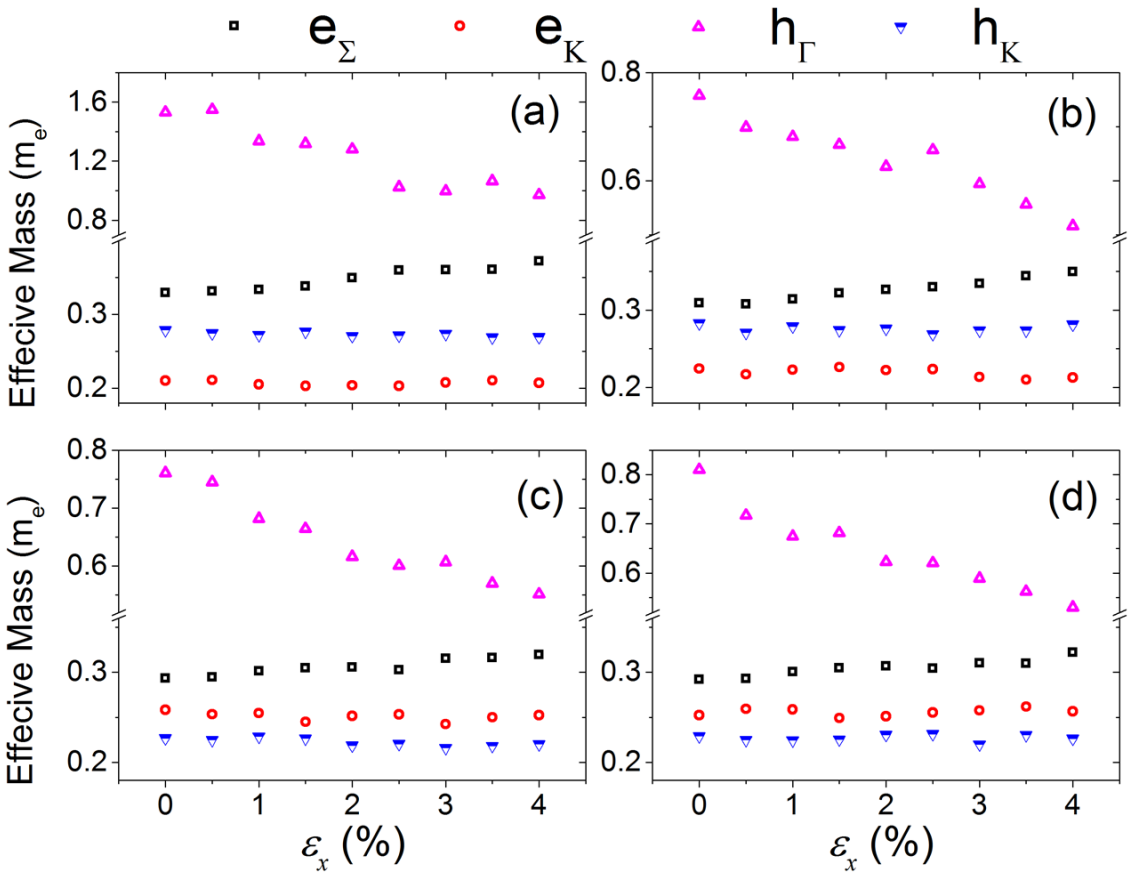

Figure 6.7 The variation of electron effective mas and hole effective mass with a uniaxial strain from 0% to 4% using different computational methods: (a) PBE, (b) PBE + vdW, (c) PBE + vdW + SOC, and (d) PBE + vdW + SOC + Poisson.

6.5 Conclusions

In this chapter, the strain effects are extended to other 2D TMDs including HfS_2 and WSe_2. First, the band structures of ML, BL, and TL HfS_2 suggest that the locations of band edges of 2D HfS_2 structures are not affected by number of layers. These 2D HfS_2 structures are subjected to external strain with a wide range from -15% to 10% strain. Both uniaxial and biaxial strain are considered. ML, BL and TL HfS2 are turned to metallic structures at a compressive strain over 13%. The mechanical boundary conditions (uniaxial and biaxial) show less predominant effects as compared to MoS_2. Besides, the effect of vdW interaction and SOC on the band structure of bilayer WSe_2 are studied. Our result shows giant spin splitting similar to the previous calculations. Our results indicate that the vdW interaction, SOC and Poisson effects may significantly influence the band edge locations, the gap energies of band transitions. The effective masses are found to be less dependent on the SOC or Poisson effect.

CHAPTER ONE

7. SUMMERY AND OUTLOOK

7.1 Summary

The aims of this thesis were to investigate the strain response of CVD-grown 2D TMDs. The roles of edges and defects on the modifications in electronic, optical, mechanical properties were identified. The interplay between edges, structures, and strain were studied to discover the underlying mechanisms of strain relaxation at the atomic scale.

Chapter 2 studied the effect of edges in 2D bilayer MoS_2 materials under an applied strain. The modeled bilayer structure composed of an infinitely large bottom layer and arrayed nanoribbons in the top layer. The edges of the nanoribbons allow the top layer to have more flexibility in terms of atomic relaxation compared to the bottom layer. The two layers were found to be subjected to different local strains under a tensile uniaxial strain/stress condition in the basal plane. The local strain and the variation in band gap energy ΔE_g at the center of the top layer were substantially smaller than those in the bottom layer under a tensile uniaxial strain/stress condition. These results demonstrate that distinct band gap energies can be induced/achieved in the bilayer structures under tensile uniaxial strain. Such variations need to be accounted for when analyzing strain effects on electronic properties using experimental methods or in continuum models.

Chapter 3 discussed the modifications in electronic properties and sliding behavior of MoS_2 bilayer at the presence of vacancy defects. Five types of vacancies including V_S,

V_{SS}, V_{Mo}, V_{MoS3} and V_{MoS6} were studied and compared to pristine structure. Localized charge states were activated both within the band gap region and near the band edges. The number of defect charge states was found to be increased with the number of vacancies. The defects embodied in the bottom affected the local density of states of atoms in both top and bottom layer. But the modifications in electronic properties were found to be limited to the atoms surrounding the vacancies. Therefore, the effects of vacancies were supposed to be local. Moreover, the potential energy surfaces for various types of vacancy were also identified and compared with that of pristine bilayer to study variations in the most favored sliding pathway. The optimal sliding route was found to be invariant to defects. However, the presence of vacancies increased the possibilities for sliding because the energy barriers were lowered. As a result, the interlayer coupling was considerably reduced in defect structures.

Chapter 4 switched to experimental scale structures to explore the relationship between strain, edges and ripples as observed in CVD-grown MoS_2 multilayers. A model multilayered system with terraces and edges was created to mimic the CVD-grown system. The strain response of the multilayered system was found to be layer dependent and the relaxation of individual layers was attributed to nucleation, propagation and interaction of ripples. The ripples were observed to nucleate at the locations of the edges of the layer in the regions below the edge and propagate inward to the center of the multilayered structure. The ripples had typical vertical displacements of ~0.1 Å for uniaxial tensile strain and ~10 Å for uniaxial compressive strain. The strains required for the formation of ripples were observed to be dependent on the dimensions of the layers.

In chapter 5, the interatomic interactions between Mo/S atoms were optimized in the form of hybrid REBO/LJ potential to best capture the structural and energetic properties, as well as the strain configuration at the presence of edges. The strain response of stacked MoS2 bilayer with a triangular shape were studied. The structures of the modeled system were identical to the CVD-grown structures. As a result, the edge configuration was reproduced and the strain response was more comparable to experimental observations. For example, the strain response at an applied tensile strain of 1.5% showed a "three-pointed star" shape in displacement map, which was astonishingly similar to the PL intensity map of the bilayer MoS_2 triangle found in recent experiments. Our results suggested that the strain subjected to the substrate was not able to completely transfer to the bilayered MoS_2 sample, and the difference in the layer strain caused lattice match, which resulted in the formation of Moiré pattern. The emergence of Moiré islands was correlated to the reduction in the layer strain. A new group of Moiré islands were nucleated every 3.2 % applied strain in tension and 2.5 % in compression, which lead to a periodic reduction in the layer strain.

Chapter 6 extended the study of strain effects to other 2D TMDs including HfS_2 and WSe_2. Unlike 2D MoS_2, the locations of band edges of HfS_2 were not affected by strain or number of layers. ML, BL and TL HfS_2 turned to metallic structures at a compressive strain over 13%. The mechanical boundary conditions (uniaxial and biaxial) showed less effects as compared to MoS_2. Besides, the effect of vdW interaction and SOC on the band structure of bilayer WSe_2 were studied, and a giant spin splitting was observed at the valence band edge. Our results indicated that the vdW interaction, SOC and Poisson effects significantly modified the band edge locations, the gap energies of band transitions. On the

other hand, the effective masses were found to be less dependent on the SOC or Poisson effect.

Here is the list of journal publications and presentations related to current thesis:

Publications

[1] **Wang, J**; Namburu R. R; Dubey, M; Dongare, A. M; Origins of Moiré patterns in CVD-grown MoS_2 bilayer structures at the atomic scales, *Scientific Reports.* (in preparation for submission)

[2] **Wang, J**; Dongare, A. M; Investigation of role of defects on the electronic structure and the mechanical behavior of MoS_2 bilayer structures, *Journal of Materials Science.* (in preparation for submission)

[3] Wu, W; **Wang, J;** Wright, N. C; Leppert-Simenauer, D. M; Ercius, P; Dongare, A. M; Pettes, M. T; Giant mechanico-optoelectronic effect in an atomically-thin semiconductor, *Nano Letters.* (in preparation for submission)

[4] **Wang, J**; Namburu R. R; Dubey, M; Dongare, A. M; Origins of ripples in CVD-grown few-layered MoS_2 structures under applied strain at atomic scales. *Scientific Reports* **2017**, *7*, 40862

[5] McCreary, A.; Ghosh, R.; Amani, M.; **Wang, J.;** Duerloo, K.-A.; Sharma, A.; Jarvis, K.; Reed, E.; Dongare, A. M.; Banerjee, S. K.; Terrones, M.; Namburu, R.; Dubey, M., Effects of uniaxial and biaxial strain on CVD-grown few-layered terrace structures of MoS_2. *ACS Nano* **2016,** *10*, 3186.

[6] Dong, L.*; **Wang, J**.*; Namburu, R.; Regan, T. P.; Dubey, M.; Dongare, A. M., Edge effects on band gap energy in bilayer *2H*-MoS_2 under uniaxial strain. *Journal of Applied Physics* **2015,** *117* (24), 244303.

* Authors have equal contributions

Presentations

Poster- **Wang, J**; Namburu R. R; Dubey, M; Dongare, A. M; Origins of ripples in CVD-grown few-layered MoS_2 structures under applied strain at atomic scales, **2017 Spring**, *Materials Research Society*

Poster- **Wang, J**; McCreary, A; Namburu, R; Dubey, M; Dongare, A.M; Theoretical study of electronic properties and sliding behavior of MoS_2 bilayer with vacancies, **2016 Fall**, *Materials Research Society*

Talk- **Wang, J**; McCreary, A; Dongare, A.M; Namburu, R; O'Regan, T.P; Dubey, M.; Deformation behavior of multilayer MoS_2 sheets at the atomic scales, **2015 Fall,** *Materials Research Society*.

Poster- **Wang, J**; Dong, L; Dongare, A.M; Namburu, R; O'Regan, T.P; Dubey, M; First principles study on strain induced variations in the electronic properties of stacked 2D materials, **2014 Fall**, *Materials Research Society*

Poster- **Wang, J**; Rajendran, A.M.; Dongare, A. M; Atomic Scale Modeling of Shock-Wave Propagation and Failure of Fused Silica. **2014 Fall**, *Materials Research Society*

Poster- **Wang, J**; Dong, L; Dongare, A.M; Namburu, R; O'Regan, T.P; Dubey, M; First principles calculation of the electronic properties of stacked MoS_2, **2014 Summer**, *Institute for Pure and Applied Mathematics (IPAM) Summer School, UCLA*

7.2 Outlook

It is now possible to build multilayer heterostructures either by stacking various atomic crystals on top of each other or by growth of different structures together to form interfaces [9]. While the electronic properties of isolated layer have been intensively explored, the behavior of the electronic interface among the stacked layers is still of great research interest. The electronic structure of the 2D layers can be easily influenced by the adjacent layer through the interlayer vdW coupling. This strategy to stack multiple 2D materials can be used to tailor the desired electronic response under various loading conditions. A challenge in the applicability of monolayer MoS_2 sheets arises from the direct-to-indirect band gap transitions under tensile strains of 1% and under compressive strains of -2% [36]. It is not clear if a stacked $MoS_2/HfS_2/WSe_2$ structure will result in a direct band gap or indirect band gap for the heterostructure. As a result, the vdW interface made from 2D TMDs will be of great research interests.

References

[1] A. Kuc, T. Heine, A. Kis, Electronic properties of transition-metal dichalcogenides. *MRS Bulletin* **40**, 577-584 (2015).

[2] F. J. Clauss, *Solid lubricants and self-lubricating solids*. (Elsevier, 2012).

[3] B. Dubertret, T. Heine, M. Terrones, The rise of two-dimensional materials. *Accounts of Chemical Research* **48**, 1-2 (2015).

[4] S. Z. Butler *et al.*, Progress, challenges, and opportunities in two-dimensional materials beyond graphene. *ACS Nano* **7**, 2898-2926 (2013).

[5] Q. H. Wang, K. Kalantar-Zadeh, A. Kis, J. N. Coleman, M. S. Strano, Electronics and optoelectronics of two-dimensional transition metal dichalcogenides. *Nature Nanotechnology* **7**, 699-712 (2012).

[6] B. Liu, A. Abbas, C. Zhou, Two-dimensional semiconductors: from materials preparation to electronic applications. *Advanced Electronic Materials*, (2017).

[7] C. Tan *et al.*, Recent advances in ultrathin two-dimensional nanomaterials. *Chemical Reviews* **117**, 6225-6331 (2017).

[8] A. V. Kolobov, J. Tominaga, *Two-Dimensional Transition-Metal Dichalcogenides*. (Springer, 2016), vol. 239.

[9] S. Tongay *et al.*, Monolayer behaviour in bulk ReS_2 due to electronic and vibrational decoupling. *Nature Communications* **5**, (2014).

[10] M. Chhowalla *et al.*, The chemistry of two-dimensional layered transition metal dichalcogenide nanosheets. *Nature Chemistry* **5**, 263-275 (2013).

[11] A. Kuc, T. Heine, The electronic structure calculations of two-dimensional transition-metal dichalcogenides in the presence of external electric and magnetic fields. *Chemical Society Reviews* **44**, 2603-2614 (2015).

[12] A. K. M. Newaz *et al.*, Electrical control of optical properties of monolayer MoS_2. *Solid State Communications* **155**, 49-52 (2013).

[13] E. J. G. Santos, E. Kaxiras, Electrically driven tuning of the dielectric constant in MoS_2 layers. *ACS Nano* **7**, 10741-10746 (2013).

[14] S. Wu *et al.*, Electrical tuning of valley magnetic moment through symmetry control in bilayer MoS_2. *Nature Physics* **9**, 149-153 (2013).

[15] D. Voiry, A. Mohite, M. Chhowalla, Phase engineering of transition metal dichalcogenides. *Chemical Society Reviews* **44**, 2702-2712 (2015).

[16] A. Geim, I. Grigorieva, Van der Waals heterostructures. *Nature* **499**, 419-425 (2013).

[17] H. Terrones, F. Lopez-Urias, M. Terrones, Novel hetero-layered materials with tunable direct band gaps by sandwiching different metal disulfides and diselenides. *Scientific Reports* **3**, 1549 (2013).

[18] A. Castellanos-Gomez *et al.*, Local strain engineering in atomically thin MoS_2. *Nano Letters* **13**, 5361-5366 (2013).

[19] H. J. Conley *et al.*, Bandgap Engineering of Strained Monolayer and Bilayer MoS_2. *Nano Letters* **13**, 3626-3630 (2013).

[20] P. Johari, V. B. Shenoy, Tuning the electronic properties of semiconducting transition metal dichalcogenides by applying mechanical strains. *ACS Nano* **6**, 5449-5456 (2012).

[21] M. Chhowalla *et al.*, The chemistry of two-dimensional layered transition metal dichalcogenide nanosheets. *Nat Chem* **5**, 263-275 (2013).

[22] M. Chhowalla, D. Jena, H. Zhang, Two-dimensional semiconductors for transistors. *Nature Reviews Materials* **1**, 16052 (2016).

[23] RadisavljevicB, RadenovicA, BrivioJ, GiacomettiV, KisA, Single-layer MoS_2 transistors. *Nature Nanotechnology* **6**, 147-150 (2011).

[24] A. Ayari, E. Cobas, O. Ogundadegbe, M. S. Fuhrer, Realization and electrical characterization of ultrathin crystals of layered transition-metal dichalcogenides. *Journal of applied physics* **101**, 014507 (2007).

[25] Y. F. Lin *et al.*, Origin of noise in layered MoTe2 transistors and its possible use for environmental sensors. *Advanced Materials* **27**, 6612-6619 (2015).

[26] Z. Yin *et al.*, Single-layer MoS_2 phototransistors. *ACS Nano* **6**, 74-80 (2011).

[27] C. Lee *et al.*, Frictional characteristics of atomically thin sheets. *Science* **328**, 76-80 (2010).

[28] X. Wang *et al.*, Chemical vapor deposition growth of crystalline monolayer $MoSe_2$. *ACS Nano* **8**, 5125-5131 (2014).

[29] K. F. Mak, C. Lee, J. Hone, J. Shan, T. F. Heinz, Atomically thin MoS_2: a new direct-gap semiconductor. *Physical Review Letters* **105**, 136805 (2010).

[30] W. Jin *et al.*, Direct measurement of the thickness-dependent electronic band structure of MoS_2 using angle-resolved photoemission spectroscopy. *Physical Review Letters* **111**, 106801 (2013).

[31] H. Zeng *et al.*, Optical signature of symmetry variations and spin-valley coupling in atomically thin tungsten dichalcogenides. *Scientific Reports* **3**, 1608 (2013).

[32] P. Hohenberg, W. Kohn, Inhomogeneous electron gas. *Physical Review* **136**, B864-B871 (1964).

[33] G.-B. Liu, D. Xiao, Y. Yao, X. Xu, W. Yao, Electronic structures and theoretical modelling of two-dimensional group-VIB transition metal dichalcogenides. *Chemical Society Reviews* **44**, 2643-2663 (2015).

[34] A. Kuc, N. Zibouche, T. Heine, Influence of quantum confinement on the electronic structure of the transition metal sulfide TS_2. *Physical Review B* **83**, 245213 (2011).

[35] L. Zhang, A. Zunger, Evolution of Electronic Structure as a Function of Layer Thickness in Group-VIB Transition Metal Dichalcogenides: Emergence of Localization Prototypes. *Nano Letters*, (2015).

[36] L. Dong, R. Namburu, T. O'Regan, M. Dubey, A. Dongare, Theoretical study on strain-induced variations in electronic properties of monolayer MoS2. *Journal of Materials Science* **49**, 6762-6771 (2014).

[37] K. F. Mak, C. Lee, J. Hone, J. Shan, T. F. Heinz, Atomically Thin MoS_2: A New Direct-Gap Semiconductor. *Physical Review Letters* **105**, (2010).

[38] M. Cahay. (The Electrochemical Society, 2001).

[39] T. Cheiwchanchamnangij, W. R. Lambrecht, Quasiparticle band structure calculation of monolayer, bilayer, and bulk MoS_2. *Physical Review B* **85**, 205302 (2012).

[40] H. Shi *et al.*, Exciton dynamics in suspended monolayer and few-layer MoS_2 2D crystals. *ACS Nano* **7**, 1072-1080 (2013).

[41] J. Padilha, H. Peelaers, A. Janotti, C. Van de Walle, Nature and evolution of the band-edge states in MoS 2: From monolayer to bulk. *Physical Review B* **90**, 205420 (2014).

[42] M. Li, Y. Wan, L. Tu, Y. Yang, J. Lou, The Effect of $VMoS_3$ Point Defect on the Elastic Properties of Monolayer MoS_2 with REBO Potentials. *Nanoscale Research Letters* **11**, 1-7 (2016).

[43] P. Nicolini, T. Polcar, A comparison of empirical potentials for sliding simulations of MoS2. *Computational Materials Science* **115**, 158-169 (2016).

[44] G. Ye *et al.*, Defects Engineered Monolayer MoS_2 for Improved Hydrogen Evolution Reaction. *Nano Letters* **16**, 1097-1103 (2016).

[45] A. Castellanos-Gomez *et al.*, Local strain engineering in atomically thin MoS2. *Nano Letters* **13**, 5361-5366 (2013).

[46] H. J. Conley *et al.*, Bandgap engineering of strained monolayer and bilayer MoS2. *Nano Lett* **13**, 3626-3630 (2013).

[47] M. A. Bissett, M. Tsuji, H. Ago, Strain engineering the properties of graphene and other two-dimensional crystals. *Physical Chemistry Chemical Physics* **16**, 11124-11138 (2014).

[48] H. Wang, H. Yuan, S. S. Hong, Y. Li, Y. Cui, Physical and chemical tuning of two-dimensional transition metal dichalcogenides. *Chemical Society Reviews* **44**, 2664-2680 (2015).

[49] T. Shen, A. V. Penumatcha, J. Appenzeller, Strain engineering for transition metal dichalcogenides based field effect transistors. *ACS Nano* **10**, 4712-4718 (2016).

[50] S. Bertolazzi, J. Brivio, A. Kis, Stretching and breaking of ultrathin MoS_2. *ACS Nano* **5**, 9703-9709 (2011).

[51] K. He, C. Poole, K. F. Mak, J. Shan, Experimental demonstration of continuous electronic structure tuning via strain in atomically thin MoS_2. *Nano Letters* **13**, 2931-2936 (2013).

[52] S. B. Desai *et al.*, Strain-induced indirect to direct bandgap transition in multilayer WSe2. *Nano Letters* **14**, 4592-4597 (2014).

[53] J. Qi, X. Li, X. Qian, J. Feng, Bandgap engineering of rippled MoS2 monolayer under external electric field. *Applied Physics Letters* **102**, 173112 (2013).

[54] L. Dong, A. M. Dongare, R. R. Namburu, T. P. O'Regan, M. Dubey, Theoretical study on strain induced variations in electronic properties of 2H-MoS2 bilayer sheets. *Applied Physics Letters* **104**, 053107 (2014).

[55] P. Lu, X. Wu, W. Guo, X. C. Zeng, Strain-dependent electronic and magnetic properties of MoS_2 monolayer, bilayer, nanoribbons and nanotubes. *Physical Chemistry Chemical Physics* **14**, 13035-13040 (2012).

[56] W. S. Yun, S. W. Han, S. C. Hong, I. G. Kim, J. D. Lee, Thickness and strain effects on electronic structures of transition metal dichalcogenides: 2H-$M{X}_{2}$ semiconductors (M $=$ Mo, W; X $=$ S, Se, Te). *Physical Review B* **85**, 033305 (2012).

[57] H. Shi, H. Pan, Y.-W. Zhang, B. I. Yakobson, Quasiparticle band structures and optical properties of strained monolayer MoS${}_{2}$ and WS${}_{2}$. *Physical Review B* **87**, 155304 (2013).

[58] S. Yu, H. D. Xiong, K. Eshun, H. Yuan, Q. Li, Phase transition, effective mass and carrier mobility of MoS2 monolayer under tensile strain. *Applied Surface Science* **325**, 27-32 (2015).

[59] M. Ghorbani-Asl *et al.*, Electromechanics in MoS(2) and WS(2): nanotubes vs. monolayers. *Sci Rep* **3**, 2961 (2013).

[60] Y. Zhan, Z. Liu, S. Najmaei, P. M. Ajayan, J. Lou, Large-area vapor-phase growth and characterization of MoS2 atomic layers on a SiO2 substrate. *Small* **8**, 966-971 (2012).

[61] K. Liu *et al.*, Evolution of interlayer coupling in twisted molybdenum disulfide bilayers. *Nature Communications* **5**, (2014).

[62] N. A. Lanzillo *et al.*, Temperature-dependent phonon shifts in monolayer MoS2. *Applied Physics Letters* **103**, 093102 (2013).

[63] A. McCreary *et al.*, Effects of Uniaxial and Biaxial Strain on Few-Layered Terrace Structures of MoS2 Grown by Vapor Transport. *ACS Nano* **10**, 3186-3197 (2016).

[64] W. Zhou *et al.*, Intrinsic Structural Defects in Monolayer Molybdenum Disulfide. *Nano Letters* **13**, 2615-2622 (2013).

[65] S. Tongay *et al.*, Defects activated photoluminescence in two-dimensional semiconductors: interplay between bound, charged, and free excitons. *Scientific Reports* **3**, 2657 (2013).

[66] A. Mills *et al.*, Ripples near edge terminals in MoS2 few layers and pyramid nanostructures. *Applied Physics Letters* **108**, 081601 (2016).

[67] V. Borisenko *et al.*, Theoretical study of defect impact on two-dimensional MoS2. (2015).

[68] M. Yankowitz *et al.*, Emergence of superlattice Dirac points in graphene on hexagonal boron nitride. *Nature Physics* **8**, 382-386 (2012).

[69] J. Kang, J. Li, S.-S. Li, J.-B. Xia, L.-W. Wang, Electronic structural Moiré pattern effects on MoS2/MoSe2 2D heterostructures. *Nano Letters* **13**, 5485-5490 (2013).

[70] S. Tang *et al.*, Precisely aligned graphene grown on hexagonal boron nitride by catalyst free chemical vapor deposition. *Scientific Reports* **3**, 2666 (2013).

[71] W. Yang *et al.*, Epitaxial growth of single-domain graphene on hexagonal boron nitride. *Nature Materials* **12**, 792-797 (2013).

[72] C. Zhang *et al.*, Interlayer couplings, Moiré patterns, and 2D electronic superlattices in MoS2/WSe2 hetero-bilayers. *Science Advances* **3**, e1601459 (2017).

[73] J. Coraux, T. N. Plasa, C. Busse, T. Michely, Structure of epitaxial graphene on Ir (111). *New Journal of Physics* **10**, 043033 (2008).

[74] S. G. Sørensen, H. G. Füchtbauer, A. K. Tuxen, A. S. Walton, J. V. Lauritsen, Structure and electronic properties of in situ synthesized single-layer MoS2 on a gold surface. *ACS Nano* **8**, 6788-6796 (2014).

[75] S. S. Grønborg *et al.*, Synthesis of Epitaxial Single-Layer MoS2 on Au (111). *Langmuir* **31**, 9700-9706 (2015).

[76] D. Kiriya *et al.*, Oriented Growth of Gold Nanowires on MoS2. *Advanced Functional Materials* **25**, 6257-6264 (2015).

[77] N. Krane, C. Lotze, J. M. Läger, G. Reecht, K. J. Franke, Electronic structure and luminescence of quasi-freestanding MoS2 nanopatches on Au (111). *Nano Letters* **16**, 5163-5168 (2016).

[78] D. Sholl, J. A. Steckel, *Density functional theory: a practical introduction*. (John Wiley & Sons, 2011).

[79] W. Kohn, L. J. Sham, Self-consistent equations including exchange and correlation effects. *Physical Review* **140**, A1133 (1965).

[80] J. P. Perdew, K. Burke, M. Ernzerhof, Generalized gradient approximation made simple. *Physical Review Letters* **77**, 3865 (1996).

[81] M. G. Medvedev, I. S. Bushmarinov, J. Sun, J. P. Perdew, K. A. Lyssenko, Density functional theory is straying from the path toward the exact functional. *Science* **355**, 49-52 (2017).

[82] L. J. Sham, M. Schlüter, Density-Functional Theory of the Energy Gap. *Physical Review Letters* **51**, 1888-1891 (1983).

[83] K. F. Mak, C. Lee, J. Hone, J. Shan, T. F. Heinz, Atomically Thin MoS_2: A New Direct-Gap Semiconductor. *Physical Review Letters* **105**, 136805 (2010).

[84] J. Heyd, G. E. Scuseria, M. Ernzerhof, Hybrid functionals based on a screened Coulomb potential. *J. Chem. Phys.* **118**, 8207-8215 (2003).

[85] F. Fuchs, J. Furthmüller, F. Bechstedt, M. Shishkin, G. Kresse, Quasiparticle band structure based on a generalized Kohn-Sham scheme. *Physical Review B* **76**, 115109 (2007).

[86] J. Hafner, Ab-initio simulations of materials using VASP: Density-functional theory and beyond. *J. Comput. Chem.* **29**, 2044-2078 (2008).

[87] J. K. Ellis, M. J. Lucero, G. E. Scuseria, The indirect to direct band gap transition in multilayered MoS2 as predicted by screened hybrid density functional theory. *Applied Physics Letters* **99**, 261908 (2011).

[88] T. Cheiwchanchamnangij, W. R. L. Lambrecht, Quasiparticle band structure calculation of monolayer, bilayer, and bulk MoS_2. *Physical Review B* **85**, 205302 (2012).

[89] H. Peelaers, C. G. Van de Walle, Effects of strain on band structure and effective masses in MoS_2. *Physical Review B* **86**, 241401 (2012).

[90] H. J. Conley *et al.*, Bandgap engineering of strained monolayer and bilayer MoS_2. *Nano Letters* **13**, 3626-3630 (2013).

[91] H. Shi, H. Pan, Y.-W. Zhang, B. I. Yakobson, Quasiparticle band structures and optical properties of strained monolayer MoS_2 and WS_2. *Physical Review B* **87**, 155304 (2013).

[92] A. Tkatchenko, M. Scheffler, Accurate Molecular van der Waals interactions from ground-state electron density and free-atom reference data. *Physical Review Letters* **102**, 073005 (2009).

[93] T. Bučko, S. Lebègue, J. Hafner, J. G. Ángyán, Tkatchenko-Scheffler van der Waals correction method with and without self-consistent screening applied to solids. *Physical Review B* **87**, 064110 (2013).

[94] D. Frenkel, B. Smit, *Understanding molecular simulation: from algorithms to applications*. (Academic press, 2001), vol. 1.

[95] T. Liang, S. Phillpot, S. Sinnott, Parametrization of a reactive many-body potential for Mo–S systems. *Physical Review B* **79**, (2009).

[96] J. A. Stewart, D. E. Spearot, Atomistic simulations of nanoindentation on the basal plane of crystalline molybdenum disulfide (MoS_2). *Modelling and Simulation in Materials Science and Engineering* **21**, 045003 (2013).

[97] K. He, C. Poole, K. F. Mak, J. Shan, Experimental demonstration of continuous electronic structure tuning via strain in atomically thin MoS_2. *Nano Letters* **13**, 2931-2936 (2013).

[98] J. S. Qi, X. Li, X. F. Qian, J. Feng, Bandgap engineering of rippled MoS_2 monolayer under external electric field. *Applied Physics Letters* **102**, (2013).

[99] L. Dong, A. M. Dongare, R. R. Namburu, T. P. O'Regan, M. Dubey, Theoretical study on strain induced variations in electronic properties of 2H-MoS_2 bilayer sheets. *Applied Physics Letters* **104**, 053107 (2014).

[100] W. S. Yun, S. W. Han, S. C. Hong, I. G. Kim, J. D. Lee, Thickness and strain effects on electronic structures of transition metal dichalcogenides: 2H-MX_2 semiconductors (M = Mo, W; X = S, Se, Te). *Physical Review B* **85**, 033305 (2012).

[101] C. R. Zhu *et al.*, Strain tuning of optical emission energy and polarization in monolayer and bilayer MoS_2. *Physical Review B* **88**, 121301 (2013).

[102] S. Bhattacharyya, A. K. Singh, Semiconductor-metal transition in semiconducting bilayer sheets of transition-metal dichalcogenides. *Physical Review B* **86**, 075454 (2012).

[103] H. I. Rasool, C. Ophus, W. S. Klug, A. Zettl, J. K. Gimzewski, Measurement of the intrinsic strength of crystalline and polycrystalline graphene. *Nature Communications* **4**, (2013).

[104] P. Lu, X. Wu, W. Guo, X. C. Zeng, Strain-dependent electronic and magnetic properties of MoS_2 monolayer, bilayer, nanoribbons and nanotubes. *Physical Chemistry Chemical Physics* **14**, 13035-13040 (2012).

[105] E. Scalise, M. Houssa, G. Pourtois, V. Afanas'ev, A. Stesmans, Strain-induced semiconductor to metal transition in the two-dimensional honeycomb structure of MoS_2. *Nano Research* **5**, 43-48 (2012).

[106] A. L. Kitt *et al.*, How Graphene Slides: Measurement and Theory of Strain-Dependent Frictional Forces between Graphene and SiO_2. *Nano Letters* **13**, 2605-2610 (2013).

[107] P. E. Blochl, Projector augmented-wave method. *Physical Review B* **50**, 17953 (1994).

[108] G. Kresse, J. Furthmüller, Efficient iterative schemes for ab initio total-energy calculations using a plane-wave basis set. *Physical Review B* **54**, 11169 (1996).

[109] J. P. Perdew, K. Burke, M. Ernzerhof, Generalized gradient approximation made simple. *Physical Review Letters* **77**, 3865-3868 (1996).

[110] J. F. Nye, *Physical Properties of Crystals: Their Representation by Tensors and Matrices*. (Oxford University Press, London, 1957).

[111] T. Böker *et al.*, Band structure of MoS_2, $MoSe_2$, and α-$MoTe_2$: Angle-resolved photoelectron spectroscopy and ab initio calculations. *Physical Review B* **64**, 235305 (2001).

[112] R. Aksoy *et al.*, X-ray diffraction study of molybdenum disulfide to 38.8 GPa. *Journal of Physics and Chemistry of Solids* **67**, 1914-1917 (2006).

[113] A. Tkatchenko, M. Scheffler, Accurate molecular van der Waals interactions from ground-state electron density and free-atom reference data. *Physical Review Letters* **102**, 073005 (2009).

[114] L. Dong, A. M. Dongare, R. R. Namburu, T. P. O'Regan, M. Dubey, Theoretical study on strain induced variations in electronic properties of 2*H*-MoS_2 bilayer sheets. *Applied Physics Letters* **104**, 053107 (2014).

[115] A. N. Enyashin, M. Bar-Sadan, L. Houben, G. Seifert, Line defects in molybdenum disulfide layers. *The Journal of Physical Chemistry C* **117**, 10842-10848 (2013).

[116] M. Ghorbani-Asl, A. N. Enyashin, A. Kuc, G. Seifert, T. Heine, Defect-induced conductivity anisotropy in MoS_2 monolayers. *Physical Review B* **88**, 245440 (2013).

[117] L.-p. Feng, J. Su, S. Chen, Z.-t. Liu, First-principles investigations on vacancy formation and electronic structures of monolayer MoS_2. *Materials Chemistry and Physics* **148**, 5-9 (2014).

[118] L.-p. Feng, J. Su, Z.-t. Liu, Effect of vacancies on structural, electronic and optical properties of monolayer MoS_2: A first-principles study. *Journal of Alloys and Compounds* **613**, 122-127 (2014).

[119] Y. Gan, H. Zhao, Chirality effect of mechanical and electronic properties of monolayer MoS_2 with vacancies. *Physics Letters A* **378**, 2910-2914 (2014).

[120] J.-Y. Noh, H. Kim, Y.-S. Kim, Stability and electronic structures of native defects in single-layer MoS_2. *Physical Review B* **89**, 205417 (2014).

[121] K. C. Santosh, C. L. Roberto, A. Rafik, M. W. Robert, C. Kyeongjae, Impact of intrinsic atomic defects on the electronic structure of MoS_2 monolayers. *Nanotechnology* **25**, 375703 (2014).

[122] S. Yuan, R. Roldán, M. Katsnelson, F. Guinea, Effect of point defects on the optical and transport properties of MoS_2 and WS_2. *Physical Review B* **90**, 041402 (2014).

[123] S. Haldar, H. Vovusha, M. K. Yadav, O. Eriksson, B. Sanyal, Systematic study of structural, electronic, and optical properties of atomic-scale defects in the two-dimensional transition metal dichalcogenides MX_2 (M = Mo, W; X = S, Se, Te). *Physical Review B* **92**, 235408 (2015).

[124] H.-P. Komsa, A. V. Krasheninnikov, Native defects in bulk and monolayer MoS_2 from first principles. *Physical Review B* **91**, 125304 (2015).

[125] B. Akdim, R. Pachter, S. Mou, Theoretical analysis of the combined effects of sulfur vacancies and analyte adsorption on the electronic properties of single-layer MoS_2. *Nanotechnology* **27**, 185701 (2016).

[126] C. González, B. Biel, Y. Dappe, Theoretical characterisation of point defects on a MoS_2 monolayer by scanning tunnelling microscopy. *Nanotechnology* **27**, 105702 (2016).

[127] P. Vancsó *et al.*, The intrinsic defect structure of exfoliated MoS_2 single layers revealed by scanning tunneling microscopy. *Scientific Reports* **6**, (2016).

[128] D. Liu, Y. Guo, L. Fang, J. Robertson, Sulfur vacancies in monolayer MoS_2 and its electrical contacts. *Applied Physics Letters* **103**, 183113 (2013).

[129] S. McDonnell, R. Addou, C. Buie, R. M. Wallace, C. L. Hinkle, Defect-dominated doping and contact resistance in MoS_2. *ACS Nano* **8**, 2880-2888 (2014).

[130] H. Nan *et al.*, Strong photoluminescence enhancement of MoS2 through defect engineering and oxygen bonding. *ACS Nano* **8**, 5738-5745 (2014).

[131] R. Addou, L. Colombo, R. M. Wallace, Surface defects on natural MoS_2. *ACS Applied Materials & Interfaces* **7**, 11921-11929 (2015).

[132] R. Addou *et al.*, Impurities and electronic property variations of natural MoS_2 crystal surfaces. *ACS Nano* **9**, 9124-9133 (2015).

[133] W. M. Parkin *et al.*, Raman shifts in electron-irradiated monolayer MoS_2. *ACS Nano* **10**, 4134-4142 (2016).

[134] S. Mignuzzi *et al.*, Effect of disorder on Raman scattering of single-layer MoS_2. *Physical Review B* **91**, 195411 (2015).

[135] R. Mishra, W. Zhou, S. J. Pennycook, S. T. Pantelides, J.-C. Idrobo, Long-range ferromagnetic ordering in manganese-doped two-dimensional dichalcogenides. *Physical Review B* **88**, 144409 (2013).

[136] A. Ramasubramaniam, D. Naveh, Mn-doped monolayer MoS_2: an atomically thin dilute magnetic semiconductor. *Physical Review B* **87**, 195201 (2013).

[137] P. E. Blöchl, Projector augmented-wave method. *Physical Review B* **50**, 17953 (1994).

[138] G. Kresse, J. Furthmüller, Efficient iterative schemes for ab initio total-energy calculations using a plane-wave basis set. *Physical Review B* **54**, 11169 (1996).

[139] J. P. Perdew, K. Burke, M. Ernzerhof, Generalized gradient approximation made simple. *Physical Review Letters* **77**, 3865-3868 (1996).

[140] L. Dong *et al.*, Edge effects on band gap energy in bilayer 2H-MoS_2 under uniaxial strain. *Journal of Applied Physics* **117**, 244303 (2015).

[141] A. McCreary *et al.*, Effects of uniaxial and biaxial strain on few-layered terrace structures of MoS_2 grown by vapor transport. *ACS Nano* **10**, 3186-3197 (2016).

[142] G. Levita, A. Cavaleiro, E. Molinari, T. Polcar, M. Righi, Sliding properties of MoS_2 layers: load and interlayer orientation effects. *The Journal of Physical Chemistry C* **118**, 13809-13816 (2014).

[143] P. Tao, H.-H. Guo, T. Yang, Z.-D. Zhang, Stacking stability of MoS 2 bilayer: An ab initio study. *Chinese Physics B* **23**, 106801 (2014).

[144] B. Cao, T. Li, Interlayer electronic coupling in arbitrarily stacked MoS_2 bilayers controlled by interlayer S–S interaction. *The Journal of Physical Chemistry C* **119**, 1247-1252 (2015).

[145] L. Tapasztó *et al.*, Breakdown of continuum mechanics for nanometre-wavelength rippling of graphene. *Nature Physics* **8**, 739-742 (2012).

[146] J. Brivio, D. T. Alexander, A. Kis, Ripples and layers in ultrathin MoS_2 membranes. *Nano Letters* **11**, 5148-5153 (2011).

[147] A. Kushima, X. Qian, P. Zhao, S. Zhang, J. Li, Ripplocations in van der Waals layers. *Nano Letters* **15**, 1302-1308 (2015).

[148] J. W. Jiang, The buckling of single-layer MoS_2 under uniaxial compression. *Nanotechnology* **25**, 355402 (2014).

[149] J.-W. Jiang, The strain rate effect on the buckling of single-layer MoS_2. *Scientific Reports* **5**, (2015).

[150] Y. Zheng *et al.*, Quantum mechanical rippling of a MoS_2 monolayer controlled by interlayer bilayer coupling. *Physical Review Letters* **114**, 065501 (2015).

[151] L. Dong *et al.*, Edge effects on band gap energy in bilayer 2H-MoS_2 under uniaxial strain. *Journal of Applied Physics* **117**, 244303 (2015).

[152] T. Liang, S. R. Phillpot, S. B. Sinnott, Parametrization of a reactive many-body potential for Mo–S systems. *Physical Review B* **79**, 245110 (2009).

[153] S. Plimpton, Fast parallel algorithms for short-range molecular dynamics. *Journal of Computational Physics* **117**, 1-19 (1995).

[154] S. Xiong, G. Cao, Molecular dynamics simulations of mechanical properties of monolayer MoS_2. *Nanotechnology* **26**, 185705 (2015).

[155] H. Kumar, D. Er, L. Dong, J. Li, V. B. Shenoy, Elastic deformations in 2D van der waals heterostructures and their impact on optoelectronic properties: predictions from a multiscale computational approach. *Scientific Reports* **5**, (2015).

[156] J. Wang, R. R. Namburu, M. Dubey, A. M. Dongare, Origins of ripples in cvd-grown few-layered MoS_2 structures under applied strain at atomic scales. *Scientific Reports* **7**, 40862 (2017).

[157] M. Ritter, W. Ranke, W. Weiss, Growth and structure of ultrathin FeO films on Pt (111) studied by STM and LEED. *Physical Review B* **57**, 7240 (1998).

[158] H. Kumar, D. Er, L. Dong, J. Li, V. B. Shenoy, Elastic Deformations in 2D van der waals heterostructures and their impact on optoelectronic properties: predictions from a multiscale computational approach. *Scientific Reports* **5**, 10872 (2015).

[159] J. A. Miwa *et al.*, Electronic structure of epitaxial single-layer MoS_2. *Physical Review Letters* **114**, 046802 (2015).

[160] A. Bruix *et al.*, Single-layer MoS 2 on Au (111): Band gap renormalization and substrate interaction. *Physical Review B* **93**, 165422 (2016).

[161] J. L. Feldman, Elastic constants of 2H-MoS_2 and 2H-$NbSe_2$ extracted from measured dispersion curves and linear compressibilities. *Journal of Physics and Chemistry of Solids* **37**, 1141-1144 (1976).

[162] E. Selvi, Y. Ma, R. Aksoy, A. Ertas, A. White, High pressure X-ray diffraction study of tungsten disulfide. *Journal of Physics and Chemistry of Solids* **67**, 2183-2186 (2006).

[163] A. K. Geim, I. V. Grigorieva, Van der Waals heterostructures. *Nature* **499**, 419-425 (2013).

[164] S. Das, J. A. Robinson, M. Dubey, H. Terrones, M. Terrones, Beyond graphene: progress in novel two-dimensional materials and van der Waals solids. *Annual Review of Materials Research* **45**, 1-27 (2015).

[165] D. Jariwala, T. J. Marks, M. C. Hersam, Mixed-dimensional van der Waals heterostructures. *Nature Materials*, (2016).

[166] T. Kanazawa *et al.*, Few-layer HfS_2 transistors. *Scientific Reports* **6**, (2016).

[167] S. H. Chae *et al.*, Oxidation effect in octahedral hafnium disulfide thin film. *ACS Nano* **10**, 1309-1316 (2016).

[168] H. Yuan *et al.*, Zeeman-type spin splitting controlled by an electric field. *Nature Physics* **9**, 563-569 (2013).

[169] N. Zibouche, A. Kuc, J. Musfeldt, T. Heine, Transition-metal dichalcogenides for spintronic applications. *Annalen der Physik* **526**, 395-401 (2014).

[170] C. Chakraborty, L. Kinnischtzke, K. M. Goodfellow, R. Beams, A. N. Vamivakas, Voltage-controlled quantum light from an atomically thin semiconductor. *Nature Nanotechnology* **10**, 507-511 (2015).

[171] P. Tonndorf *et al.*, Single-photon emission from localized excitons in an atomically thin semiconductor. *Optica* **2**, 347-352 (2015).

[172] S. Kumar, A. Kaczmarczyk, B. D. Gerardot, Strain-induced spatial and spectral isolation of quantum emitters in mono-and bilayer WSe_2. *Nano Letters* **15**, 7567-7573 (2015).

[173] R. Schmidt *et al.*, Reversible uniaxial strain tuning in atomically thin WSe2. *2D Materials* **3**, 021011 (2016).

[174] D. T. Hodul, A. M. Stacy, Anomalies in the properties of Hf $(S_{2-x}Te_x)_{1-y}$ and Hf $(Se_{2-x}Te_x)_{1-y}$ near the metal-insulator transition. *Journal of Solid State Chemistry* **54**, 438-446 (1984).

[175] Q. Zhao *et al.*, Elastic, electronic, and dielectric properties of bulk and monolayer ZrS_2, $ZrSe_2$, HfS_2, $HfSe_2$ from van der Waals density-functional theory. *Physica Status Solidi (B)*, (2017).

[176] L. E. Conroy, K. C. Park, Electrical properties of the Group IV disulfides, titanium disulfide, zirconium disulfide, hafnium disulfide and tin disulfide. *Inorganic Chemistry* **7**, 459-463 (1968).

[177] S. Kim, J. M. Zuo, N. T. Nguyen, D. C. Johnson, D. G. Cahill, Structure of layered WSe_2 thin films with ultralow thermal conductivity. *Journal of Materials Research* **23**, 1064-1067 (2008).

[178] W. Schutte, J. De Boer, F. Jellinek, Crystal structures of tungsten disulfide and diselenide. *Journal of Solid State Chemistry* **70**, 207-209 (1987).

[179] C. Chiritescu *et al.*, Ultralow thermal conductivity in disordered, layered WSe_2 crystals. *Science* **315**, 351-353 (2007).

[180] P. Erhart, P. Hyldgaard, D. O. Lindroth, Microscopic origin of thermal conductivity reduction in disordered van der Waals solids. *Chemistry of Materials* **27**, 5511-5518 (2015).

[181] P. Norouzzadeh, D. J. Singh, Thermal conductivity of single-layer WSe_2 by a Stillinger-Weber potential. *Nanotechnology*, (2016).

[182] L.-p. Feng, N. Li, M.-h. Yang, Z.-t. Liu, Effect of pressure on elastic, mechanical and electronic properties of WSe_2: A first-principles study. *Materials Research Bulletin* **50**, 503-508 (2014).

[183] Z. Zhu, Y. Cheng, U. Schwingenschlögl, Giant spin-orbit-induced spin splitting in two-dimensional transition-metal dichalcogenide semiconductors. *Physical Review B* **84**, 153402 (2011).

[184] L. Debbichi, O. Eriksson, S. Lebègue, Electronic structure of two-dimensional transition metal dichalcogenide bilayers from ab initio theory. *Physical Review B* **89**, 205311 (2014).

[185] Z.-H. Chi *et al.*, Pressure-Induced Metallization of Molybdenum Disulfide. *Physical Review Letters* **113**, 036802 (2014).

[186] A. P. Nayak *et al.*, Pressure-induced semiconducting to metallic transition in multilayered molybdenum disulphide. *Nature Communications* **5**, (2014).

[187] Z. Zhao *et al.*, Pressure induced metallization with absence of structural transition in layered molybdenum diselenide. *Nature Communications* **6**, (2015).

[188] S. Bhattacharyya, A. K. Singh, Semiconductor-metal transition in semiconducting bilayer sheets of transition-metal dichalcogenides. *Physical Review B* **86**, 075454 (2012).

[189] K. Ashok, P. K. Ahluwalia, Semiconductor to metal transition in bilayer transition metals dichalcogenides MX 2 (M = Mo, W; X = S, Se, Te). *Modelling and Simulation in Materials Science and Engineering* **21**, 065015 (2013).

[190] W. S. Yun, S. Han, S. C. Hong, I. G. Kim, J. Lee, Thickness and strain effects on electronic structures of transition metal dichalcogenides: 2H-MX_2 semiconductors (M= Mo, W; X= S, Se, Te). *Physical Review B* **85**, 033305 (2012).